Magnetic resonance properties of all solution-processed Iron Garnet thin films

Thesis submitted in partial fulfilment

for the Award of Degree

DOCTOR OF PHILOSOPHY

by

Rajnandini Sharma

SCHOOL OF MATERIALS SCIENCE AND TECHNOLOGY

INDIAN INSTITUTE OF TECHNOLOGY

BANARAS HINDU UNIVERSITY

VARANASI - 221 005

INDIA

ROLL NUMBER
18111007

YEAR OF SUBMISSION
2023

Dedicated to Maa

Certificate

It is certified that the work contained in the thesis titled **"Magnetic resonance properties of all solution-processed Iron Garnet thin films"** by **Ms. Rajnandini Sharma**, Roll Number **18111007**, has been carried out under my/our supervision and that this work has not been submitted elsewhere for a degree.

It is further certified that the student has fulfilled all the requirements of Comprehensive Examination, Candidacy and SOTA for the award of Ph.D Degree.

Supervisor
Dr. Shrawan Kumar Mishra
School of Materials Science & Technology
IIT (BHU), Varanasi-221005

Declaration

I, **Rajnandini Sharma**, certify that the work embodied in this thesis is my own bona-fide work and carried out by me under the supervision of **Dr. Shrawan Kumar Mishra** from July 2018 to December 2023 at the **School of Materials Science & Technology**, Indian Institute of Technology (BHU), Varanasi. The matter embodied in this thesis has not been submitted for the award of any other degree/diploma. I declare that I have faithfully acknowledged and given credits to the research scholars/scientists wherever their works have been cited in my work in this thesis. I further declare that I have not willfully copied any others' work, paragraphs, text, data, results, etc., reported in journals, books, magazines, reports dissertations, theses, etc., or available at websites and have not included them in this thesis and have not cited as my own work.

Date — Signature of the student

Place: Varanasi — (Rajnandini Sharma)

Certificate by the Supervisor

It is certified that the above statement made by the student is correct to the best of my knowledge.

Dr. Shrawan Kumar Mishra

School of Materials Science & Technology

IIT (BHU), Varanasi

Coordinator

School of Materials Science & Technology

IIT (BHU), Varanasi

Copyright Transfer Certificate

Title of the Thesis : **Magnetic resonance properties of all solution-processed Iron Garnet thin films**

Name of the Student : **Rajnandini Sharma**

Copyright Transfer

The undersigned hereby assigns to the Indian Institute of Technology (Banaras Hindu University) Varanasi all rights under copyright that may exist in and for the above thesis submitted for the award of the **Doctor of Philosophy**.

Date — Signature of the student

Place: Varanasi — (Rajnandini Sharma)

Note: However, the author may reproduce or authorize others to reproduce material extracted verbatim from the thesis or derivative of the thesis for author's personal use provided that the source and the Institute's copyright notice are indicated.

Acknowledgements

First of all, I am very thankful to Balaji and Lord Shiva for their constant blessings and mental support that helped me overcome all the odds. I am also grateful to the holy city Kashi for its positive vibrations and spiritual driving force. It is a great honor to acknowledge the moral & scientific support, encouragement, and guidance that I have received from different research groups and several individuals at various places and institutions during the completion of my Ph.D. thesis. Without their advice, guidance, and friendship, this work would have indeed suffered. I believe success is a collective phenomenon that you achieve with the help of many individuals. Here I am gone; name those who helped me achieve my doctorate degree successfully. I am very grateful to my Ph.D. supervisor Dr. Shrawan Kumar Mishra, for his constant efforts and for being the person who supported me in this complete Ph.D. journey. Sir, you have helped me grow independentally and taught me how to work as a team member. You have also provided me opportunities to develop my technical skills, and I sincerely hope to continue learning from you. I am thankful to my lab members Dr. Shyam Babu, Raman, Nidhi, and Niti, and Simran for their moral support. Specially, I would like to thank Pawan for his suggestions. I am also appreciative of M.tech. students (Shantanu, Rohit, Akash, and Rakesh, Arkapravo, Abhas, and Omkar) of the quantum lab, School of Materials Science and Technology, IIT (BHU) for their stimulating discussions and teaching me the balance between research and life.

I am thankful of the Dr. V. R. Reddy, Dr. R. J Choudhary, and Prof. S. Bhunia for experimental facility of UGC-DAE CSR, Indore and RRCAT, Indore. I am also thankful toward Dr. R. Rawat for his honest advice to have something in backup for the thesis. I am also grateful of Rathore sir, and Anil sir, engineers of UGC-DAE CSR indore for the experiments perform by them. I am thankful to Shivam and Rijul sir my co-authors for the

nice feedback on the article. I would like to show gratitude towards Dr. B. Bhoi for the fruitful discussions.

I express my sincere indebtedness to Dr. E. G. Rini and Dr. Y. Choyal with deepest regards and profound respect for inspiring me for research. I also wish to express my indebtedness to Dr. Vasant Sathe, Scientist, UGC-DAE CSR, Indore, for supervising me during my M.Sc. dissertation, which builds a foundation in the arena of science.

I specially acknowledged the support of the SMST and CIF (Central Instrumental Facility), IIT BHU, Varanasi, and all its Techn. & Non-Techn. Members who have worked day and night to make this research work successful. I would also like to acknowledge all the faculty members Prof. D. pandey, Prof. R. Prakash, Prof. P. Maiti, Dr. (Mrs.) C. Rath, Dr. A. K. Singh, Dr. C. Upadhyay, Dr. B. N. Pal, Dr. S. Singh, Dr. A. K. Mishra, Dr. N. Kumar, Dr. R. Kumar, and Dr. A. Kumar of SMST, IIT (BHU), for their direct and indirect guidance. Without the facilities, equipment, and raw materials provided by SMST, this thesis work would have remained a dream. I also wish to thank the authority of INSPIRE fellowship, Department of Science and Technology, India, for providing me with the necessary permission and financial assistance for conducting this thesis work. In SMST, I have honestly enjoyed the company of Nisha, Aakansha, Priya ma'am, Priyanka, Neha, Sapna, Urvashi, Pooja ma'am, Rajnikant, Prince, Anuraag, Vipin, Sunayana, and Rajlakshmi who always been present with me to accomplish my degree fruitfully. I am also thankful to Sanjay sir for introducing this institute to me.

I am thankful towards Pravin for always motivating me and believing in my potentials. I also like to thank my friends Varsha, Shubhangi, Vivek, Saroj ma'am, Kamakshi ma'am, Noshin, Asmita, and Ankit for listening to me and constantly encouraging me throughout my Ph.D. tenure.

I would also like to thank my research progress evaluation committee (RPEC) members, Dr. Shrawan Kumar Mishra (Chairman &, Supervisor), Dr. Sandip Chatterjee (External

Expert, Dept. of Physics, IIT (BHU)), Dr. Bhola Nath Pal (Internal Expert) not only for their time and extreme patience but also for their thoughtful comments and suggestions. Thank you!

In the end, I would like to thank my mothers Mrs Saroj Sharma and late Alka Sharma and my brother Vasudev for their constant love, support and always stand stiff for me. I am also grateful to my father Mr. Chandrashekhar Sharma, my sister Divyanjali Sharma, my masi Mrs. Champa Jangir and my mamiji Mrs. Nirmala Jangir and Mrs. Sapna Jangir for there support in this endeavour. I would like to express my thank to all my extend family for there constant support and believing in me to achieve my dreams.

Abstract

The technological growth of the present world is mainly due to the invention of computers. From a huge space-occupied computer with slow processing using the cathode tubes, evolution has brought humanity to the era of laptops and mobile phones, where everything is one click away. All information is well distributed and accessible with the desire of the learner through the internet. These computers uses electronics that utilizes the charge of the electron. The electron transport gives rise to the resistance and associated Joules heating. This Joule heating limits the further compactness and fast-functioning of processor units. The transistors used in the current processor are at the edge of the faster and densification of the technology with the present electronics.

The solution of present limitation lies in the electron itself. The electron has two intrinsic properties: one is the charge on which electronics is based and the other is spin. The spin transport is free of Joule heating and this can be an alternative to the electronics for further enhancement in the technology. The dissipationless spin transport is a branch of condensed matter physics known as spintronics. If the spin current can be of various origins. Spin waves are one of them. The spin wave was predicted by Bloch in 1929, and the as the waves are propagating in the spin moment, it is named spin waves. The quanta of the spin wave are magnons. The field of spintronics that studies the processing and transportation of magnons is known as magnonics. Magnonics is compatible with electronics and spintronics. There are both metallic and insulator hosts for the magnons. Some notable metallic hosts are CoFeB, Permalloy, and Heusler alloys, and the insulators are yttrium iron garnets (YIG), and ferrites. The most popular insulating magnon host is YIG, which has the lowest reported Gilbert damping parameter. The longest free path length of magnons in μm thick YIG is a few tens of mm. The power required to excite the spin wave is very low, a few tens of dBm. Therefore, to completely eradicate

electron transport, ferromagnetic insulators are the conscious choice. There are various sophisticated methods, like pulsed laser deposition and RF-sputtering, that are utilized to deposit these ferrimagnetic insulators.

The present thesis elaborating focuses on the cost-effective deposition method of iron garnets ($Y_3Fe_5O_{12}$: Yttrium Iron Garnet (YIG) and $Tm_3Fe_5O_{12}$: Thulium Iron Garnet (TmIG)) using sol-gel-based spin coating method. The magnetic resonance properties of both polycrystalline and epitaxial thin films have been investigated using ferromagnetic resonance (FMR) and superconducting quantum interference device (SQUID)-vibrating sample magnetometry (VSM). On the same hand YIG is the lowest reported Gilbert damping parameter system, makes potential significance in many applications. On other hand TmIG has the spin-orbit torque phenomenon, making them an excellent host of magnonic applications. The polycrystalline YIG and TmIG samples were deposited on thermally oxidized Si (100) substrates, and the epitaxial YIG and TmIG thin films were deposited on the $Gd_3Ga_5O_{12}$ (GGG) (111) substrates. The lab source and synchrotron X-ray diffraction (XRD) studied the phase confirmation of thin films. Thickness estimation is performed using X-ray reflectivity (XRR) and cross-sectional scanning electron microscopy (SEM). Topography and morphologies of thin films were analyzed using atomic force microscopy (AFM) and SEM. The stoichiometry of the constituent with the ionic state has been confirmed by utilizing X-ray photoelectron spectroscopy (XPS). The confirmation of the ferrimagnetic ordering, along with the low-temperature compensation in the TmIG, has been performed using the SQUID-VSM. The estimation of the effective magnetization has been performed using FMR. The dissipation factors of the magnetic energy have also been estimated using the FMR.

This thesis presents an optimization of the annealing duration of polycrystalline YIG thin film deposited using the sol-gel-based spin coating on the thermally oxidized Si(100) substrate. The XRD confirms the high crystallinity deposition of the YIG above 5 hrs

annealing. XPS confirms the oxygen deficiency in the YIG annealed for 10 hrs, which supports the SQUID-VSM data for the lower magnetization in the 10 hrs sample. The lower intensity of the FMR signal also supports the annealing for the 5 hrs for polycrystalline YIG deposition for the YIG samples. Further gyromagnetic ratio and effective magnetizations along with Gilbert damping parameter is studied in the YIG 5 hrs samples. The crossectional SEM shows the thickness of the deposited thin film is 20.18 $\pm$ 2.92 nm. The Gilbert damping parameter estimated is α = 4.75 $\times 10^{-3}$, which is an order higher than PLD-grown samples along with the higher extrinsic dissipation linewidth of 5mT. Therefore, The epitaxial thin film of the YIG has been deposited on the GGG(111) substrate. The synchrotron XRD confirms the excellent crystallinity of the deposited thin films. The elemental analysis is performed using the XPS. The presence of Fe^{3+} in the sample confirms that stoichiometry is maintained. The thickness of the deposited thin film is estimated to be 18 nm using XRR. The topography confirms the average roughness of 0.4 nm. The FMR study suggests that the effective magnetization is lower than the saturation magnetization with strong the presence of anisotropy in the epitaxial YIG. The stress calculation shows that the major contribution to the magnetic anisotropy in the YIG is because of stress-induced anisotropy. The high crystalline sample has a higher damping parameter but less inhomogeneous contribution to the linewidth 2 mT.

This thesis also presents the study of the polystalline TmIG samples. The XRD study confirms the single-phase polycrystalline TmIG on the thermally oxidized Si (100) substrate. The XPS study of the TmIG is done first time in this thesis. The XPS handbook is utilized to confirm the Tm^{3+} state along with the Fe^{3+} cationic state. The low-temperature magnetization of the TmIG is studied with the experimental determination of the compensation temperature $\approx$ 15 K. The room temperature ferrimagnetic ordering with the low-temperature modulated ferromagnetic ordering is confirmed experimentally with the magnetic hysteresis loop. The further epitaxial thin film of the TmIG on the GGG(111)

substrate is deposited utilizing the sol-gel-based spin-coating method. The synchrotron XRD is utilized to confirm the deposited thin film's excellent crystallinity and interfacial roughness. Thickness is estimated of the deposited thin film is 12.25 nm using XRR. The perpendicular magnetic anisotropy (PMA) presence in the deposited thin film is confirmed with polar magneto-optical microscopy. The origin of this PMA is the stress-induced anisotropy is presented in the thesis. The FMR is used to estimate the uniaxial anisotropy with the Landé g-factor 1.391 $\pm$ 0.006 because of the high spin-orbit coupling of the f-orbital of thulium cation. The Gilbert damping parameter is estimated α = 0.0216 $\pm$ 0.0028. The quality of the deposited TmIG is found to be equivalent to the PLD-grown samples of TmIG, making it a potential method to deposit the rare-earth iron garnets. This cost-effective method of sol-gel-based spin coating with the presence of a clean room and a controlled oxygen environment can be used for the applications.

Table of contents

List of figures

List of tables

List of Abbreviations

YIG	Yttrium Iron Garnet
TmIG	Thulium Iron garnet
GGG	Gadolinium Gallium Garnet
FMR	Ferromagnetic Resonance
XRD	X-ray Diffraction
XPS	X-ray Photoelectron Spectroscopy
AFM	Atomic Force Microscopy
SEM	Scanning Electron Microscopy
MPMS	Magnetic Property Measurement System
SQUID	Superconducting Quantum Interference Device
VSM	Vibrating Sample Magnetometry
JCPDS	Joint committee on powder diffraction standards
FCC	Field Cooled Cooling

XRR	X-ray Reflectivity
FMI	Ferromagnetic Insulators
PLD	Pulsed laser Deposition
LPE	Liquid Phase Epitaxy
GIXRD	Grazing Incident X-ray Diffraction
FCW	Field Cooled Warming
SOC	Spin-orbit Coupling
PMA	Perpendicular Magnetic Anisotropy
MOKE	Magneto-optic Kerr Effect

List of Symbols

Å	Angstrom
λ	Wavelength
nm	Nanometer
μm	Micrometer
M_{eff}	Effective Magnetization
M_S	Saturation Magnetization
K_U	Uniaxial Anisotropy Constant
K_S	Shape Anisotropy Constant
K_σ	Stress-induced Magnetic Anisotropy

Chapter 1

Introduction

1.1 Introduction

The twentieth century has been an era of technological evolution, and at the end of this century, every household was equipped with personal computers. This century has seen the development of computers of the size of a room to their evolution to be as compact as fit in a lap. The twenty-first century is moving towards more compact and faster personal computers, advanced supercomputers, and futuristic quantum computers. The development of current computers is based on electronics. Electric charge motion has drawbacks in requiring a significant amount of current, and it causes natural resistance by producing Joule heating. As the size is reduced, these challenges have been enhanced and the need for a less heat-producing way of transport has been studied. One way of doing it is using the electron's spin component and properties that function on spin current. The electron transport that is based on spin is spintronics. Now, many advanced scientific studies are focusing on the development of spintronics because the scientific community sees the future in them. To fasten and densify the transport and memory, it is essential to understand and enhance our knowledge about spintronics((70, 7, 104)). The origin of spintronics has been materialized by the discovery of giant magnetoresistence (GMR) in magnetic/nonmagnetic

superlattice by A. Fert and P Grünberg((44, 16)). The collective work of GMR awarded Nobel prize in 2007 for their contribution in Physics. With the discovery of the spin valve, the memory storage's densification has upgraded. Spintronics has many application, a few of them has been discussed in Figure (1.1). GMR and Tunneling magnetoresistance (TMR) has made hard disk drive (HDD) more compact ((48)).

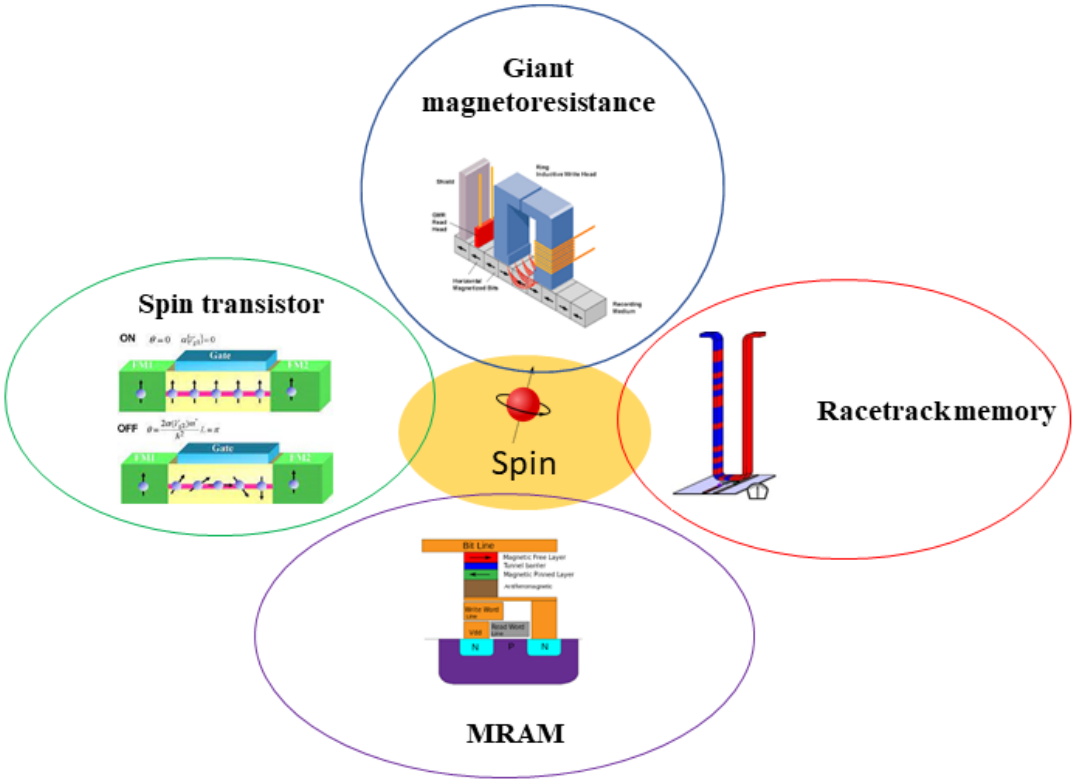

Fig. 1.1 The major applications of spintronics.

Understanding of the presence of spin phenomenon has been advanced by presenting the idea of spin injection by Datta and Das in 1990 ((35)). They proposed the electro-optical modulation replacement by the electric spin-oriented field effect transistor (spin FET). A successful demonstration of the spin-polarized Light Emitting Diode (Spin LED) was done in 2001 by Zhu *et al.* ((136)). Along with the electron-based spin current, the more dynamic spin wave-based spin current has also found its experimental observation

((81)). Bloch predicted a spin wave in 1929 ((17)). The excitation of the magnetic ordering behaves as the wave propagating, and its quanta is magnon. Magnon has opened a new area of research to get Joule heating free information transfer ((28, 110)). The field of data processing and information transfer using magnon is known as Magnonics. There are various advantages of using magnon in the information processing; they are as follows:

- Magnon based processing can harness the superposition phenomenon.
- Processing dimensions can be reduce to few tens of nm.
- Magnon gives freedom to work in GHz-THz range.
- They can overcome the Joule heating losses.
- Various transistor based on the magnon-magnon interaction can be build at low currents.

Magnonics has opened whole new possibilities not only for device fabrications but also for understanding the physics behind them. Magnonics has applications in logic gate operations, analog data processing, oscillators, and resonators. There are various conducting and insulating magnonic crystals. These are CoFeB, permalloy (NiFe), YIG, rare-earth iron garnets, and Heusler alloys. This thesis deals with the magnonic crystals YIG and TmIG. Both are insulating ferrimagnets and have long spin wave propagation distances and low damping parameters. There are various synthesis methods to synthesize these. The thesis is based on a cost-effective method, all solution-based spin coating. It is not as much as the explored synthesis method when we talk about iron garnets. For the basic understanding of the properties of these magnonic crystals, Ferromagnetic resonance (FMR) has been utilized. In the following section, a detailed description of the purpose of choosing iron garnet and FMR is elaborated.

1.2 Why Iron Garnets?

Garnet is an old English word meaning "dark red", as the abundant garnets are of dark red color. natural garnets are found worldwide. Iron garnets were synthesized in the laboratory by Bertaut and Forrat in 1956 ((11)). Yttrium iron garnet (YIG) was the very first garnet invented. Later on, various single-crystal and polycrystalline rare-earth garnets were synthesized. Complete lanthanide elements have been utilized to substitute yttrium in iron garnets. ((56)). YIG has been utilized extensively to study magnon properties, as it has the lowest ferromagnetic resonance linewidth and lowest reported Lorentz damping parameter 4.2×10^{-4} ((38)). The smaller the linewidth, the lesser the dissipation of the spin wave energy. There are various contributions of the dissipation: 1) extrinsic, and 2) intrinsic. Spin-orbit coupling, electron-electron interactions, and relaxation of the spin in the direction of the applied field contribute to the intrinsic dissipation. The magnon-magnon scattering, and the presence of defects contribute to the inhomogeneous extrinsic dissipation. YIG has utilized to understand these contributions extensively ((72, 116, 71, 43)). To get the epitaxial YIG as a thin film, gadolinium gallium garnet (GGG) is used as substrate. The lattice mismatch between YIG and GGG is 0.61% ((121)), makes less strained thin film, and cause the absence of perpendicular magnetic anisotropy (PMA). The substituted GGG are used to generate the PMA in the thin film ((87)). It is essential to have PMA in the present day to densify further the information, spin polarization, magneto-optical devices, spin-torque oscillators, and magnon valves ((128, 75, 33)).

The substitution of rare-earth at the yttrium site in YIG results in the presence of PMA and high spin-orbit coupling (SOC). This substitution changes the magnetic behavior of the iron garnet at low temperatures ((56)). Figure (1.2): depicts the magnetic behavior of the various rare-earth iron garnets. There is a presence of compensation temperature. The lowest compensation temperature belongs to thulium iron garnet (TmIG) and ytterbium

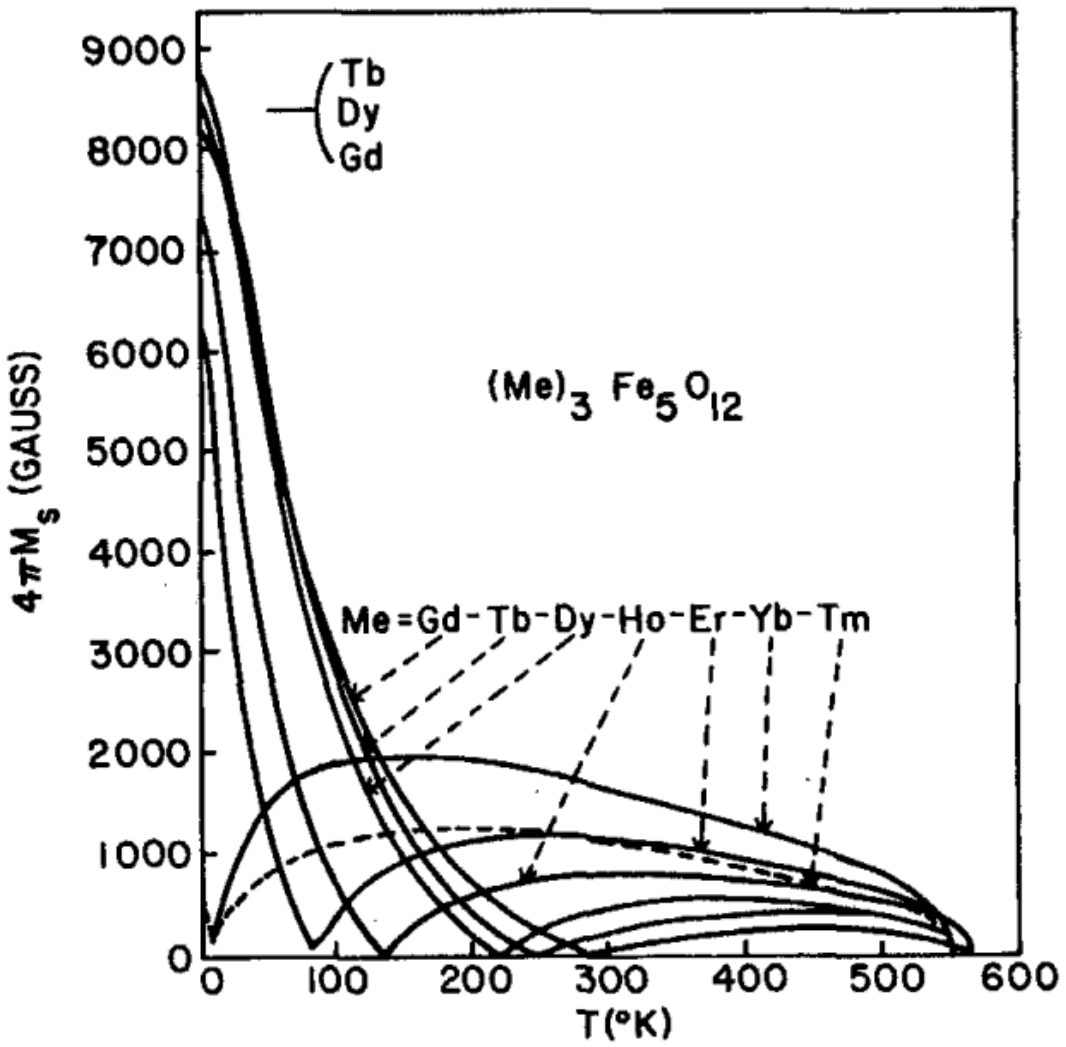

Fig. 1.2 Magnetization as a function of temperature for rare-earth iron garnets (adopted from ((56))).

iron garnet. This thesis discusses the TmIG due to its low compensation temperature and presence of high SOC and PMA in thin film on GGG ((52, 124)). The presence of the spin-orbit torque opens wide magnonics applications for the TmIG/Pt heterostructures.

1.3 Significance of Ferromagnetic Resonance

Knowing the materials analyzed in the thesis is essential but it is also essential to the method used to characterize the materials. The prominent method used is Ferromagnetic resonance (FMR). FMR was discovered in 1946 by Griffith ((59)), and its delineation was done by Kittel in 1947 ((77)). It is a century-old technique but still relevant because of the results it provides to confirm application in modern spintronics. Applications of this method have evolved with the advancement in synchrotron sources and in inverse spin Hall effect utility. Without harming the sample its magnetic dynamics can be analyzed using broadband FMR. Broadband FMR is able to measure the gyromagnetic ratio, saturation magnetization, and Gilbert damping parameter((123)).

Magnetic excitons have a tendency to precess in the presence of the external field. This precess motion is probed using the external microwave source. Microwaves in the range of GHz frequency are utilized to excite the spin waves ((61)). This excitation resonated with the microwaves. This resonace is the key characteristics of the present work. By knowing the dynamics by Landau-Liftsitz- Gilbert equation and the Kittel equation of the relation of net magnetization, magnetic anisotropy, resonance field, and frequency of excitation make this technique a non-destructive method to analyze the materials constants ((77, 91)).

This thesis utilized the broadband FMR of GHz frequency to explore the static and dynamic magnetic parameters of the ferrimagnetic insulators.

1.4 Outline of the thesis

The present thesis is organized into eight chapters as follows

Chapter 1 describes the motivation, introduction, and background behind the selection of iron garnets as ferrimagnetic insulators for magnonics-related studies. The use of FMR with its advantages is also discussed.

Chapter 2 elaborates on the theoretical background of the exchange, super-exchange, anisotropy, the ferromagnetic resonance conditions, and the magnetic damping factors of the magnetic energy.

Chapter 3 provides a detailed synthesis method, i.e., sol-gel-based spin coating. The working principles and the setup of the characterization methods are explained in a very concise manner. The characterization methods discussed are XRD, XRR, SEM, AFM, XPS, SQUID-VSM, and FMR.

Chapter 4 discusses the optimization of the annealing duration for the single-phase polycrystalline YIG deposition using sol-gel-based spin-coating on a thermally-oxidized Si (100) substrate. The stoichiometry of the element is conformed using XPS. The comprehensive FMR study of a 20.18 nm thick YIG thin film is discussed. The lowest solution-based Gilbert damping $\alpha = 4.754\times10^{-3}$ is presented.

Chapter 5 discusses the epitaxial growth of the YIG on the GGG (111) single-crystal. The 18 nm thick YIG epitaxial thin film of excellent crystallinity is comprehensively studied to estimate the Gilbert damping parameter $\alpha = 8.83\times10^{-3}$ and the inhomogeneous damping. The presence of the stressed-induced anisotropy as a major contributor to the uniaxial anisotropy is presented.

Chapter 6 discusses the polycrystalline 22 nm thick TmIG thin film synthesized with all solution-processed methods. The elemental constituents' atomic percentages are estimated using the XPS and found under consideration. The low-temperature compensation

temperature is experimentally confirmed in the thin films. The low temperature and room temperature magnetic behaviour are explored.

Chapter 7 discusses the epitaxial 12.25 nm thick TmIG thin films comprehensively. XRD-based strain-induced anisotropy is estimated. The excellent crystalline TmIG thin film is confirmed with the Laue oscillations in the XRD. The Gilbert damping parameter is equivalent to the pulsed laser-deposited thin films.

Chapter 8 summarises the final experimental findings of the present thesis and discusses related future prospects.

Chapter 2

Theoretical Background

2.1 Basics of Magnetic energies

Understanding the magnetic ground state of the system is possible with basic theoretical background knowledge. This thesis deals with the ferromagnetic resonance study of the insulating ferrimagnetic systems with the lowest reported Gilbert damping parameter. The basics of magnetism that can help to understand the physical significant terms are discussed in this chapter. Here, a brief introduction to the exchange interaction, specially superexchange is discussed. Along with exchange interaction, magnetization dynamics using the Landau-Lifshitz- Gilbert equation will be touched to give an overview of the magnetic dynamics in ferrimagnetic systems. After stating the equation, its term for the dissipation of magnetic energy has also been briefly discussed. Magnetic materials possess spontaneous magnetization, that makes them promising in various applications like memory, computation, compass, etc. To have enhanced understanding, it is essential to investigate the properties' basic fundamentals. This chapter is focused on such a perspective that helps to build a basic foundation on various significant aspects.

2.1.1 Exchange energy

The Weiss molecular field theory was unable to explain the reason behind the ferromagnetic state of transition metals. Thereafter, in 1928, Heisenberg proposed the Hamiltonian for the ferromagnetic state ((68)). Considering the example of the hydrogen molecule, Heisenberg explained the ground state using a quantum mechanical approach. He considered two Hydrogen atom with wavefunction (Ψ) by combining spatial (ϕ) and spin (χ) wavefunctions. $\Psi = \phi\chi$. The final Ψ has to be asymmetric. For spatially symmetric wave function, the spin wavefunction has to be antisymmetric and vice versa. The probability of asymmetric spatial wavefunction suggests the localization of electrons around the separate atoms, and the probability of symmetric wavefunction suggests the sharing of electrons by both atoms equally. He stated that the two electrons being identical can be exchanged between the two hydrogen nuclei. This interaction between exchangeable electrons was termed an "exchange interaction". The Hamiltonian for Heisenberg exchange interaction is expressed as follows:

$$H = -2\sum_{i<j}^{N} J_{ij}\hat{S}_1.\hat{S}_2 \tag{2.1}$$

where J is exchange integral, $\hat{S_1}$ and $\hat{S_2}$ spin vectors of atom 1 and atom 2, respectively. The value of J decides whether spins will be aligned parallel or anti-parallel. Figure 2.1: depicts the wavefunction and probability density in the hydrogen molecule

Equation for exchange integral (J) is as follows:

$$J = \frac{E_S - E_T}{2} \tag{2.2}$$

where E_S is the energy of the singlet spin wavefunction and E_T is the energy of the triplet spin wavefunction. If E_S is lower, then J is negative, which means it is an antiferromagnetic ground state, and if E_T is lower, J is positive and supports a ferromagnetic ground state.

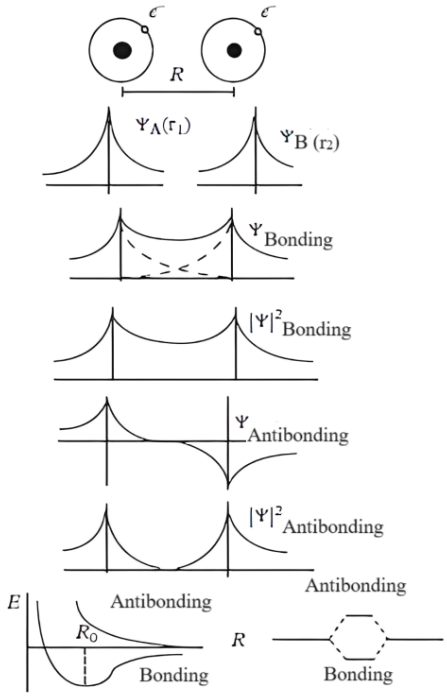

Fig. 2.1 The interaction between two hydrogen atoms based on bonding and anti-bonding of the wavefunctions. Figure adopted from ((81)).

There are broadly two types of exchange interactions, i.e., direct and indirect exchange. When the two magnetic species interact directly without the intermediate species, known as direct interaction, for example, $Co_{23}Fe_{11}Cu_{66}$, CoFeB. When the exchange interaction is intermediated by nonmagnetic species like oxygen or electrons, it is known as an indirect exchange interaction. The indirect exchange that happens in the electron gas is known as Ruderman-Kittel-Kasuya-Yoshida (RKKY) interaction and the oxygen intermediated exchange between two similar species is known as super-exchange if it happens between two different cationic states is known as the double exchange. There is an asymmetric exchange known as Dzyloshinskii-Moriya interaction that gives rise to interesting spin textures. Iron garnets show the super-exchange kind of indirect exchange interaction. Super-exchange is explained in detail as follows.

Superexchange energy

Metals have free electrons, which makes it difficult to study the underlying exchange interaction. In the case of transition metal oxides covalent bonding is present, which facilitate localized electron which helps in studying the magnetic order with ease. Taking the example of MnO, oxygen-mediated superexchange interaction is shown. The mediating O^{2-} orbital show (p-d) σ or $\sigma*$ bonding with 3d orbitals of Mn^{2+}. Due to Pauli's exclusion principle, these electrons shared within Mn^{2+}-O^{2-}-Mn^{2+} orbitals are an antiferromagnetic couple to each other depicted in Figure: (2.2) that shows how p_z orbital of O^{2-} overlap with the Mn^{2+} cation and electronic configuration of p and d orbitals. Completely filled O^{2-} behave as mediator of the antiferromagntic coupling with Mn^{2+} transition metals ((81, 32, 18, 96)).

There are set of rules for the superexchange interaction known as Goodenough-Kanamori rules attribute that superexchange interaction is antiferromagnetic in nature when the virtual electron transfer is between two half-filled orbitals. In contrast, superexchange

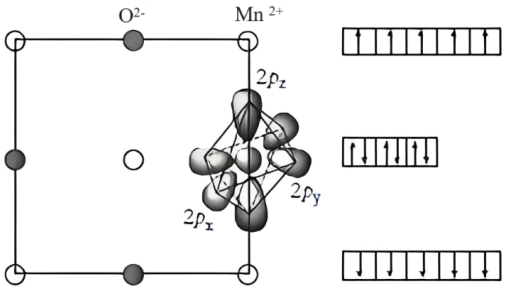

Fig. 2.2 Orbital structure of linearly coupled Mn^{2+} and O^{2-} cation in Mn^{2+}-O^{2-}-Mn^{2+} configuration in MnO. Electron configuartion of 3d, and 2p orbitals, coupled using antiferromagnetic superexchange interaction, adopted from ((81)).

interaction changes into a ferromagnetic nature when it is between half-filled to empty orbital or filled to half-filled orbitals ((57)).

In iron garnets the Fe^{3+} cations interact with the mediating O^{2-} anions, similar to the Mn^{2+} and O^{2-} interactions. The half-filled d-orbital of alike cations are antiferromagnetically coupled as per the Goodenough-Kanamori rule. This half-filled orbital give rise to uncompensated moment gives rise to the ferrimagnetic ordering in the iron garnets.

2.1.2 Magnetic anisotropy

The scalar Heisenberg interaction presents a picture of isotropic exchange in the ferromagnets as well as antiferromagnets and ferrimagnets. In reality, the magnetization is anisotropic in nature. This anisotropy could be because of the crystallographical axes, stress, and shape of the sample. The iron garnets have cubic magnetocrystalline anisotropy, because they are thin film, demagnetization energy gives rise to the shape anisotropy and there is a strain in the thin film film because of the lattice mismatch in the substrate and YIG and TmIG. A brief introduction to anisotropy is as follows.

Magneto-crystalline anisotropy

Magnetization of the magnetic systems is dependent on their crystallographic directions. This anisotropy in magnetization due to the crystallographic direction is known as magneto-crystalline anisotropy. This arises as a result of spin-orbit coupling in the material. Orbitals due to the crystal field affect the spin orientations, this asymmetry gives rise to magneto-crystalline anisotropy. Iron garnets have a combination of uniaxial and cubic magnetocrystalline anisotropy. The axis along which the magnetization saturates at a low magnetic field is the easy axis and the highest magnetic field required to saturate the magnetization is the hard axis. In cubic crystals, magnetic anisotropy is known as cubic magneto-crystalline anisotropy. Let α_1= cos a, α_2 = cos b, and α_3 = cos c be directional cosine of magnetization vectors. The anisotropy energy density of the cubic crystals is as follows:

$$E_{mc} = K_0 + K_1(\alpha_1^2\alpha_2^2 + \alpha_2^2\alpha_3^2 + \alpha_3^2\alpha_1^2) + K_2\alpha_1^2\alpha_2^2\alpha_1^2 + ... \tag{2.3}$$

where, K_0, K_1, and K_2 are the different order contributions of the anisotropy constant at a certain temperature. The higher-order constant is neglected here. In this case, K_2 is very small and therefore can be neglected. As the K_0 term has nonangular dependence and as here we only see the difference in the anisotropy energy, therefore, it is neglected. For both YIG and TmIG is K_1 is -1.1 $\times 10^3$ N/m^2 ((14, 29)).

Stress-induced anisotropy

A thin film is grown over a single crystal substrate. The interface constraints the lattice parameter of the grown thin film. This asymmetry breaks the symmetry of the grown thin film. The lattice mismatch between the bulk and interface gives rise to a stress-induced anisotropy. The magnetic energy variation arises due to the strain in a system known as

magnetostriction and magnetoelastic energy. Stress-induced anisotropy is presented as follows:

$$K_\sigma = -\frac{3}{2}\lambda_{111}\sigma \tag{2.4}$$

where, K_σ is stress-induced anisotropy constant, λ_{111} is magnetostriction constant along (111) direction, and σ is stress in the direction. λ_{111} values for YIG and TmIG are -1.7 $\times 10^{-6}$ and -5.2 $\times 10^{-6}$, respectively. The stress-induced anisotropy makes a major contribution to the epitaxial iron garnet thin films. In TmIG, lattice mismatch causes perpendicular magnetic anisotropy in the deposited thin films.

Shape anisotropy

There is an internal counter force applied on the magnetization of the magnetic matter to oppose it. This energy is also known as shape anisotropy and magnetostatic energy. Figure: (2.3) showing the magnetic lines of field of (a) H field, and (b) B field in a bar magnet. Middle direction notation shows B and 4πM are parallel and H_d (demagnetization field) is anti-parallel to them. As demagnetization energy opposes the magnetization of the magnetic materials, it is applied internally unlike a stray field.

Energy equation for the demagnetization is as follows:

$$E_{demagnetization}/Volume = \mu_0 \int_0^M H_d.dM(SI) \tag{2.5}$$

H_d can be calculated using below equation:

$$H_d = -N_d.M \tag{2.6}$$

N_d is a demagnetization tensor (dimensionless) depending on the geometry of the sample and M is magnetization. Here, equation (2.6) shows demagnetization field is the opposite

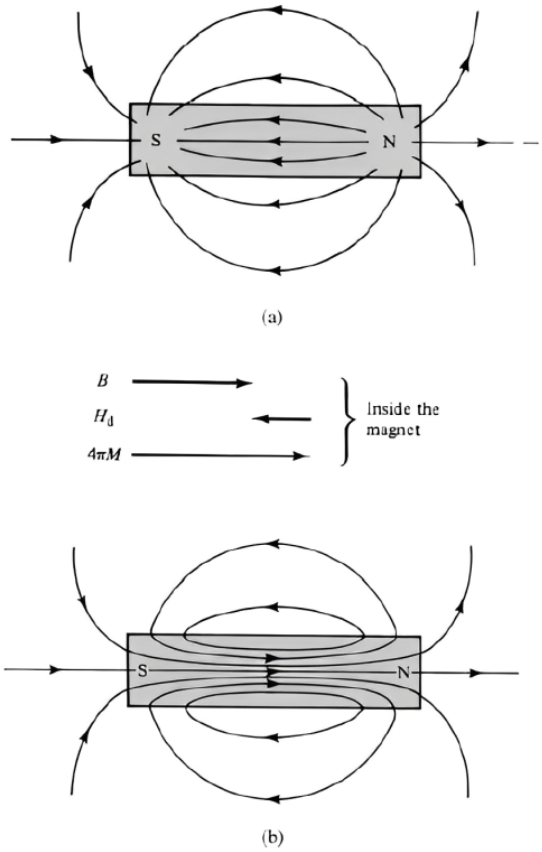

Fig. 2.3 Field lines of a bar magnet in absence of external field. (a) H field, and (b) B field. Middle arrows shows the direction of the B, H_d (demagnetization field) and 4πM at the center of the bar magnet adopted by ((18)).

of the magnetization of the magnetic matter. The E_d decreases with the formation of the domain walls.

2.1.3 Zeeman energy

According to Pauli's exclusion principal state that no two electrons can occupy a similar quantum number state in an atom. Electrons have four quantum numbers, principle quantum number (n), azimuthal quantum number (l), magnetic quantum number (m_l) and spin quantum number (m_s). The value of l lies 0,1,2,...,n-1 and m_l vary from -l,....-1,0,1,....l. The value of m_s is $\pm \frac{1}{2}$. The magnetic quantum number is degenerated in the absence of an external magnetic field. Application of external field breaks this degeneracy as presented in Figure (2.4).

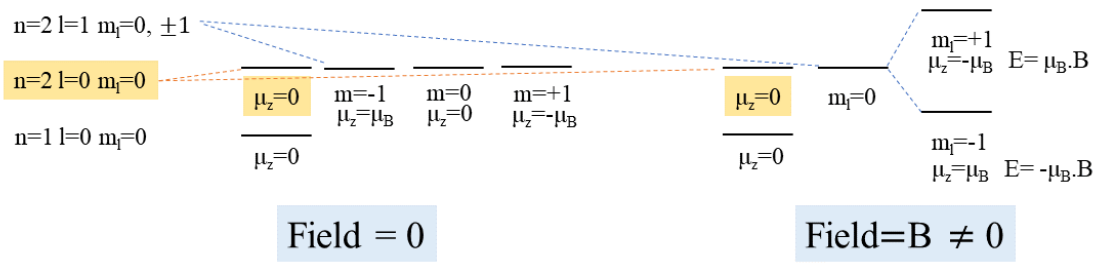

Fig. 2.4 Energy level spliting in absence and presence of external magnetic field.

Take an example of l=1 state which is a three-fold degenerate state (m_l=0, ±1) that breaks into three different energy states with energy -μ_BB, 0, and +μ_BB. This phenomenon of non-degeneracy is known as the "Zeeman effect" ((81, 32, 18)). These split energy levels absorb the microwave and show resonance. This resonance probes the magnetic properties of the sample. FMR is a spectroscopy technique based on this resonance.

2.2 Magnetism dynamics

Ferromagnetic resonance is the result of the precession of the magnetization around the external magnetic field. It is time time-dependent field causing the precession due to exposing matter to GHz frequency waves and shows absorbtion at that field. The magnetic external field at which absorption occurs is known as the resonance field. The energy losses happen with the precession with the time duration of tens of nanoseconds. These energy losses give rise to the linewidth in the resonance spectra. The Landau-Lifshitz equation is a mathematical way to understand the precession of magnetization and was further added by Gilbert to incorporate the damping term, final equation is known as the Landau-Lifshitz-Gilbert equation. This equation and its terms are elaborated in this section of the thesis.

2.2.1 The Landau-Lifshitz-Gilbert equation

The Landau-Lifshitz-Gilbert equation shows the time-dependent proceeding of the magnetization in an effective field. Landau and Lifshitz on the basis of the theory of Larmor precession determine the precession component of magnetization. But along with precession, energy losses are also present. These energy losses are such that they try to damp the precession amplitude and this damping was formulated by Gilbert in the 1950s ((55)). Collectively this equation of precession and damping is known as the Landau-Lifshitz-Gilbert equation and is written as follows:

$$\frac{dM}{dt} = \gamma[M \times H_{eff}] - \alpha[M \times \frac{dM}{dt}] \tag{2.7}$$

where, γ is gyromagnetic ratio, α is Gilbert damping constant, and H_{eff} is effective magnetic field. Figure (2.5) (a) shows the precession of magnetization around an effective magnetic field and (b) shows the damping of the amplitude due to Gilbert damping. Here

the direction of magnetization changes but the magnitude remains constant therefore, inelastic magnon scattering is not involved in it. Damping in more detail is explained in a further section.

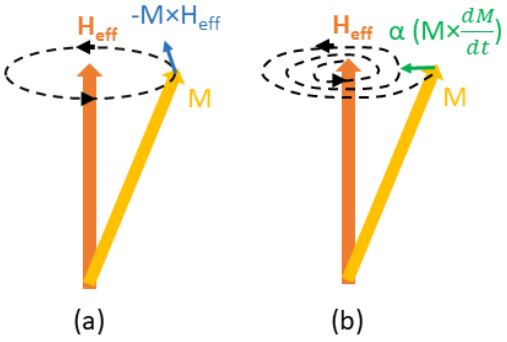

Fig. 2.5 Schematics of (a) Magnetization (M) precession and (b) damping (α) of precession around effective magnetic field (H_{eff}).

2.2.2 Resonance condition

In the presence of an external field, magnetization precesses and shows resonance under microwave exposure. From Landau-Lifshitz equation

$$\frac{dM}{dt} = -\gamma \times H_{eff} \tag{2.8}$$

Considering magnitude of magnetization is M_S.

Magnetization in spherical coordinates ($\hat{M}$, $\hat{\theta}$, $\hat{\phi}$) can be represented using cartesian coordinates as follows depicted in Figure (2.6):

$$\begin{aligned} \hat{M} &= sin\theta cos\phi\hat{x} + sin\theta sin\phi\hat{y} + cos\theta\hat{z} \\ \hat{\theta} &= cos\theta cos\phi\hat{x} + cos\theta sin\phi\hat{y} - sin\theta\hat{z} \\ \hat{\phi} &= -sin\hat{x} + cos\phi\hat{y} \end{aligned} \tag{2.9}$$

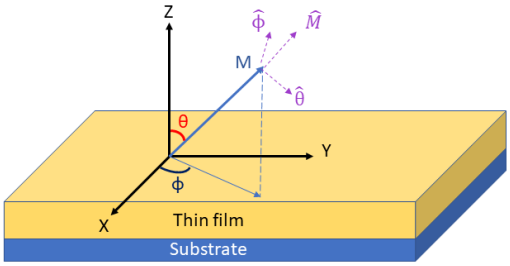

Fig. 2.6 Spherical coordinates of magnetization (M), θ, ϕ (in purple color) as function of x, y and z coordinates of the thin film.

Considering the Magnetization component, Magnetic field in spherical coordinates in terms of cartesian coordinate are as follows:

$$\begin{aligned} H &= H_M\hat{M} + H_\theta\hat{\theta} + H_\phi\hat{\phi} \\ H_M &= sin\theta cos\phi H_x + sin\theta sin\phi H_y + cos\theta H_z \\ H_\theta &= cos\theta cos\phi H_x + cos\theta sin\phi H_y - sin\theta H_z \\ H_\phi &= -sinH_x + cos\phi H_y \end{aligned} \tag{2.10}$$

Z-component of rate of change of magnetization as function of time as given in equation (2.8) can be written as

$$\frac{dM_z}{dt} = -\gamma(M_xH_y - M_yH_x) \tag{2.11}$$

substitute the value of M_x, M_y and M_z in equation (2.11) from equation (2.9) and results is as follows:

$$-sin\theta\frac{d\theta}{dt} = -\gamma sin\theta(-sin\phi H_z + cos\phi H_y) \tag{2.12}$$

$$\frac{d\theta}{dt} = \gamma H_{\phi} \tag{2.13}$$

Similarly for M_x component:

$$\frac{dM_x}{dt} = -\gamma(M_x H_y - M_y H_x) \tag{2.14}$$

$$-sin\theta sin\phi \frac{d\phi}{dt} + cos\theta cos\phi \frac{d\theta}{dt} = -\gamma(sin\theta sin\phi H_z + cos\theta H_y) \tag{2.15}$$

$$sin\theta \frac{d\phi}{dt} = -\gamma H_{\theta} \tag{2.16}$$

Effective magnetic field governing the magnetization dynamics can be derived from the free energy (F) as follows:

$$M_{eff} = -\frac{1}{M_s}\frac{dF}{dM} \tag{2.17}$$

Total free energy is combination of external field, anisotropy term, and demagnetization term. Given free energy density F, equilibrium state can be determine by minimizing it. Therefore,

$$\begin{aligned} \frac{dF}{d\theta} &= 0 \\ \frac{dF}{d\phi} &= 0 \end{aligned} \tag{2.18}$$

Deviation from equilibrium can be experessed in below equation:

$$\begin{aligned} dF = -M_s d\theta H_\phi \Longrightarrow F_\theta = \frac{dF}{d\theta} = -M_s H_\theta \\ dF = -M_s sin\theta d\phi H_\phi \Longrightarrow F_\phi = \frac{dF}{d\phi} = -M_s sin\theta H_\phi \end{aligned} \tag{2.19}$$

The equation of motion can be expressed in derivative of free energy,

$$\begin{aligned} \frac{d\theta}{dt} = -\gamma H_\phi = -\gamma \frac{F_\phi}{M_s sin\theta} \\ sin\theta \frac{d\phi}{dt} = -\gamma H_\theta = -\gamma \frac{F_\theta}{M_s} \end{aligned} \tag{2.20}$$

Taylor expansion for small deviation $\delta\theta$,$\delta\Phi$ will be

$$\begin{aligned} F_\theta = F_{\theta\theta}\delta\theta + F_{\theta\phi}\delta\phi \\ F_\phi = F_{\phi\theta}\delta\theta + F_{\phi\phi}\delta\phi \end{aligned} \tag{2.21}$$

Therefor, the equation of motion become:

$$\begin{aligned} \frac{d\delta\theta}{dt} = -\frac{\gamma}{M_s sin\theta}[F_{\phi\theta}\delta\theta + F_{\phi\phi}\delta\phi] \\ sin\theta_0 \frac{d\delta\phi}{dt} = \gamma M_s [F_{\theta\theta}\delta\theta + F_{\theta\phi}\delta\phi] \end{aligned} \tag{2.22}$$

For Harmonic solution considering $\delta\theta \approx e^{iwt}$ and $\delta\phi \approx e^{iwt}$ will be:

$$F_{\theta\theta}F_{\phi\phi} - F_{\phi\theta}F_{\theta\phi} = -M_s^2 sin^2\theta \frac{w^2}{\gamma^2} \tag{2.23}$$

$$w_{res} = \frac{\gamma}{M_s sin\theta_0}\sqrt{F_{\theta\theta}F_{\phi\phi} - F_{\phi\theta}F_{\theta\phi}} \tag{2.24}$$

Consider an in-plane magnetized thin film with uniaxial anisotropy that align the magnetization in equilibrium. There are various ennergy term envolve in the resultant magnetization orientation, these energies are as follows:

- Zeeman energy as a result of external in-plane applied field in y-axis F_Z=-M_S $\hat{M}$. H = -M_S H m_y.
- Uniaxial anisotropy that tries the in-plane alignment of magnetization F_U= - K M_y^2.
- Demagnetization as result of opposition internal moments to magnetization F_d= - $\frac{M_S}{2}$ $\hat{M}$. H_d. H_d is demagnetization field equals to -M_S N $\hat{M}$. N is demagnetization tensor whoes value are N_{xx}=N_{yy}=0, N_{zz}=4π. Therfore, F_d=2$\pi M_S^2 m_z^2$
- In thin film inetrface between film and substrate also impact anisotropy of the film. This anisotropy also effect the magnetization orientation. The inetrface energy of the following form: F_i= $\frac{-K_i}{t_{fm}} M_z^2$ which is equivalent to the voltage controlled magnetic anisotropy effect. The resultent

$$\begin{aligned} F &= -M_S H m_y - K m_y^2 + 2\pi M_S^2 m_z^2 - K_t m_z^2 \\ &= -M_S H m_y - K m_y + \frac{M_S}{2}[4\pi M_S - \frac{2K_t}{M_S}] m_z^2 \\ &= -M_S H m_y - K m_y + \frac{M_S}{2} H_\perp m_z^2 \\ &= -M_S H sin\theta sin\phi - K sin^2\theta sin^2\phi + \frac{M_S}{2} H \perp cos^2\theta \end{aligned} \tag{2.25}$$

By minimizing the free energy equilibrium orientation of magnetization can be determined as follows:

$$\begin{aligned} F_\theta &= -M_S H cos\theta sin\phi - 2K sin\theta cos\theta sin^2\phi - M_S H_\perp sin\theta cos\theta \equiv 0 \\ F_\phi &= -M_S H sin\theta cos\phi - 2K sin^2\theta cos\phi sin\phi \equiv 0 \end{aligned} \tag{2.26}$$

After substituting $\phi = \frac{\pi}{2}$, therefore voltage controlled magnetic anisotropy can shift magnetization orientation in y-z plane. Therefore, condition for θ will be

$-M_S \cos\theta[H+ (H_K+H_\perp)\sin\theta]=0$

where, $H_K = 2K/M_S$ is the uniaxial anisotropic field. The solution from the above equation will be 1. $\theta = \frac{\pi}{2}$ 2. $\sin\theta = \frac{-H}{H_K+H_\perp}$

The angle $\theta \in [0,\pi]$. Therefore expect results are as follows 1. for $H_K+H_\perp>0$, $\theta=\frac{\pi}{2}$; 2. for $H_K+H_\perp<0$, $H<(H_K+H_\perp)$, $\sin\theta = \frac{H}{|H_K+H_\perp|}$

Case I : $\theta = \frac{\pi}{2}$, $\phi = \frac{\pi}{2}$

The second derivative of free energy will be

$$\begin{aligned} F_{\theta\theta} &= -M_S H sin\theta sin\phi - 2K cos2\theta sin^2\phi - M_S H_\perp cos2\theta \\ &= M_S H + 2K + M_S H_\perp \\ F_{\phi\theta} &= -M_S H cos\theta cos\phi - 2K sin2\theta cos\phi sin\phi = 0 = F_{\theta\phi} \\ F_{\phi\phi} &= -M_S H sin\theta sin\phi - 2K sin^2\theta cos2\phi = M_S H + 2K \end{aligned} \tag{2.27}$$

Therefore,

$$\begin{aligned} w_{res} &= \frac{\gamma}{M_s sin\theta_0}\sqrt{F_{\theta\theta}F_{\phi\phi} - F_{\phi\theta}F_{\theta\phi}} \\ &= \frac{\gamma}{M_s}\sqrt{(M_S H + 2K + M_S H_\perp)(M_S H + 2K)} \\ &= \gamma\sqrt{(H + \frac{2K}{M_S} + H_\perp)(H + \frac{2K}{M_S})} \\ &= \gamma\sqrt{(H + H_K + H_\perp)(H + H_K)} \end{aligned} \tag{2.28}$$

The resonance condition for case I is: $M_{eff} = H_K + H_\perp$

$$w_{res} = \gamma\sqrt{(H + M_{eff})(H)}$$

Case II : $H_K+H_\perp<0$, $H<(H_K+H_\perp)$, $\sin\theta = \frac{H}{|H_K+H_\perp|}$

Second derivative of free energy is

$$\begin{aligned}
F_{\theta\theta} &= -M_S H sin\theta sin\phi - 2K cos2\theta sin^2\phi - M_S H_\perp cos2\theta \\
&= \frac{M_S H^2}{|H_K + H_\perp|} - M_S(H_K + H_\perp)(1 - \frac{2H^2}{(H_K + H_\perp)^2}) \\
&= M_S|H_K + H_\perp| - \frac{M_S H^2}{|H_K + H_\perp|} \\
F_{\phi\theta} &= -M_S H cos\theta cos\phi - 2K sin2\theta cos\phi sin\phi = 0 = F_{\theta\phi} \\
F_{\phi\phi} &= -M_S H sin\theta sin\phi - 2K sin^2\theta cos2\phi \\
&= \frac{M_S H^2}{|H_K + H_\perp|} + 2K\frac{H^2}{(H_K + H_\perp)^2} \\
&= \frac{M_S H^2}{|H_K + H_\perp|}(1 + \frac{H_K}{|H_K + H_\perp|})
\end{aligned} \tag{2.29}$$

Therfore,

$$\begin{aligned}
w_{res} &= \frac{\gamma}{M_s sin\theta_0}\sqrt{F_{\theta\theta}F_{\phi\phi} - F_{\phi\theta}F_{\theta\phi}} \\
&= \frac{\gamma}{M_s}\sqrt{(M_S|H_K + H_\perp| - \frac{M_S H^2}{|H_K + H_\perp|})(\frac{M_S H^2}{|H_K + H_\perp|}(1 + \frac{H_K}{|H_K + H_\perp|}))} \\
&= \gamma\sqrt{(1 + \frac{H_K}{|H_K + H_\perp|})[(H_K + H_\perp)^2 - H^2]}
\end{aligned} \tag{2.30}$$

The resonance condition for the case II is

$$w_{res} = \gamma\sqrt{(1 + \frac{H_K}{|M_{eff}|})[(M_{eff})^2 - H^2]}$$

where, $M_{eff} = H_K + H_\perp$

2.3 Magnetization damping

The relaxation of the magnetic systems is important because of its importance in spin wave propagation and spin pumping. To give an easy flow to the spin waves, relaxation should be

small. Relaxation depends on the both intrinsic and extrinsic properties of the system. This relaxation is also called damping. Linewidth in FMR is the result of these relaxations. The damping in magnetic systems can be broadly divided into Gilbert and non-Gilbert damping. The intrinsic damping of the system is called Gilbert damping as it was calculated by the Gilbert in 1950s. The nonhomogeneous contribution due to magnon-magnon scattering is the non-Gilbert damping in magnetic systems. By plotting the linewidth as a function of the frequency both intrinsic and extrinsic contributions can be separated as given in below equation:

$$\Delta H = \Delta H_0 + \frac{4\pi\alpha}{\gamma} f \tag{2.31}$$

where, ΔH is linewidth, ΔH_0 is an inhomogeneous contribution to the linewidth, α is the intrinsic Gilbert damping parameter, and f is the frequency of microwave radiation. In this section, both intrinsic and extrinsic contributions are discussed in detail.

2.3.1 Intrinsic damping

Landau - Lifshitz magnetic dynamics equation was enriched with the damping of magnetization by Gilbert in the 1950s ((55)). In this section of magnetic dynamics, the damping in the precessing magnetization in the presence of an external magnetic field was assimilated and the famous magnetic dynamics equation Landau-Lifshitz- Gilbert equation was stated. This equation is elaborated in section 2.2.1 of this thesis. This Gilbert damping parameter originates because of the intrinsic properties also known as the intrinsic damping. The system itself has intrinsic damping based on the electrons and their interaction with the phonon and the spin-orbit coupling. The unconserved spin of relaxation gives its origin to the spin-orbit coupling of the system. If the spin-orbit coupling is absent gives that the intrinsic damping vanishes out. The term Gilbert damping constant α has been discussed in this section. The Gilbert damping constant is intrinsic in nature. It gives the behavior of

the sample as per its quality and extrinsic defects do not come into consideration((69)). The first principle calculations have proven the α is as follows:

$$\alpha = \frac{ie\hbar\mu_0 M_S}{8m_0^2c^2}(1-\chi_m^{-1}) \tag{2.32}$$

where, χ_m is magnetic susceptibility. begin with the relativistic Dirac-Pauli Hamiltonian and solving it considering the spin-orbit coupling gives the above result. α has intrinsic properties and this thesis studies this property to evaluate the quality of the deposited thin films. The smaller the α the more number of cycles needed for magnetization to be at equilibrium. YIG is the lowest reported α material.

2.3.2 Extrinsic damping

The inhomogeneous extrinsic contribution to the linewidth comes from defects of the magnetic system that break translation symmetry. ΔH_0 is the inhomogeneous contribution to the linewidth in equation (2.31). A major mechanism for the non-Gilbert damping is two-magnon scattering ((79, 63, 135, 72)). Initially, the role of voids and porous in the nearly ideal single crystal of YIG was studied by Spark-Loudon-Kittel in 1961 ((115)). The broadening of the peak has contributed to the crystal quality. The defects and pores play a major role in the relaxation processes. The spin wave propagation is hindered by the grain boundaries and the defects in the system. This role can be distinctly understood in polycrystalline and epitaxial thin films.

Chapter 3

Synthesis and Characterization Techniques

3.1 Overview

The backbone of the experimental work is to understand the instruments and their principle behind its functioning. The present thesis deals with the experimental study, therefore, it is essential to give a prospective on the experimental instruments. The understanding of the instrument gives an additional advantage on the results that need to explain. The instrumental background is essential to experimental study. Therefore, the current chapter presents a brief introduction to the method of the synthesis and the characterization methods. The thesis is based on the cost effective method of deposition, i.e. sol-gel-based spin-coating. This chapter gives an comprehensive detail of synthesis along with the X-ray diffraction, X-ray reflectivity, Atomic force microscopy, scanning electron microscopy, X-ray photoelectron spectroscopy, magnetic property measurement system, and the Ferromagnetic resonance.

3.2 Synthesis method

The method of deposition used in this thesis is sol-gel-based spin coating. Iron garnets thin films can be prepared using liquid phase epitaxy (LPE) ((41)), pulse laser deposition (PLD) ((20, 15, 119)) and rf-sputtering ((39, 37, 88)). All the above process require sophisticated instruments and are expensive methods. One alternate of these methods is all wet chemical based methods, sol-gel-based spin coating is one of them. To deposit the sample using sol-gel-based spin-coating, it is essential to clean the substrate and prepare the solution of appropriate molarity to get enough grain density on the substrate, spin coating speed, and duration. All these factors are comprehensively discussed in the following subsections. The basic reaction for the chemical synthesis is as follows:

$$3X(NO_3)_3 + 5Fe(NO_3)_3 = X_3Fe_5O_{12} + 12N_2O_5 \tag{3.1}$$

where, X is yttrium (Y) or thulium (Tm).

3.2.1 Substrate Cleaning

To grow the thin film over the substrate, it is essential to clean the substrate to free it from dust and any organic and inorganic residue. Firstly, to remove the dust and any residue substrate is, clean with soap water with cotton buds by rubbing soapy bud in a circular motion. Rinse substrate with deionized water (DI), sonicate it for 30 minutes in DI water, then 30 minutes sonication in Acetone, and Isopropyl alcohol, respectively that remove any dust and other unwanted species of the substrate surface. At the end of activating the substrate surface and burning organic residue, the substrate is plasma cleaned at atmospheric pressure.

3.2.2 Solution preparation

For the solution of precursors, $Y(NO_3)_3.6H_2O$ or $Tm(NO_3)_3.6H_2O$ and $Fe(NO_3)_3.9H_2O$ were dissolved in 2-methoxyethanol in 3:5 ratio forming 400 mM solution. pH is maintained to 2-3 using diethylamine. This precursor solution was stirred for three days on a magnetic stirrer at room temperature. Prior to the day of deposition, solution is filtered using syringe filter of 0.47 μm pore size.

3.2.3 Spin Coating and annealing procedure

Figure (3.1) shows the schematic of the deposition procedure. Cleaned thermally oxidized Si substrate is drop casted and spin coated at 4000 rpm for 30 s and to evaporate the solvent from coated substrate, it is heated at 363 K for 2 hrs, followed by green heating at 623 K for 30 min for the organic compound dissociation. and final product is annealed at 1173 K for 5 hrs (for YIG) and 1223 K for 3 hrs (for TmIG) to get single phase iron garnet.

3.3 Characterization Techniques and their principles

3.3.1 X-ray Diffraction

X-rays were discovered by German physicist R*ö*ntgen in 1895. X-rays propagate in straight line, can diffract and interfere. There are various application of x-ray in field of medical, chemistry and physics. Its first application was in radiography by physician to observe the broken bones. Later soon by physicist to see through the opaque things due to its penetration capability of lighter elements. In 1912, after the discovery of the basic nature of X-rays, X-ray diffraction (XRD) through the crystals have observed and utilized. As x-rays have wavelength of few Å that is of the order of the inter planar distances in the crystals. This potential property of x-ray makes them a handy tool to dig out the crystal

Fig. 3.1 Schematic of spin coating deposition.

structure of the materials. Materials scientists along the chemists, physicists and various engineers utilized this characterization method to confirm the crystalline state of the solids. Discovery of the XRD was done by the M. Von Laue in 1912, the simpler explanation to the XRD was done by W.H. Bragg and W. L. Bragg in 1913 ((45)).

Working Principle

The XRD was explained by Laue using scattering of the X-ray from the atoms. The simpler equation was presented by Braggs. They assumed the atoms are arranged in the periodic planar manner and interplanar distance gives the diffraction at various angle based on their (hkl) and wavelength of the incident X-ray. The uncomplicated equation originate by them is as follows:

$$2dsin\theta = n\lambda \tag{3.2}$$

Figure (3.2) is the schematics of the Bragg's assumption taking the each layer of the atoms in the unit cell is a plane and the diffraction of the incident X-ray wavelength these planes. The wavelength of the incident X-ray is λ and the interplanar distance be d. Assuming the concept of the constructive interference, the path difference between the X-rays travel between two successive layer is equals to n λ. where, final equation becomes equation (3.2) ((32)).

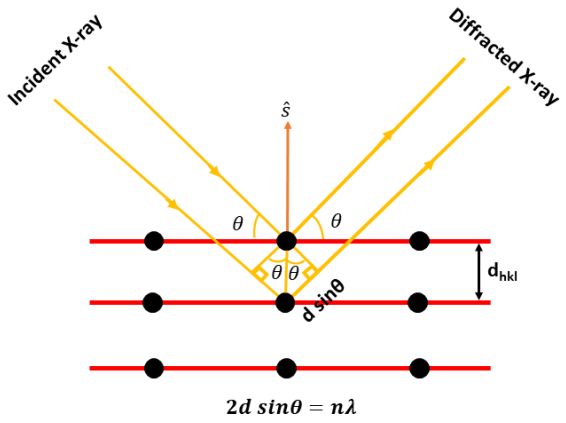

Fig. 3.2 Schematic of Bragg's equation.

Instrumentation

Figure (3.3) depicts the XRD instrumentation, comprise of the X-ray source, sample Goniometer, and Detector. X-ray source is fabricated of anode and cathode sealed in vacuum tube. AC current is passed through the anode (tungsten filament), that emits electron which streaks the cathode (Copper connected with the water cooling system). These streaking electron cause knock out of core electrons in the cathode and further de-excitation of higher orbital electron by emission of the X-rays. These X-ray comprise of bremsbelag and the characteristic emission peaks. Among these K_α has been separated

by using Ni edge. In this thesis Cu K_α has been utilized, having wavelength 1.5406 Å. There is a presence of $K\alpha_1$ and $K\alpha_2$ due the low wavelength separation between two. Both $\theta/2\theta$, and $\omega - 2\theta$ measurements has been done in Bragg-Brentano geometry. This thesis

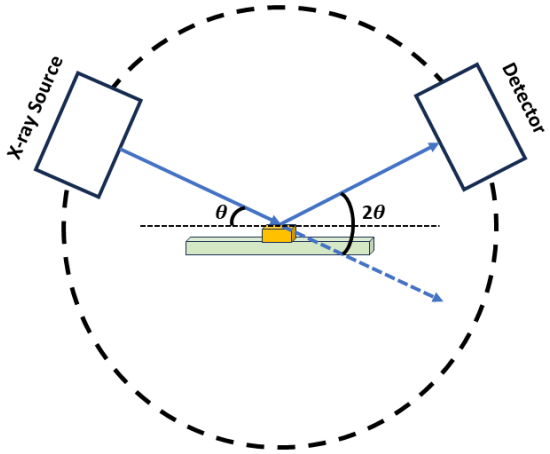

Fig. 3.3 Schematic of instrument of the XRD .

discusses te XRD of both polycrystalline and epitaxial thin films. In epitaxial films only single family of the planes present as the other plane normal [hkl] is not parallel to the diffraction vector ($\hat{S}$). Brukar D8 and Panalytical X'Pert Pro diffractometer with Cu-K_α (λ = 1.5406 Å) as a radiation source are used in the present thesis for the polycrystalline samples. For the epitaxial thin films grazing-incident XRD has been done at INDUS2 (BL13), of the RRCAT, Indore at 10 KeV energy of the wavelength 1.24 Å. Joint Committee on Powder Diffraction Standards (JCPDS) files are used to confirm the experimental XRD patterns. As the crystal structure is cubic, interplanar distances are are calculated using Bragg's relation 3.2. The d is used to calculate lattice parameter (a) using:

$$d = \frac{a}{\sqrt{h^2 + k^2 + l^2}} \tag{3.3}$$

3.3.2 X-ray Reflectivity

X-rays are the noninvasive tool to study the properties of the crystals. X-ray Reflectivity (XRR) is characterization based on the efficiency of this band of electromagnetic spectrum. XRR based on the total external reflection of the X-ray from the layered structures. Each layer has different electron density and the relative electron density of the layer decides the critical angle of total external reflection in the spectra. Reflection from the different layers form the Fresnel fringes. The periodicity of the Kiessig fringe depend on the thickness of the layers. Surface, and interface roughness decides the slop of the spectra. As the roughness increases the more X-ray get scattered and reflectivity reduces that reduce the slop. Brukar D8 (similar to XRD) is used to perform XRR on the thin films. XRR can differentiate thicknesses from 1 Åto 4000 Å. Roughness analyzed in the range of 0 - 20 Å.

Working principle

Parratt formulism and Fresnel reflection principle is used to understand the total external reflection of X-ray in thin films. Reflectivity as function of wave vector is as follows:

$$R(q) = \left| \frac{q - \sqrt{q^2 - q_C^2 - \frac{32i\pi^2\beta}{\lambda^2}}}{q + \sqrt{q^2 - q_C^2 - \frac{32i\pi^2\beta}{\lambda^2}}} \right|^2 \tag{3.4}$$

where, q is $\frac{4\pi}{\lambda}\ \sin\theta$, and $\theta_C = q_C \frac{\lambda}{4\pi}$. At various q value reflectivity vary differently and the different conditions are as follows:

1) if q<q_C, total external reflection occurs and R=1.

2) if q=q_C, Reflection reduce extensively.

3) if q>q_C, R decreases with $\frac{1}{q^4}$ as R= $\frac{q_C^4}{16q^4}$

Based upon the Fresnel reflection multilayer XRR analysis is performed using Parratt's formulism. This thesis used Parratt32 to perform the fittings based on Parratt formulism.

3.3.3 Atomic Force Microscopy

A three-dimensional microscopy performed by contact of the nano-probe and sample surface is atomic force microscopy (AFM). Surface morphology study of the non-conductive samples for the surface texture and the roughness estimation. AFM can be performed in contact, tapping and non-contact mode. The separation between probe and sample cause the bending of cantilever in different orientation. Figure (3.4) shows the different modes with probe-sample separation.

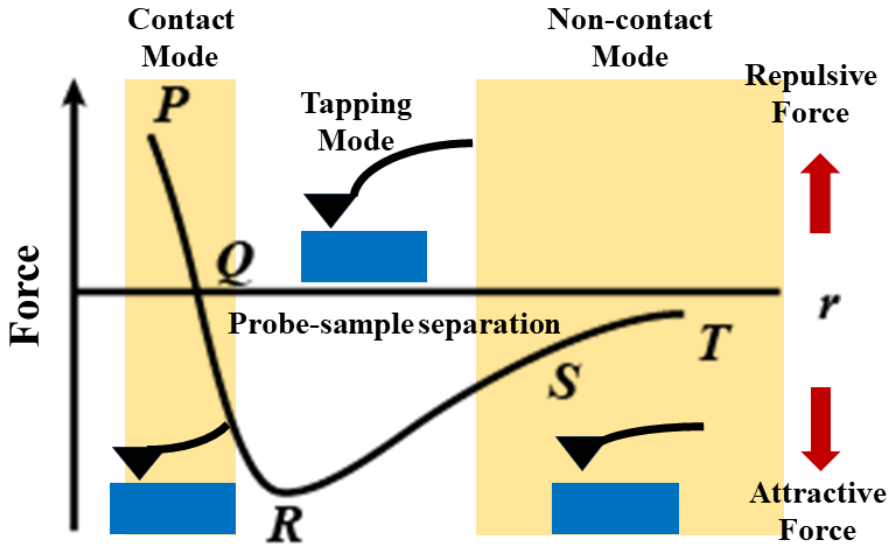

Fig. 3.4 Different mode of AFM with respect to separation between probe and sample.

Working Principle and Instrumentation

AFM setup comprises of laser, probe attached to the cantilever adjusted by the piezoelectric scanner, sample stage, and the photodiode detector. Figure (3.5) depicts the instrumentation of the AFM. Sample is exposed to the tip of probe that is connected with the piezoelectric scanner to tune the distance between probe and sample. Laser is focused on the top of the tip that dependent on its position, reflect the laser to the photodiode. If the laser is at

the center it is at zero feedback. If it get deflected it gives feedback to the piezoelectric scanner to move the probe and that value is registered as data. This data as function of distance of scanning forms the surface morphology micrograph.

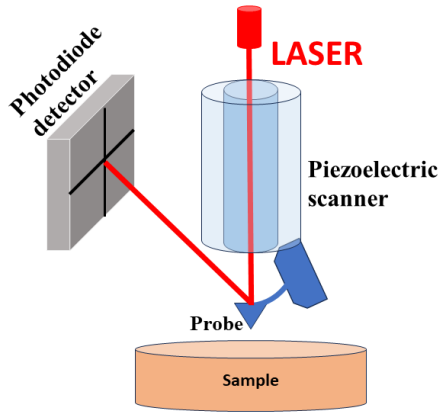

Fig. 3.5 Schematics of the instrumentation of Atomic Force Microscopy.

Bruker Anasys nano-IR3 in contact mode is used to perform AFM in this thesis.

3.3.4 Scanning Electron Microscopy

Microscopes helps to magnifies the object and observes the surface topography along with some elemental properties of the samples. Initially, visible light was used to magnify the objects. Magnification of these microscopes varied from 500X to 2000X. In light microscopes, glass lenses were used. Electron beam can be focused using electromagnetic lens. These principle was used and focus the electron beam and various microscopic method has been invented. Scanning electron microscopy (SEM) is one of them. It used the secondary electrons to image the surface with the magnification of 100,000X. SEM uses raster scanning process.

Working Principle

Figure (3.6) depicts the interaction of electron beam with the sample and as result secondary electrons, backscattered electrons, Auger electrons, characteristic X-rays, Cathodoluminescence, and continuum X-rays emits. Out of these, secondary electron can gives the topographical information of the sample. Characteristic X-rays give the elemental composition of the sample.

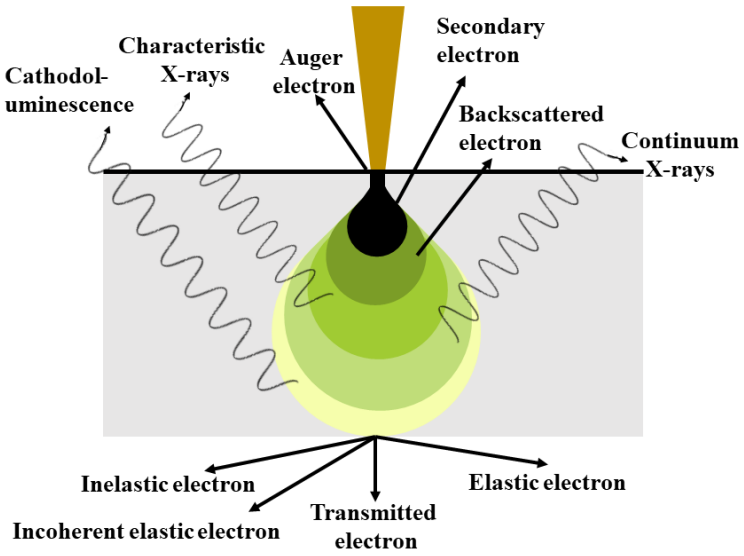

Fig. 3.6 The interaction of focused electron beam eject out different kind of electrons and X-rays.

Instrumentation

SEM is high vacuum microscopic instrument. Figure (3.7) depicts schematics of the components in SEM. The setup is consists of electron source, initially tungsten filament nowadays, field-emitting guns (FEG) are used. FEG are also made of tungsten but in form of tip (0.5 nm). They work on low temperatures, in the presence of anode to eject out and accelerate the electrons. These electron are accelerated using scan tilt and focused using condenser lenses. These electrons are passed through scanner coil to focus the specific

area. These focused beam cause the emission of the electron and X-rays as depicted in Figure (3.6). Among these secondary electron are collected by the Everhart–Thornley detector.

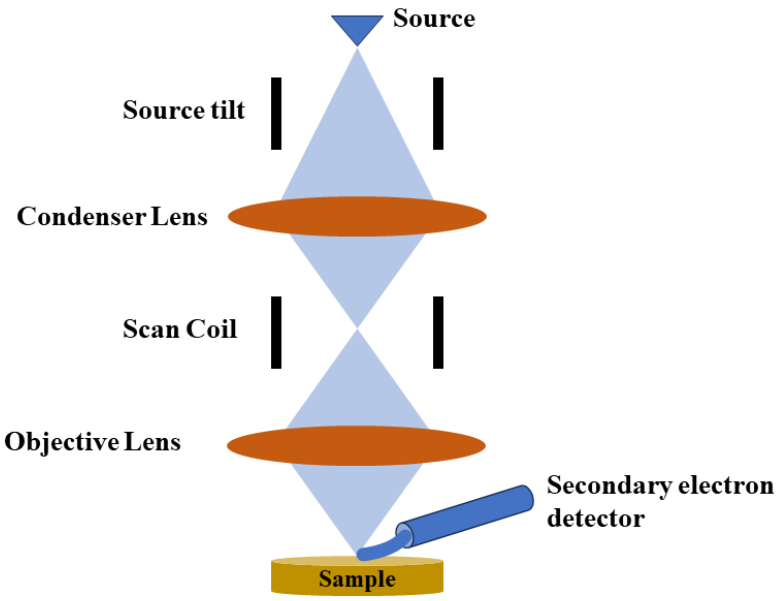

Fig. 3.7 Instrumentation of Scanning Electron Microscope.

In this study, insulating samples have been studied therefore, few nm thick gold coating used to overcome screening effect of the electron. A field emission gun-based scanning electron microscope (FE-SEM) of SIGMA, ZEISS have been used in the presented thesis. Inge processing is performed using the ImageJ software ((1)).

3.3.5 X-ray Photoelectron Spectroscopy

As previously discussed X-ray based studies like XRD, and XRR, X-ray Photoelectron Spectroscopy (XPS) is more sophisticated, ultra-high vacuum based method to dig out the information from the characteristic binding energy of the core electrons of the elements. XPS is surface-sensitive X-ray-based spectroscopy to determine the chemical composition

with the valence state of the constituents. XPS is also known as electron spectroscopy for chemical analysis (ESCA).

Working Principle

XPS is based on the photoelectric effect. Photoelectric effect was discovered by Hertz in 1887, and Einstein utilizing the concept of quantization of energy packets (quanta) to explain it in 1905 for which he was awarded the Nobel Prize in 1912. Another Nobel prize was given to Kai Seigbahn in 1981 for his invention of the XPS instrument in 1954 at Uppsala University. X-ray shined on the sample surface cause ejection of the electron and by measuring the energy of the ejected electron, nature of constituents and their environment is unleash, using the following equation,

$$E_B = E_P - (E_K + \phi) \tag{3.5}$$

where E_B is binding energy, E_P is incident photon energy, E_K is kinetic energy of ejected electron and ϕ is work function of the instrument and sample. When X-ray are shined over the material, its core electron get eject out when the incident X-ray energy is higher then the work function of the material and rest of energy is converted into the E_K of the ejected electrons. If we take a difference of the incident energy , work function, and E_K we get the E_B a finger print of the element. Figure (3.8) depicts a specimen spectra and the schematic of the electronic configuration of element.

Instrumentation

Figure (3.9) depicts the schematics instrumentation of the XPS that comprise of a X-ray source, sample holder, analyzer, detector, signal processor and read out. Here, aluminium is utilized as the cathode for X-ray waves. Quartz as monochromator is used to separate the K_α, centering at 1486.7 eV energy and bandwidth of 0.3 eV. This monochromatic

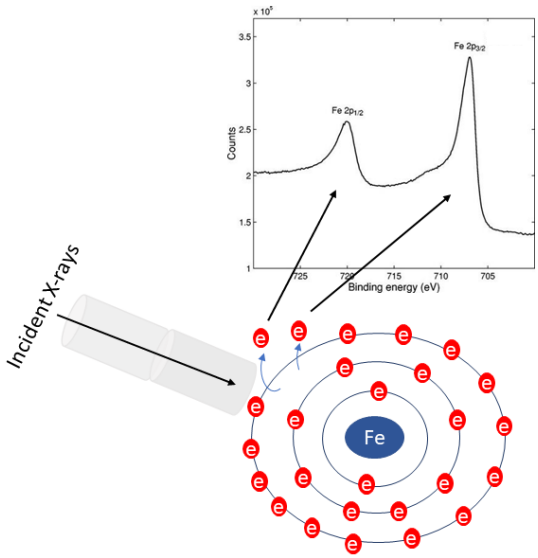

Fig. 3.8 Schematic of photoelectric effect in XPS.

light is focused on the sample surface. photoelectron ejected collected and passed to the hemispherical analyzer to separate the electron on the basis of their kinetic energy. This counts of that specific kinetic energy is converted into binding energy and is plotted as the spectra. K-Alpha model of the Thermo Fisher Scientific is used to perform XPS in the

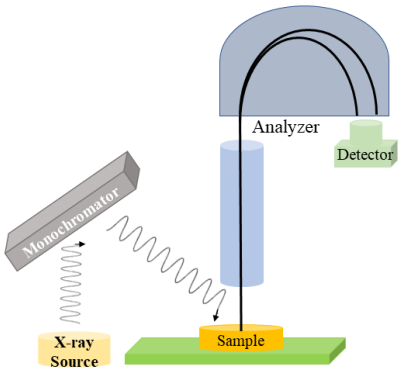

Fig. 3.9 Schematic of instrumentation of XPS.

present thesis. For this sample preparation chamber is vacuumed to $\approx 10^{-8}$ Torr, followed

with the final chamber vacuum to $\approx 10^{-9}$ Torr. All core level XPS spectra were calibrated with respect to the C_{1s} peak centered at ≈284.8 eV.

3.3.6 Magnetic Property measurement System

Magnetic Property Measurement System (MPMS) is the most sensitive magnetic moment measurement system that has sensitivity up to 10^{-8} emu. It is versatile in measuring powder, thin films, single crystals, etc., and is widely used in materials science. MPMS combines vibrating sample magnetometry (VSM) and superconducting quantum interference device (SQUID). Where VSM gives rise to the flux change in the SQUID that measures the moment of the sample, in the following section, the principle of VSM and SQUID will be discussed.

Working Principle

VSM working Principle

VSM works on the principle of Faraday's law of electromagnetic induction. Current in closed circuit is induced in the opposite direction when it is exposed to the varying magnetic flux ((96)). This statement can be written as:

$$\varepsilon = -N\frac{\Delta\phi}{\Delta t} \tag{3.6}$$

Where, ε is induced electromotive force, ϕ is flux.

SQUID working Principle

SQUID works on the principle of the Josephson tunneling effect. In 1962, Brian David Josephson theoretically predicted the tunneling of Cooper pairs from the insulating gap between two superconducting materials ((74)), which was later experimentally shown by

Philip Anderson and John Rowell ((2)). When an insulating or normal metal thin layer is sandwiched between two superconducting, Cooper pairs tunnels through that insulating or regular conducting layers similar to electron tunnel through insulating layers in quantum tunneling. The current flow through circuit will be

$$I = I_0 sin(\delta) \tag{3.7}$$

I_0 is maximum current flow through the tunneling and δ is phase difference between the current of two superconducting layers.

$$\dot{\delta} = \frac{d\delta}{dt} = \frac{2eV}{\hbar} = \frac{2\pi}{\phi_0} V \tag{3.8}$$

where, ϕ_0 is flux quantization (h/2e) and V is volatge develope across the junction.

MPMS uses DC-SQUID in which two parallel Josephson junctions sense the voltage induced due to tho change in flux. Figure (3.10) depicts the schematic diagram of DC-SQUID ((30)). Figure (3.10) depicts the DC SQUID biased with current (I) and I bifurcate in two arms having value (I/2). Each Josephson junction cause change in phase difference of current passing through junctions and their interference at output current. Current induced (J) is due to applied flux causing phase difference in current flow and above I_C, Voltage is induced as a function of applied change in magnetic flux. This induced voltage gives the moment of the samples.

Figure (3.11) depicts the IV characteristics of DC SQUID. Above I_C Voltage start to generates (I_0). IV characteristics at half integer and integer flux quanta is have different critical current. Voltage measured as function of applied flux. Magnetometry measurements are conducted at Quantum design MPMS3.

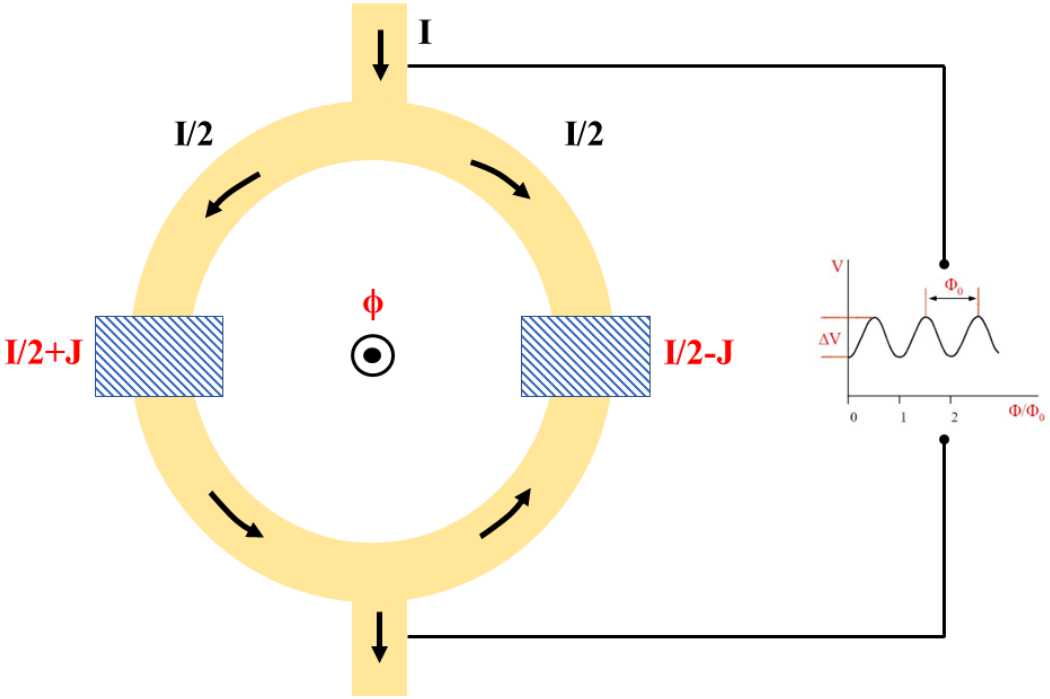

Fig. 3.10 Schematic of Superconducting Quantum Interference device.

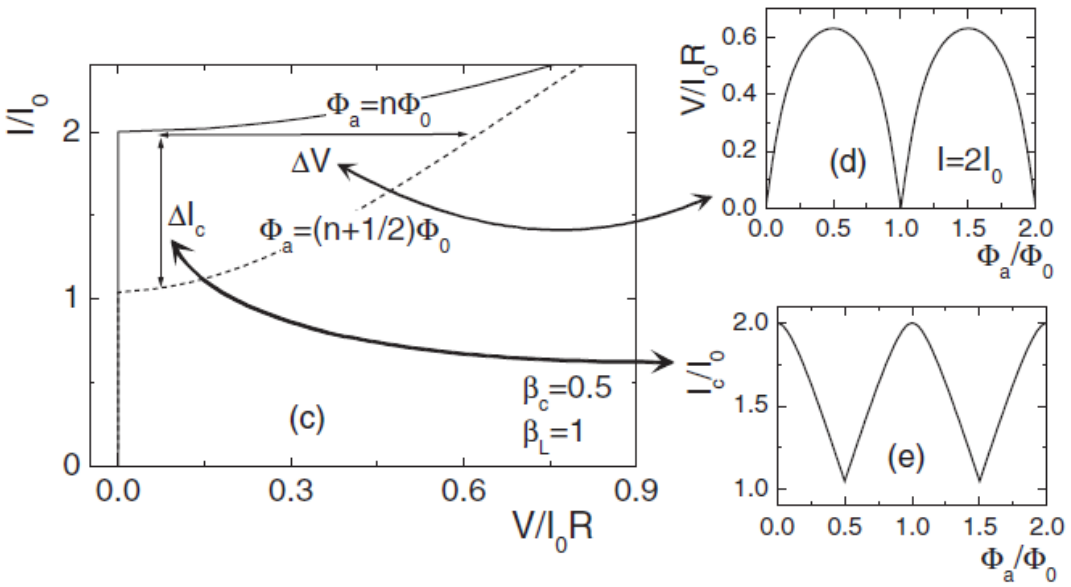

Fig. 3.11 IV characteristics od DC SQUID with current and voltage variation as a function of flux quantum ((30)).

DC Magnetometry

Magnetic materials have the transition from paramagnetic to ferromagnetic or antiferromagnetic phase as the function of the temperature. The magnetization of materials Vs temperature at certain applied field gives the signature of these transition. Magnetization attain zero value at T_C and further decrease in the temperature enhance the moment till the mK temperature. At mK it shows the highest magnetization by overcoming all thermal vibrations. This behavior is shown by ferromagnetic materials. Antiferromagnetic material's magnetization at T_N starts to decrease, as the moments begin to align in anti-parallel manner. YIG and TmIG are antiferromagneticaly coupled ferrimagnets. At higher temp 100 K these materials shows the ferrimagnetism gives the T_C at $\approx$ 560 K. In TmIG on lowering the temperature Tm^{3+} ion begin to contribute and the moments decreases at T_N an reached a compensating temperature where it shows the minima with further increment due the moment contribution of the Tm^{3+}.

Zero field Cooling (ZFC): Sample is cooled in the absence of the magnetic field. The warming cycle magnetization as a function of temperature is measured in presence of the external magnetic field. This method gives the sponteneous magnetization as a function of temperature is experimetally observed.

Field Cooled Cooling(FCC): Sample is cooled in the presence of certainly feeble magnetic field and magnetization as function of temperature is measured in cooling cycle.

Field Cooled worming (FCW): This process is similar to ZFC but at the time of Cooling certainly small field is applied.

Above three magnetometry modes have been utilized to probe the magnetic transitions in the thin films.

AC Magnetometry

DC magnetometry has limitation to certain frequency of the sample oscillations. AC magnetometry can overcome that. Inspite of oscillating sample, a time dependent ac field is applied along the the external DC field. This induce the flux in the SQUID, to observe the susceptibility (M/H) of the sample. This mode is not absolute, based on the measurement of the slope of the magnetization Vs magnetic field. The advantage of this method is that at small change in slope no matter how high moment is, it can give the signature of the transitions. Difference between spin ice, super paramagnetic behavior can be be understood by taking the ac-susceptibility at various applied ac-magnetic field. By varying the applied DC magnetic field different section of the M(H) can be probed and the transition and magnetic behaviors can be studied.

3.3.7 Ferromagnetic Resonance

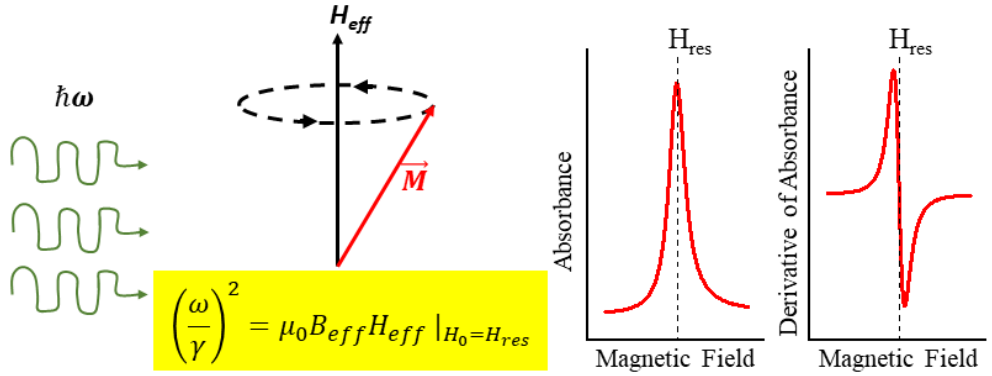

Fig. 3.12 Microwave radiation of energy $\hbar\omega$ falls on the precession magnetization (**M**) along the effective field (H_{eff}) resonate at resonance magnetic field (H_{res}) shows absorbance in the spectra. First derivative of absorbance is observed in FMR spectra.

Matter and radiation interact when the condition satisfies between the energy levels of the matter and the energy or frequency of the interacting radiation. This interaction happens

and cause emission or absorption of electromagnetic radiation. Interaction between matter and radiation are the basis of many biological (vision of eyes, sensation of heat with nervous system of the body) and telecommunication devices (radios, television, internet). Matter-radiation interaction helps to understand various fundamentals of matter and science experimentally. The study of this interaction as function of wavelength or frequency of radiation is termed as spectroscopy. Specific absorption or emission frequency of the radiation determine energy extent of the interaction, give details of matter, like infrared radiation gives details of rotational and vibrational energy levels of interacting materials and microwave cause molecular rotation and gives details of the electronic levels. By exposing the matter with the radiation its characteristics can be determine by absorption or emission. When the sponteneously magnetized materials (ferromagnetic and ferrimagnetic) interact with the microwave, their Larmor precession resonant with the specific frequency of the exposed frequency and shows the absorption of that specific frequency. This phenomenon is termed as ferromagnetic resonance (FMR). Ferromagnetic resonance can utilized to calculate various material specific properties like gyromagnetic ratio (γ), damping constant (α), anisotropy field (H_K) and saturation magnetization (M_S). Ferromagnetic resonance (FMR) is a spectroscopy technique that probes the precession of magnetic components and helps study the dissipative energy factor along with the characteristics of the magnetically ordered systems. With the external microwave, the precession of magnetization can be probe. FMR was discovered by Griffith 1946 ((59)) and the the first explanation of the FMR was done by Kittel in 1948 ((78)).

Working Principle

In the presence of an external magnetic Field (H_{eff}), the precession magnetization (**M**) of the sample get resonate with the frequency (ω) of an interacting microwave((12)). At constant frequency, when varying (H_{eff}) become equivalent to resonance magnetic field

(H_{res}), i.e., the condition of resonance satisfies and absorption peak is observed as depicted in Figure (3.12).

Instrumentation

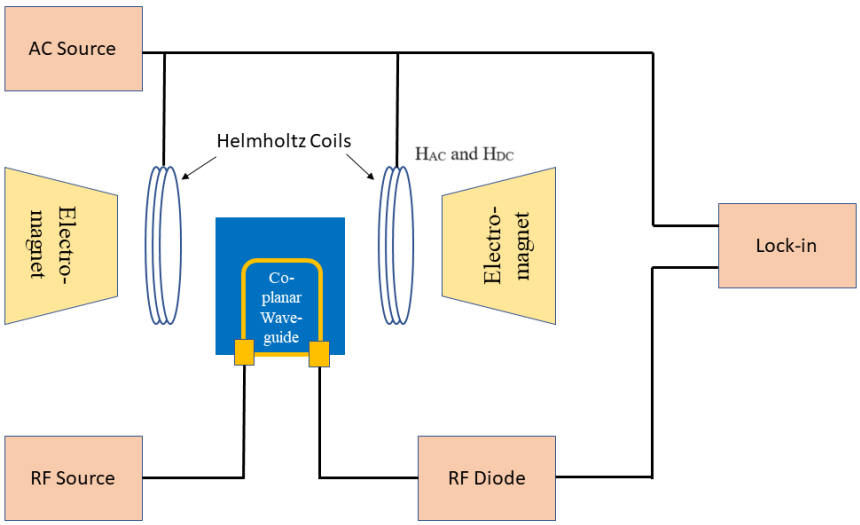

Fig. 3.13 Ferromagnetic resonance experimental setup

In presence of external magnetic field, sample is excited using the microwave frequency. In figure (3.13) a coplanar wave guide is present in between electromagnet and helmholtz coils where electromagnet provides DC magnetic field and Helmholtz coil provide ac magnetic field. RF source act as input RF wave and as RF frequency passes through the coplanar wave guide on which the inverted sample absorb some band of frequency at resonance magnetic field. RF diode measure the absorbed frequency and lock-in amplifier enhance signal to noise ratio using ac magnetic field. For room temperature FMR, Quantum design NanoOs phase FMR has been utilized.

Chapter 4

Magnetic-ordering of polycrystalline Yttrium Iron Garnet thin film

abstract

YIG is a ferrimagnetic insulator that shows significant potential in various applications, such as spin pumping and optical devices. There are various methods through which the YIG thin film can be grown namely PLD, LPE, and rf-sputtering. These sophisticated methods require massive instrumentation. Sol-gel-based spin-coating can be a cost-effective way to deposit the YIG thin film. This chapter deals with the optimization of the growing process of YIG thin film. Here, we report the growth of uniform polycrystalline YIG thin films on thermally oxidized Si (100) substrates. X-ray diffraction confirms the single-phase formation of YIG. X-ray photoemission is used to probe the valence state of constituent elements of the ferrimagnetic thin films. The lowest Gilbert damping constant (α) = 4.754×10^{-3} with an inhomogeneous contribution to the linewidth of 5.04 mT is observed using FMR due to extrinsic inhomogeneous growth of the deposited film.

4.1 Introduction

YIG is synthetic garnet having cubic crystal structure with space group $Ia\bar{3}d$ ((54, 108)). Magnetic ion Fe^{3+} in the unit cell of crystal structure form a tetrahedron and octahedron with oxygen ion; these coordinations are antiferromagnetically coupled, as they are not equal in numbers and give rise to ferrimagnetic ordering((54, 40)). Understanding the magnetization dynamics of YIG is a fascinating research topic due to its various applications of YIG, mainly in microwave absorbance((113)), acoustic transducers((50)), and magneto-optical devices((19, 64)). Studying YIG is also essential due to the its manifestation of spin Seebeck effect in Bismuth-doped YIG ((132)) Recently, YIG's application in spin-pumping has emerged that initiate various studies((122, 67, 27)). Investigating the magnetic energy dissipation factors of the YIG materials with lower α is desirable ((31)). YIG has been grown using sophisticated deposition methods like liquid phase epitaxy, pulsed laser deposition (PLD), and sputtering ((67, 97, 21, 118, 119, 34, 62, 88, 114)). The observed value of α for YIG varies between 5.16×10^{-5} to 1.2×10^{-1}((67, 97, 21, 118, 119, 34, 62, 88, 24, 66, 114, 39, 83, 84)). The reported values of α for polycrystalline YIG deposited using co-precipitation spin-coating are ranging 2.7×10^{-2} to 1.2×10^{-1}((130)). Lower the α higher the possibility that YIG can be utilized in spin pumping.

This chapter presents a cost-effective all-solution process-based spin-coating method to deposit the YIG thin film on thermally oxidized Si substrate. We prepared the thin films with varying annealing duration and find out the appropriate annealing duration. With the optimization annealing duaration, we determine the intrinsic and extrinsic magnetic energy dissipation factors of grown YIG films using FMR techniques. We observe the lowest damping constant of sol-gel-based spin-coated YIG films.

Table 4.1 Lattice parameters and grain size of the deposited polycrystalline YIG.

Sample	lattice parameters		Crystallite size (nm)
	a=b=c (nm)	$\alpha = \beta = \gamma$(deg)	
YIG 2 hrs	1.2129	90	9.30
YIG 5 hrs	1.2509	90	20.13
YIG 10 hrs	1.2384	90	27.66

4.2 Results and discussion

4.2.1 Structural Study

Figure (4.1) shows the XRD pattern of the deposited YIG; major peaks (400), (420), and (422) have been indexed using JCPDS no. 00-033-0693 ((100, 102, 94)). The lattice parameters a=b=c for YIG 2hrs, YIG 5hrs, and YIG 10 hrs are 1.2129 nm, 1.2509 nm, and 1.2384 nm, respectively, with $\alpha = \beta = \gamma = 90$ °C. The highest intensity peak (420) has been fitted using Lorentz fitting, and full width at half maxima has been used to calculate Scherrer's crystallite size. The crystallite size calculated are 9.30 nm, 20.13 nm, and 27.66 nm of YIG annealed at 2 hrs, 5 hrs, and 10 hrs, respectively. The method used to deposit the thin film is identical for all three samples except for the annealing duration. With increasing annealing duration XRD peaks get intense and sharpened as a result of an accumulation of crystallites with the increase in annealing duration, as supported by literature ((4)). To get single-phase YIG with good crystallinity, annealing of 5 hrs or more is required, as confirmed by XRD.

4.2.2 Thickness analysis and Surface Morphology

Figure (4.2a) displays the cross-sectional SEM of sol-gel-based deposited YIG. The marked green area is YIG thin film, and the average deposited thickness of the film is 20.18 $\pm$ 2.92 nm. Figure (4.2 b) displays the SEM image of spin-coated YIG. It confirms the polycrystalline deposition that shows the growth is uniform over the substrate. The grains

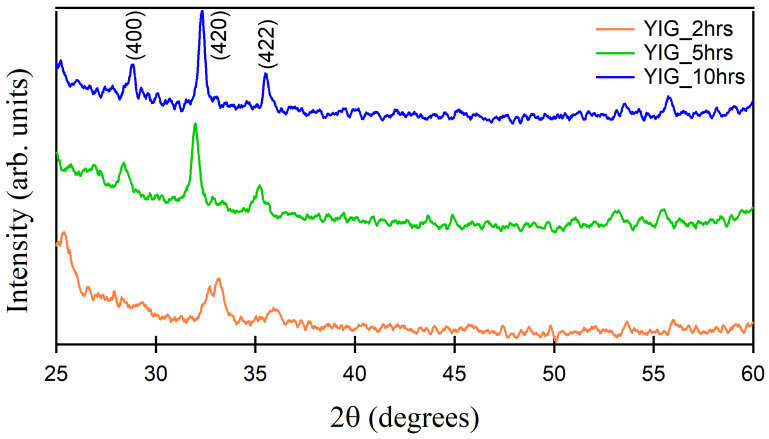

Fig. 4.1 X-ray diffraction of YIG annealed at 2 hrs, 5 hrs and 10 hrs.

have covered the substrate homogeneously. Few larger grains are also observed, but uniform coverage of nm-sized grains on the substrate dominates.

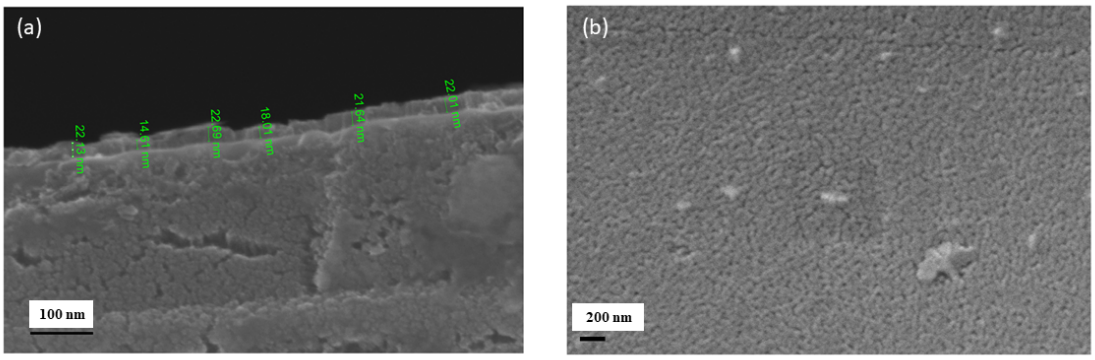

Fig. 4.2 (a)Cross-section scanning electron microscopy image of YIG thin film and (b) surface morphology of homogeneous polycrystalline YIG film.

4.2.3 Elemental Study

Figure (4.3)(a) depicts the wide-range survey scan XPS spectra recorded for synthesized YIG films. Characteristic photoemission and Auger peaks of Y, O, C, N, and Fe (YIG film), confirming the chemical pureness of the grown YIG films. The composition of Y and O are not much varied in the studied samples ((120, 22)). Survey scan of all the three annealed samples are identical, with some intensity variation. Figure (4.3b) depicts

the high-resolution spectra of the O_{1s} orbital. Inset of Figure (4.3) shows the ratio of the surface and the bulk oxygen ratio. The ratio between area of 531.3 eV and 529.6 eV peaks has been presented. The variation between 2hrs and 5 hrs ratio is low 0.4 and is under the error bar of the area estimation of the software. The distinct decrement at 10 hrs is estimating the oxygen vacancy in the sample.

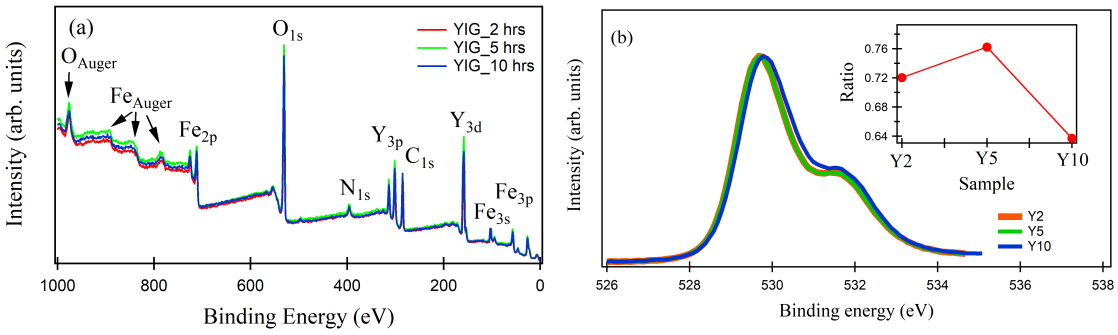

Fig. 4.3 XPS survey scan of the varying annealing duration of sol-gel-based spin-coated YIG thin films with the high resolution O_{1s} spectra of YIG 2 hrs, 5 hrs, and 10 hrs.

The Y (3d), O (1s), and Fe (2p) XPS spectra in higher resolution is shown in Figure (4.4 a-c). Figure (4.4a) presenting the deconvoluted O_{1s} XPS spectra after linear background subtraction. Two peaks at binding energy 529.6 eV and 531.3 eV are due to the presence of O_{1s} in the thin film along with the surface oxygen ((120)). The peak on the high binding energy side is supposed to be related to the hydroxyl group due to YIG surface exposure. As shown in Figure (4.4 b), the prominent peaks for Y (3d) are at binding energy 159.5 and 157.4 eV for $Y_{3d_{5/2}}$ and $Y_{3d_{3/2}}$, respectively that matches with the literature ((98)).

The Fe $2p_{3/2}$ and $2p_{1/2}$ peaks are positioned at 710.3 and 723.9 eV, respectively as shown in Figure (4.4 d). The positions of Fe 2p peaks are used to estimate the presence of $Fe^{2+/3+}$ valence at their ratio. Due to the existing uncertainty of absolute positions of Fe^{2+} and Fe^{3+} peaks, it is feasible to identify Fe^{3+} from $Fe^{2+/3+}$ by the satellite peaks that show up across the higher binding energy side of the $2p_{3/2}$ peak at a distance of $\sim$ 8 eV for pure Fe^{3+} and $\sim$ 6 eV for pure Fe^{2+}. In XPS studies, the Fe^{3+} satellite peak is observed,

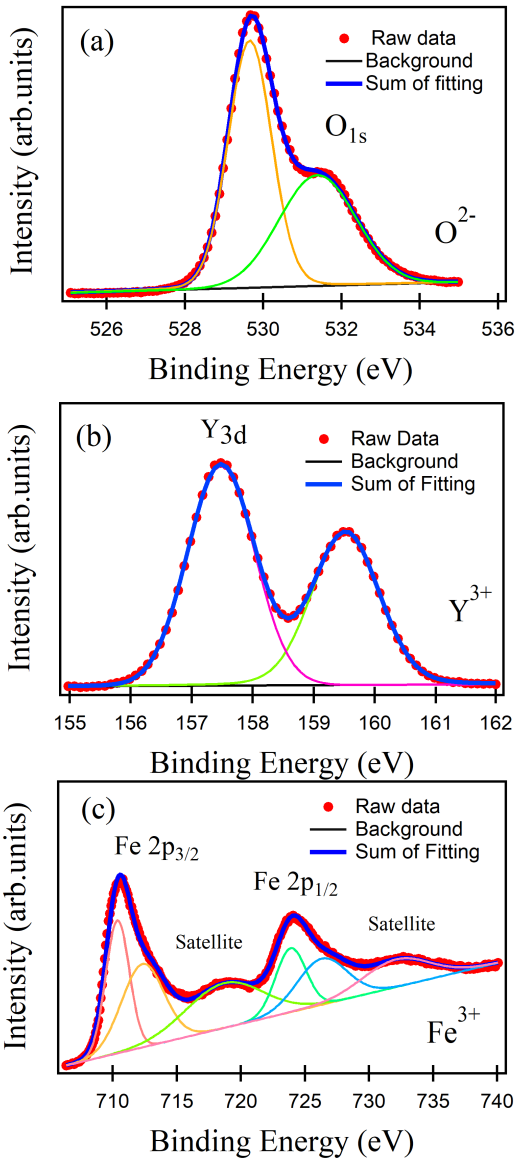

Fig. 4.4 (a) High resolution deconvoluted XPS spectra of (a) O_{1s}, (b) Y_{3d}, and (c) Fe_{2p} energy levels.

indicating the dominating nature of Fe^{3+} valence state. Thus, it is likely that the Fe^{3+} state characteristic for bulk YIG is mostly obtained in thick YIG film, while in the ultra-thin YIG film. As the Fe^{3+} is present in two diffrent environment, i.e., tetrahedral Fe_{tetra} and octahedral Fe_{oct} coordinates. For $Fe_{2p_{3/2}}$, the theoretical intensity ratio of Fe_{oct} and Fe_{tetra} is 2:3 and the experimental calculations gives it to 0.61. For $Fe_{2p_{1/2}}$, the theoretical area ratio is similar and the experimental calculations gives it to 0.65. The average of two

give the ratio be 0.63 wich is equivalent to theoretical ratio 0.66. The error is because of assumption of linear background in analysis. Figure (4.4 d) presenting the deconvoluted Fe_{2p} XPS spectra after linear background reduction. There are mainly eminent peaks at 710.3 eV and 723.9 eV of Fe $2p_{3/2}$ and Fe $2p_{1/2}$ energy levels, respectively ((58, 60)). Table 4.2 shows the experimentally obtained atomic percentage of Y, Fe, and O in the deposited sample. The atomic percentage is calculated using CasaXPS software ((46)). The atomic percentage of Oxygen is 60%, Iron is 22%, and Yttrium is 18%. The experimental atomic percentage is analogous to the expected atomic percentage of the YIG.

Table 4.2 Atomic percentage elements in polycrystalline YIG.

Element	atomic %	Valence state
Oxygen	60	2-
Iron	22	3+
Yttrium	18	3+

4.2.4 Magnetic study

Magnetic measurements gives an overview of the magnetic ordering in the samples. Figure (4.5) depicts the magnetizatoin as a function of magnetic field of YIG 2 hrs (red), YIG 5 hrs (green), and YIG 10 hrs (blue). Saturation magnetization of all three samples are varying. As the FMR suggest the presence of secondary peak in YIG 2 hrs. YIG 5 hrs have highest saturation magnetization makes it most suitable for further studies. As the XPS suggest the oxygen vacancy in the YIG 10 hrs, causes less number of oxygen in sample to favor super-exchange. The decrease in the magnetization is because of the oxygen vacancy.

4.2.5 Ferromagnetic Resonance Study

Figure (4.6) depicts the change in derivative of absorbance as a function of the applied field of YIG 2 hrs, YIG 5 hrs, and YIG 10 hrs in orange, green, and blue color, respectively.

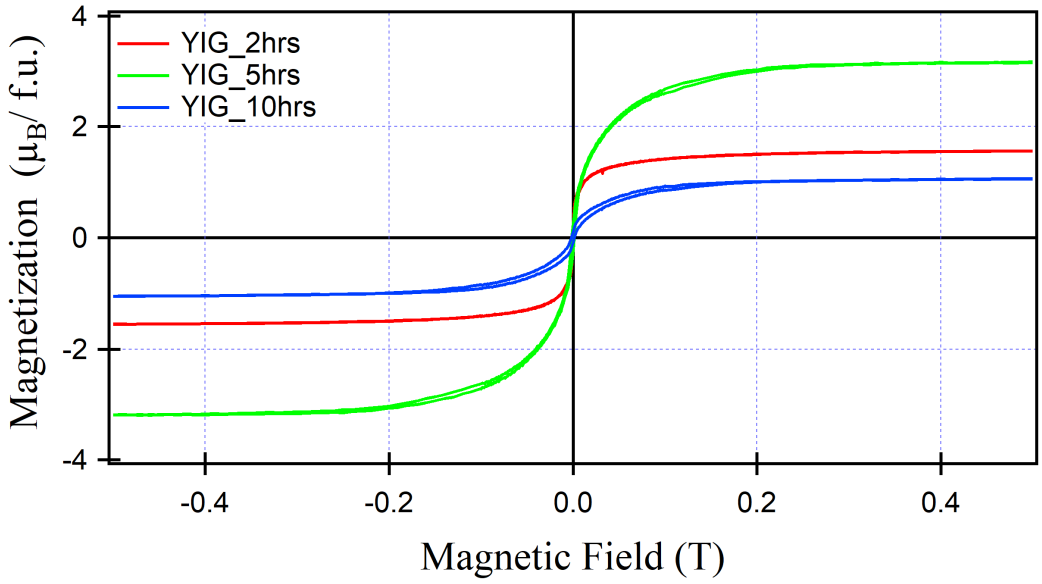

Fig. 4.5 M-H loops of YIG 2 hrs, YIG 5 hrs and YIG 10 hrs.

YIG 2 hrs show direct absorption at 0.2139 T. YIG 5 hrs sample shows as sharp resonance peak at 0.2208 T confirming of single-phase YIG. Suppose deposited thin films have been heated for a longer time, like 10 hrs, it lost its magnetic properties and shows very weak absorbance of 0.2778 T. The optimum annealing duration for YIG synthesis using all sol-gel-based spin coating is 5 hrs at 900 °C. Magnetic dissipation factors like damping constant and inhomogeneous contribution of granular deposited YIG 5 hrs are studied in further discussion.

Figure (4.7 a) shows the FMR spectra in the in-plane geometry of the sol-gel-based spin-coated YIG Film. The first derivative of the absorbance of the microwave of frequency 8 GHz as a function of the applied dc magnetic field is highlighted. Derivative of Lorentzian equation is used to fit the data, shows magnetic resonance field at 0.2214 T and with linewidth (ΔH) of 7.79 mT which is equivalent to previously deposited YIG using PLD on quartz ((13)). This linewidth is slightly higher than the value reported in literature ((100)). The linewidth of the resonance is a result of dissipative elements in the dynamics of the

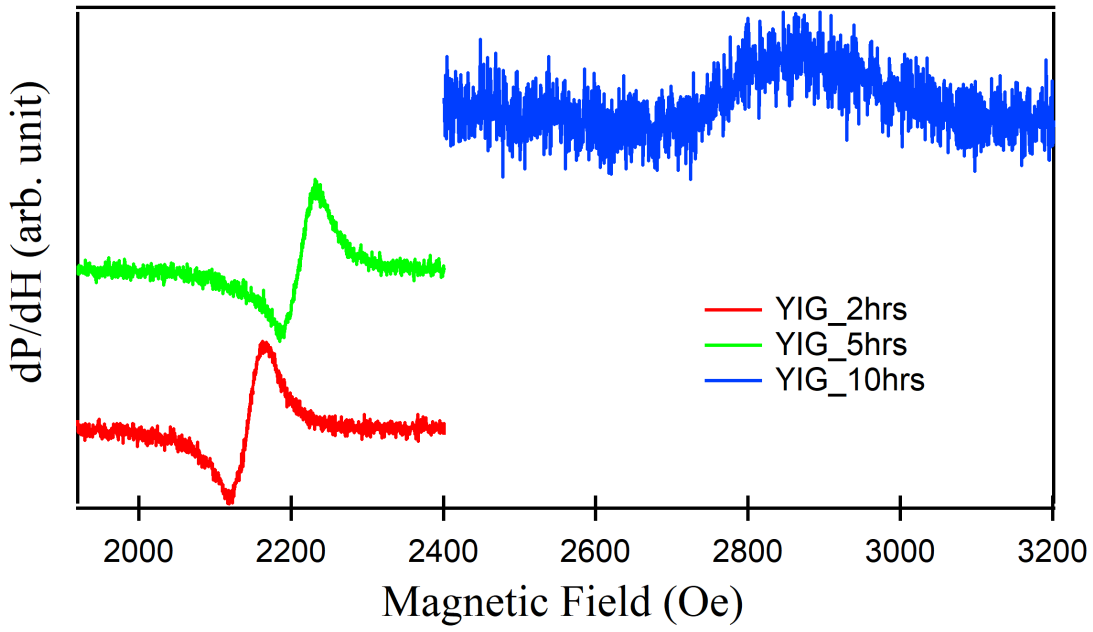

Fig. 4.6 (a) Derivative of phase as a function of applied DC magnetic field of YIG 2 hrs, YIG 5 hrs, and YIG 10 hrs.

materials ((26)). Figure (4.7 b) is frequency as a function of resonance magnetic field (H_{res}). Experimental data are fitted using Kittel equation ((22)) is given as below:

$$f = \left(\frac{\gamma}{2\pi}\right)\sqrt{(\mu_0 M_{eff} + H)(H)} \tag{4.1}$$

where γ is the gyromagnetic ratio, μ_0 is permeability, and M_{eff} is effective magnetization. Fitted data calculates the value of $\mu_0 M_{eff} = 0.1887 \pm 4.5\times10^{-3}$ T and $\gamma/2\pi = 26.64 \pm 0.11$ GHz/T. The value of experimental g-factor is 1.919. As the sample is grown using sol-gel-based spin coating, the grains that constitute the thin film are assembled randomly. Due to the randomization of these grains, there is an absence of anisotropy in the sample. Dissipation of energy in spins is important in knowing the spin-wave damping behavior of the thin film ((31)). The sample's damping constant (α) is analyzed by linear fitting the linewidth as a function of frequency as shown in Figure (4.7 c). As at lower frequencies signal to noise ratio is low, cause over or under-estimation of linewidth occurred. Therefore,

experimental linewidth data has a slight deviation from fitted data. Linewidth as a function of frequency has been fitted using an equation showing the relation of frequency, and the damping parameter is as follows((97, 21)):

$$\Delta H = \Delta H_0 + \left(\frac{4\pi\alpha}{\gamma}\right) f \tag{4.2}$$

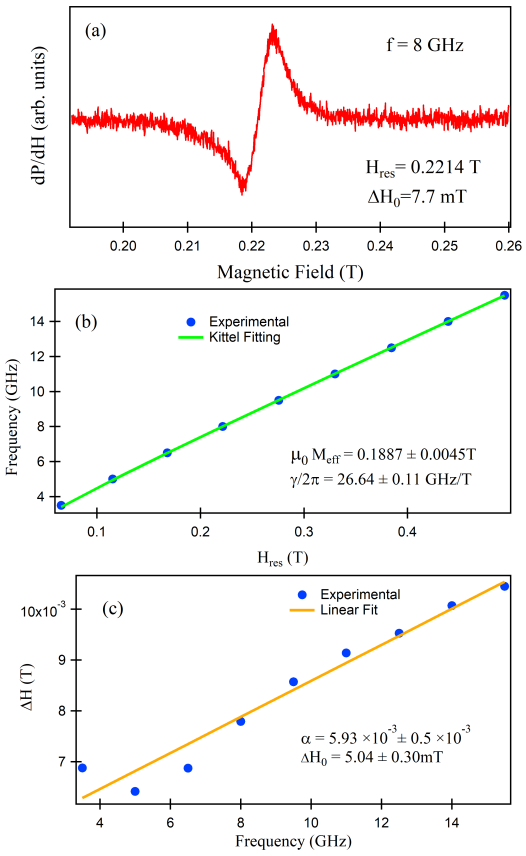

Fig. 4.7 (a) Derivative of phase as a function of applied DC magnetic field showing resonance at magnetic field 0.2214 T with linewidth 7.79×10^{-3} T Oe of the deposited sample. (b) Frequency is plotted as a function of resonance magnetic field and fitted using Kittel formula and (c) experimental linewidth (ΔH) has been plotted as a function of frequency and fitted linearly.

where ΔH is linewidth, ΔH_0 is an extrinsic contribution of the linewidth, α is Gilbert damping constant, a result of intrinsic dissipation and f is applied frequency. Equation (4.2) is utilized to fit the plot of linewidth as a function of applied frequency. This linear fit

gives α = 5.93×10^{-3} ± 0.5×10^{-3} and ΔH_0 = 5.048 ± 0.30 mT. Sol-gel based deposited YIG/Si show a slight higher damping parameter than the PLD and ion beam sputtering deposited films ((24, 83, 117)). Here, the value of ΔH_0 suggests that the major contribution in linewidth is inhomogeneity of film ((10)). Table 4.3 depicts the comparative study of the present study and literature available. It gives how the substrate and method of deposition effects the $\mu_0 M_{eff}$ and Gilbert damping parameter values. Gadolinium Gallium Garnet (GGG) substrate has the lowest damping parameter as the lattice mismatch between YIG and GGG is the lowest. Earlier work in which spin-coating is used shows a high value of the damping parameter. In spin-coating significant contribution to the dissipation of the magnetic energy is the grain boundaries present in the spin-coated YIG. The presence of 5.048 ± 0.30 mT inhomogeneous contribution shows that the individual grains are causing this dissipation in extrinsic mode. This suggests that the polycrystallinity of the sol-gel-based deposited YIG significantly contributes to the magnetic energy dissipation. The intrinsic dissipation of sol-gel-based deposition presented in the present article is better than the PLD deposited YIG on Quartz. Magnetic dissipation in the sol-gel-based spin coating on Si substrate is higher than the PLD, or liquid phase epitaxy deposited YIG on GGG substrates, but when considering the cost-effectiveness, the sol-gel-based spin coating needs to be studied elaborately as done in the present study.

Table 4.3 Comparing literature with the present polycrystalline YIG.

Substrate	Deposition Method	$\mu_o M_{eff}$ (T)	Damping Parameter	reference
SiO_2/Si	Sol-gel-based spin-coating	0.1887	5.93×10^{-3}	Present
Quartz	PLD	0.1620	1.6×10^{-2}	((13))
Si	Co-precipitation spin-coating	0.1734	2.7×10^{-2} to 1.2×10^{-1}	((130))
SiO_2/Si	PLD	0.1633	1.9×10^{-3}	((24))
GGG	Sputtering	0.1770	1.03×10^{-3}	((88))
GGG	PLD	0.1300	3.5×10^{-4}	((119))
GGG	PLD	0.1700	2.3×10^{-4}	((34))

4.3 Summary

Using sol-gel-based spin-coating on thermally oxidized Si(100) substrate, YIG is successfully deposited with varying annealing durations. Formation of YIG in all the three samples is single phase but lattice parameter varied with most relaxed one in YIG 5hrs, make it better for further studies. Survey scan in XPS shows no elemental difference in YIG 2hrs, 5hrs, and YIG 10 hrs. XPS measurement confirms the elements and their chemical state in YIG 5hrs. Ferrimagnetic ordering is confirmed using magnetic hysteresis loop measurement with highest magnetization in YIG 5 hrs. FMR study shows single resonance peak at 8 GHz again confirms single phased YIG and analyzed effective magnetization is 0.1887 $\pm$ 4.5$\times 10^{-3}$ T and $\gamma/2\pi$ is 26.64 $\pm$ 0.11 GHz/T. The lowest spin-coated Gilbert damping constant α measured is 5.93$\times 10^{-3}$ $\pm$ 0.5$\times 10^{-3}$, and inhomogeneous contribution to the linewidth is 5.048 $\pm$ 0.3 mT.

Chapter 5

Magnetic-ordering of epitaxial Yttrium Iron Garnet thin film

Abstract

Sol-gel-based spin coating is a solution method that requires inexpensive resources, and ambient pressure makes it cost-effective. YIG was synthesized in the 1950s and has been extensively used to understand the ferromagnetic resonance and behavior of magnons, as it is the lowest reported Gilbert damping parameter and linewidth. Here, we present sol-gel-based spin-coated epitaxially grown YIG/GGG thin film. The $\approx$ 18 nm thick YIG thin film is epitaxial, and lattice strain is generated due to the lattice mismatch between the GGG substrate and the YIG thin film. The surface roughness of 0.4 nm is excellent for the application purpose. The elemental study utilizes the XPS, confirming that stoichiometry is maintained during deposition. The FMR study and the strain calculation using GIXRD determine the major contribution to the anisotropy because of the stress-induced anisotropy. The stress-induced anisotropy constant (K_σ) is 4.44 kN/m^2 is the major contribution for the uniaxial anisotropy K_U is 4.48 kN/m^2.

5.1 Introduction

Sol-gel-based spin-coating is the all-solution method that requires nitrates and acetates to make a solution. In the case of yttrium, nitrates are low-priced compared to oxides used as precursors for forming targets in PLD and RF-sputtering. Sol-gel-based spin-coating is a cost-effective method that can be utilized to deposit various oxides. As the discovery of YIG has happened, it has shown its potential with magnon propagation, magneto-optic behavior, its application as oscillators, and as a key compound to study the magnon behavior. The propagation length of magnons is a few mm in μ m thick YIG. YIG is an ideal conduit for magnon propagation-based applications. YIG is a unit cell comprised of 160 atoms with the three kinds of coordination, i.e., tetrahedral, octahedral, and dodecahedral sites of Fe^{3+} and Y^{3+} cations. Fe^{3+} cations are present in octahedral and tetrahedral sites. The ratio between the two is 2:3, respectively. Then there is the presence of superexchange in the Fe^{3+}-O^{2-}-Fe^{3+} bonds, and the Goodenough-Kanamuri rule states the presence of the antiferromagnetic coupling between the two half-filled F^{3+} cations. This coupling is between unbalanced Fe^{3+} cations, giving rise to the ferrimagnetic behavior of the YIG. These ferrimagnetic materials have shown their potential in evolving spintronics and magnonics ((80)). YIG, in practice, is deposited using the LPE, PLD, and RF sputtering. Sol-gel-based deposited YIG needs to be addressed in the literature. In a few works of literature, the sol-gel-based spin-coating deposits the polycrystalline YIG/Si.

This chapter presents the YIG/GGG(111) epitaxial growth using the sol-gel-based spin coating. The structural, topography, stoichiometry, and magnetic properties of YIG with the sol-gel-based spin coating are discussed comprehensively. The strain in the thin film is due to the lattice mismatch, which is well established in the literature; a similar behavior is observed with the chosen method. This states that stress-induced magnetic anisotropy is the significant contribution to the magnetic anisotropy in the epitaxial YIG/GGG thin film.

5.2 Results and Discussion

5.2.1 Structural Study

The thin film of YIG is deposited on the single crystal GGG. To confirm the epitaxy and the phase of the YIG/GGG, XRD has been utilized. Initially, lab XRD using CuK_α of the wavelength 1.5406 Åis performed. But the presence of α_1 and α_2 hinder the resolution of the YIG peak. Therefore, the synchrotron GIXRD has been utilized with the wavelength 1.24 Å. Highly monochromatic radiation gives the distinguished peak of the YIG. Figure (5.1) depicts the GIXRD of the YIG thin film. The GIXRD shows the highest intensity substrate peak of GGG (444) reflection, with the broad YIG (444) Bragg reflection. The presence of the Laue oscillation in the GIXRD confirms the high crystallinity with excellent interface roughness. The (444) reflection of the GGG and YIG is observed at 2θ are 40.437° and 40.83°.

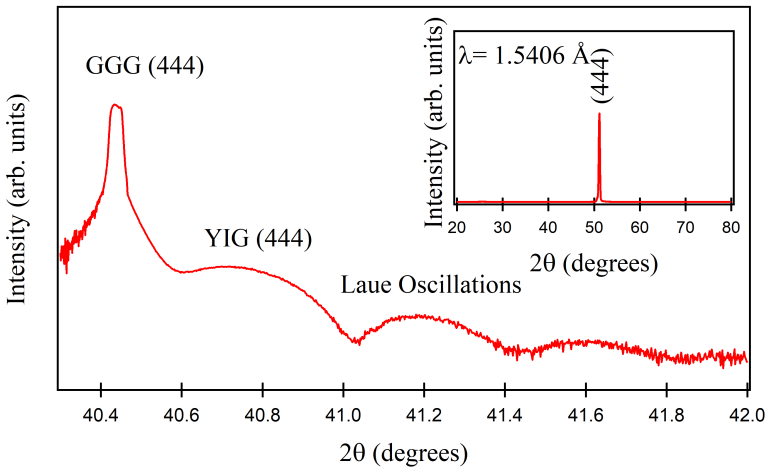

Fig. 5.1 Synchrotron GIXRD of (wavelength 1.24Å) the epitaxial YIG with Laue oscillations for excellent crystallinity. Inset shows the Lab XRD showing (444) reflection of GGG.

The crystal structure of the YIG and GGG is cubic with the space group Ia$\bar{3}$d. The Bragg's equation:

$$2dsin\theta = n\lambda \tag{5.1}$$

where, d is interplanar distance, θ is angle of reflection, and λ is wavelength used. Considering the d value from the above equation and substituting it with the following equation:

$$d = \frac{a}{\sqrt{h^2+k^2+l^2}} \tag{5.2}$$

The lattice parameter estimated with the above equation is a_{GGG} and a_{YIG} are 12.429 $\pm$ 0.011 Å, and 12.352 $\pm$ 0.011 Å, respectively. The lattice mismatch is estimated using the formula as follows:

$$\Delta\varepsilon = \frac{a_{GGG} - a_{YIG}}{a_{GGG}} \tag{5.3}$$

The mismatch between the substrate and thin film $\Delta\varepsilon$ = 0.61%. The positive value of $\Delta\varepsilon$ depicts the tensile strain in the thin film. The stress is estimated utilizing the following equation:

$$\sigma = \frac{Y}{1-\nu}\Delta\varepsilon \tag{5.4}$$

where, the ν is Poission's ratio, and Y is Young's modulus. The value of the ν is 0.29 and Y is 2.00×10^{11} N/m^2 as present in literature ((133)). The estimated value of the σ is $1.743\times10^{9}\pm$ 1.38 N/m^2. The presence of stress in the system causes magnetic anisotropy due to the magneto-elastic contribution as the growth is in (111) direction and considering the magnetostriction constant λ_{111} = -1.7$\times10^{-6}$ from the literature ((14)). Substituting

the stress (σ) and the magnetostriction constant, the stress-induced anisotropy has been calculated using the following equation:

$$K_\sigma = -\frac{3}{2}\lambda_{(111)}\sigma \tag{5.5}$$

The estimation of the K_σ is $4.44 \pm 2.2\times10^{-3}$ kN/m^2.

5.2.2 Thickness and topography Study

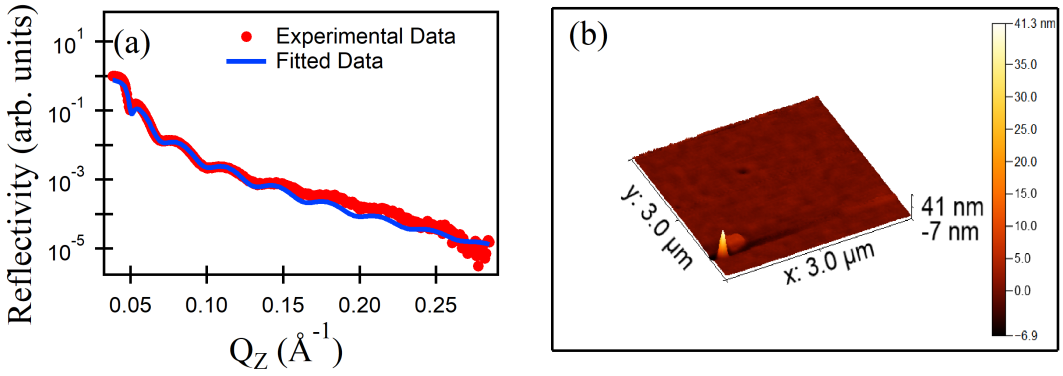

Fig. 5.2 The thickness analysis of the epitaxial YIG utilizing the XRR and the topography study utilizing the AFM.

A non-destructive method to estimate the thickness of the YIG/GGG is XRR. XRR is utilized to estimate the YIG/GGG's thickness, surface, and interfacial roughness of the YIG/GGG. Figure (5.2) (b) presents the experimental and fitted XRR data of the YIG with the (b) AFM image of the epitaxial YIG. The experimental XRR data is fitted using Parratt's formulism utilizing the Parratt32 software ((99, 47)). The thickness estimated is $\approx$ 18 nm. The surface roughness is $\approx$ 0.4 nm, and the interfacial roughness is $\approx$ 0.7 nm. The roughness is favorable for the application. The laue oscillation in the GIXRD also confirms the excellent crystalline quality of the deposited YIG sample. The topography of the YIG is depicted utilizing AFM. The estimated surface average roughness is $\approx$ 0.56 nm,

which is of the same order as the XRR. The AFM suggests the homogeneous growth of the YIG on GGG(111).

5.2.3 Elemental Study

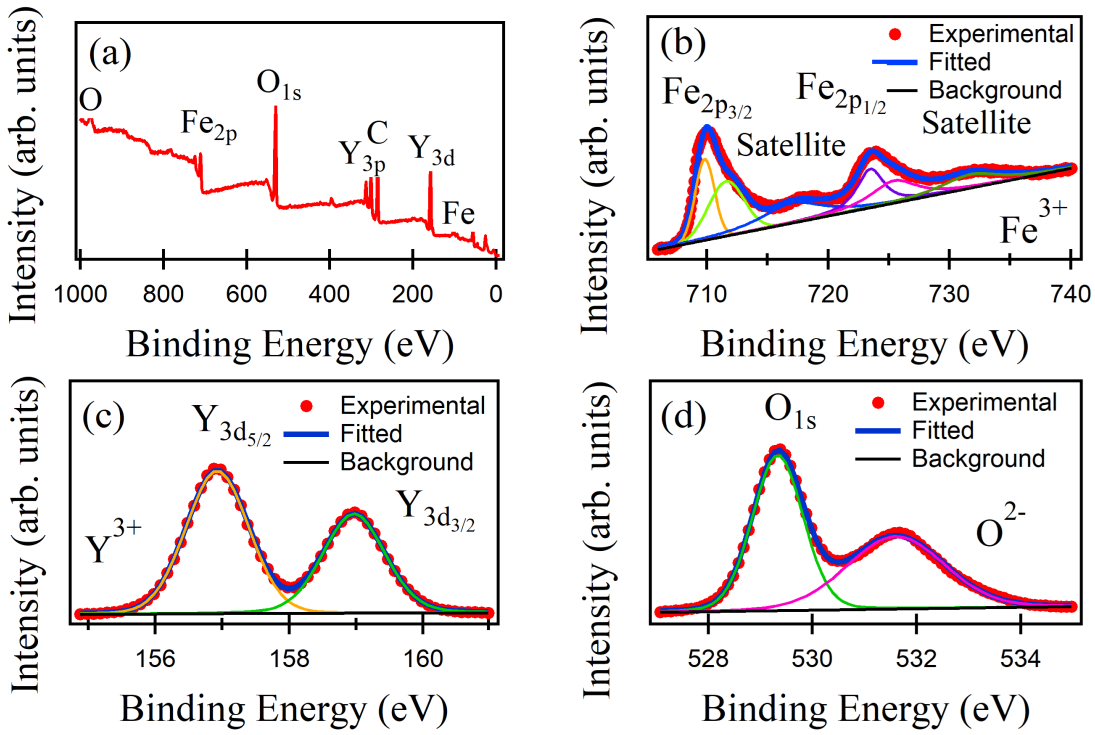

Fig. 5.3 Synchrotron GIXRD of (wavelength 1.24Å) the epitaxial YIG with Laue oscillations for excellent crystallinity. Inset shows the Lab XRD showing (444) reflection of GGG.

The confirmation of the stoichiometry is performed utilizing the XPS. Figure (5.3)(a) depicts the survey scan of the thin film. Oxygen, iron, Yttrium, and carbon in the survey scan have been notified. Calibration is performed considering C_{1s} at binding energy 284.8 $\pm$ 0.1 eV. Figure (5.3)(b) depicts the high-resolution spectra of the Fe_{2p}. The deconvoluted high-resolution spectra show the presence of two peaks in each $Fe_{2p_{3/2}}$ and $Fe_{2p_{1/2}}$. The two constituents are because of the two Fe cation environments. Fe cations are present in tetrahedral and octahedral coordinates. The four oxygen anions surround the Tetrahedral,

and six oxygen anions surround the octahedral. Due to this difference in environment, these distinct peaks occur. As the crystal structural study confirms the presence of two octahedral Fe_{octa} and three tetrahedral Fe_{tetra}, the ratio between the two is 2:3. The peak of $Fe_{2p_{3/2}}$ is at 709.8 $\pm$ 0.1 eV and 711.6 $\pm$ 0.1 eV for the tetrahedral and octahedral coordination, respectively. The peak of $Fe_{2p_{1/2}}$ is at 723.5 $\pm$ 0.1 eV and 725.4 $\pm$ 0.1 eV for the tetrahedral and octahedral coordination, respectively. The presence of a satellite peak at a difference of $\approx$8 eV from the tetrahedra peak confirms that the cationic state of iron is 3+. To confirm the crystallographic ratio between octahedral and tetrahedral Fe, experimentally, the intensity of the Fe_{octa}: Fe_{tetra} are calculated. The experimental ration for the $Fe_{2p_{3/2}}$ is 0.66 and $Fe_{2p_{1/2}}$ is 0.56. $Fe_{2p_{1/2}}$ is slightly deviated because of the assumption of linear background. Figure (5.3)(b) depicts the high-resolution spectra of the Y_{3d}. The peak positions of $Y_{3d_{5/2}}$ and $Y_{3d_{1/2}}$ at binding energy 156.9 $\pm$ 0.1 eV and 158.9 $\pm$ 0.1 eV. These support the literature and present Y^{3+} cationic state ((112)). Figure 5.3 (d) depicts the Oxygen anion's high-resolution spectra. The thin film contribution is at binding energy 529.3 $\pm$ 0.1 eV, and the surface hydroxyl oxygen is at binding energy 531.6 $\pm$ 0.1 eV. The atomic percentages of Oxygen, iron, and yttrium are estimated using CASAXPS software, and the estimation is 55.73%, 24.98%, and 19.3%, respectively ((46)). The experimental atomic percentage is close to the stoichiometry estimation.

5.2.4 Magnetic Study

The epitaxial YIG thin film is studied using the FMR. The field dependent data have been taken at 2 GHz to 15 GHz frequency range. Figure (5.4 (a)) depicts a single spectra at the 10.5 GHz frequency as a varying magnetic field. The resonance magnetic field (H_{res}) is 0.3423 T and the linewidth observed is 7.78 mT. The frequency as a function of the H_{res}

is plotted and fitted using the Kittel equation. the magnetic field is applied in in-plane geometry. The Kittel equation for the inplane magnetic field on thin film is as follows:

$$f = \left(\frac{\gamma}{2\pi}\right)\sqrt{H(H+\mu_0 M_{eff})} \tag{5.6}$$

where, f is applied frequency, γ is a gyromagnetic ratio, and $\mu_0 M_{eff}$ is effective magnetization. Figure (5.4 (b)) depicts the experimental and Kittel fitted frequency as a function of resonance field. The value of the gyromagnetic ratio is present is 28.49 $\pm$ 0.05 GHz/T, and the Land g-factor estimated as 2.036 $\pm$ 0.004. The fitted curve gives the estimated $\mu_0 M_{eff}$ = 0.05301 $\pm$ 0.0016 T. estimated $\mu_0 M_{eff}$ less than the saturation magnetization (M_S) predicts the presence of the anisotropy in the YIG/GGG thin film. The relation between the $\mu_0 M_{eff}$, M_S and anisotropy field is as follows:

$$\mu_0 M_{eff} = \mu_0 M_S - H_U \tag{5.7}$$

M_S is assumed from the literature and its value is 0.1382 T. The result of two substitutions gives the H_K = 0.0852 T. This H_K and M_S is used to estimate the anisotropy constant (K_U) calculation as per the below equation:

$$K_U = \frac{H_U \times M_S}{2} \tag{5.8}$$

The K_U is estimated from the above formula is 4.69 kN/m^2. Uniaxial anisotropy can be measured by combining cubic anisotropy, shape anisotropy, and stress-induced magnetic anisotropy. The value of the cubic anisotropy in the YIG is -0.57 kN/m^2 and shape anisotropy is 0.605 kN/m^2 with stress-induced anisotropy is calculated with the equation 5.5. The uniaxial anisotropy is estimated as 4.48 kN/m^2 by substituting all in the equation. The difference between the two is 0.21 kN/m^2, which is because of the approximate value of the M_S from the literature. As the literature presents, the significant

contribution of anisotropy is because of the stress-induced anisotropy and very little due to the cubic or shape anisotropy.

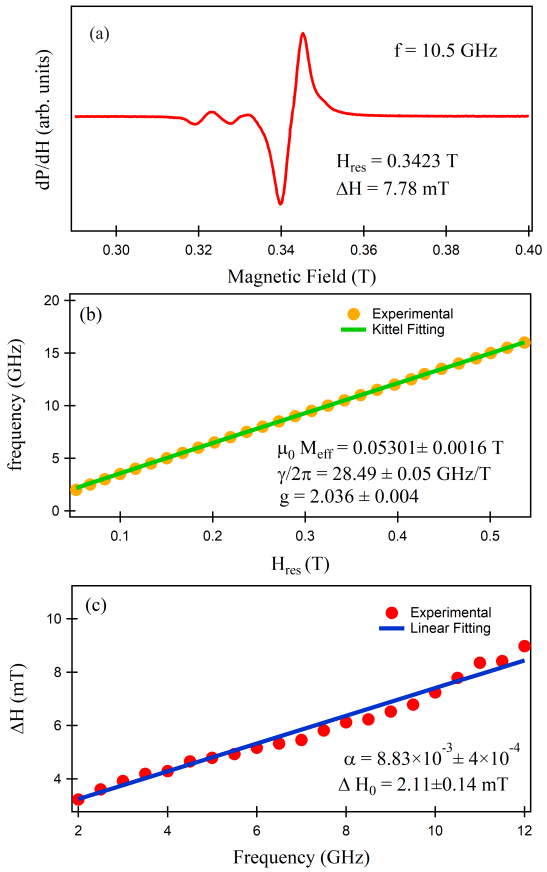

Fig. 5.4 FMR study of the epitaxial YIG. (a) FMR spectra of the epitaxial YIG, (b) Kittel fitting study of the frequency as a function of resonance field, and (c) linear fitting to estimate the Gilbert damping parameter.

Figure (5.4 (c)) depicts the damping parameter estimation using the linear fit to the linewidth (ΔH) as a function of frequency. the estimated Gilbert damping parameter (α) = 8.83 $\times$ $10^{-3}\pm$ 4$\times$ 10^{-4}. Which is higher than the polycrystalline YIG. The non-homogeneous contribution (ΔH_0) to the damping in the epitaxial YIG is 2.11 $\pm$ 0.14 mT. The intrinsic contribution is higher because of the GGG and YIG interface interaction as the epitaxy reduces the defects and the dissipation energy's non-homogeneous contribution.

5.3 Summary

The Sol-gel-based spin-coating has the potential to deposit an epitaxial thin film of the ≈18 nm YIG on the GGG(111) single crystal. The surface roughness of ≈ 0.4 nm shows its excellent quality. High crystallinity is confirmed with the GIXRD. The epitaxial YIG has stoichiometry deposition, as demonstrated by the XPS. The magnetic study is performed with FMR, and it gives the presence of anisotropy in the epitaxial YIG. This work estimates the net sum of the stress-induced anisotropy, shape anisotropy, and cubic anisotropy to get the uniaxial anisotropy. The significant contribution to the uniaxial anisotropy is the stress-induced anisotropy in sol-gel-based spin-coating, as presented in the literature.

Chapter 6

Magnetic-ordering of polycrystalline Thulium Iron Garnet thin film

abstract

In the quest to utilize rare-earth garnets (ReIG) with perpendicular magnetic anisotropy (PMA) in futuristic spintronics, the attention turned towards iron garnet thin films. Among this family, the one candidate is $Tm_3Fe_5O_{12}$ (TmIG) that manifests PMA with excellent Gilbert damping, making this material a potential candidate in magnonics devices. This chapter presents a cost-effective deposition approach of the TmIG thin films deposited on a thermally oxidized Si(100) substrate. The homogeneous TmIG ($\approx$22 nm thick) thin film shows a roughness of $\approx$1.5 nm. The magnetic properties of thin films indicating the compensation temperature $\approx$15 K. Experimental findings present a method for the deposition of TmIG thin films, which is a potential candidate for fabricating futuristic compact device. The structure is confirmed with the XRD. Thickness evolution with the XRR and elemental stoichiometry is confirmed using XPS. Magnetic ordering is observed using SQUID-VSM.

6.1 Introduction

The presence of significant PMA is crucial for stability and higher compactness, along with the low Gilbert damping parameter, which has been demonstrated in rare-earth iron garnet (ReIG) and bismuth substituted YIG ((131, 85, 105, 9, 8)). The presence of PMA in FMI opens the application of ReIG in racetrack memory and logic gates ((103)). Lower damping, extended magnon decay length, PMA, spin-orbit coupling, and strong spin-mixing conductance in TmIG/Pt hetero-structure expresses its potential application in spintronics ((5, 110)). The synthesis of solution-based rare-earth iron garnet is possible. The rare-earth have low temperature ferromagnetic ordering which effect the net magnetization. As the temperature decreases its moment starts to align oppoiste to the Fe^{3+} magnetic moment and give rise to compensation temperature. This temperature at which the minimum magnetic moment is observed is known as the compensating temeprature of the rare-earth garnets. In literature, low compensation temperature of the TmIG has been predicted. In this chapter experimental evidence of the low temperature compensation has been presented using DC magnetometry. In previous investigations, TmIG thin films have been grown using RF-sputtering and pulsed laser deposition (PLD) ((131, 85, 105, 9, 8, 52)). This chapter presents an all-aqueous solution-based sol-gel-based spin-coating method to deposit excellent quality TmIG thin films on a thermally oxidized Si (100) substrate. Sol-gel-based spin-coating is a cost-effective way to deposit the oxides ((112, 100)). The polycrystalline thin film on thermally oxidized Si(100) has been synthesized. The structural and magnetic properties of the deposited film have been studied using XRD, XRR, AFM, and SQUID-VSM. Low-thickness TmIG sample with moderate roughness has been characterized to confirm its stoichiometry using the XPS. The magnetic properties are discussed using SQUID-VSM. The characterizations confirms the single phase, stable ferrimagnetic insulator with low compensation temperature useful for the magnonic applications as it give full range magnetization with high Curie temperature.

6.2 Results and Discussion

6.2.1 Structural Study

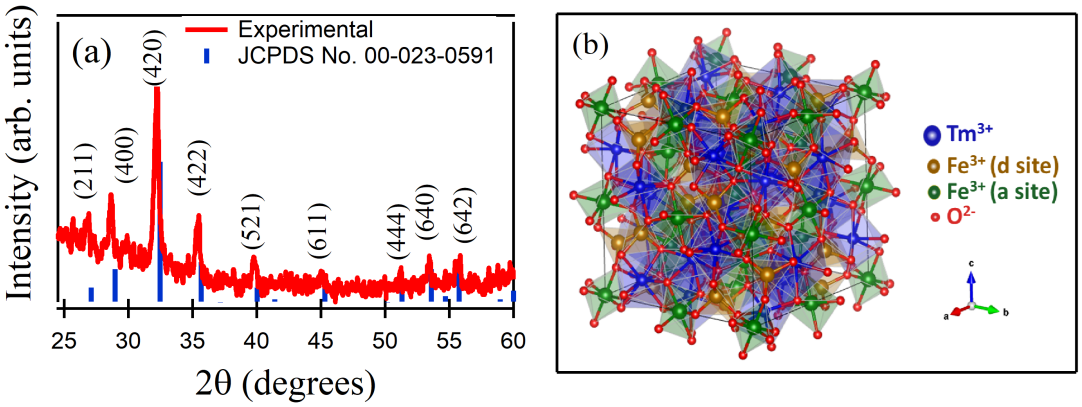

Fig. 6.1 (a) X-ray diffraction graph of TmIG, (b) unit cell of TmIG.

XRD is a powerful tool to confirm the crystalline state of compounds. Figure 6.1 (a) depicts the diffraction pattern of the TmIG thin film deposited on thermally oxidized Si using the sol-gel process. The structural phase is confirmed using JCPDS file No. 00-023-0591 ((126, 86)). The Braggs reflections of all the planes (211), (400), (420), (422), (521), (611), (444), (640), and (642) are distinguishable in the XRD pattern. The XRD confirms the space group $Ia\bar{3}d$, which is a cubic crystal structure. Analysis of XRD pattern considering (400), (420), (422), and (521) bragg reflections provides lattice parameters a = b = c = 12.4277 $\pm$ 0.0221 Å. As the crystal structure is cubic, angles are $\alpha = \beta = \gamma$ = 90°. XRD supports the polycrystalline phase of the deposited thin film. Using the Scherrer equation crystallite size has been estimated considering the highest intensity peak of Braggs plane (420). The crystallite size estimated is $\approx$16 nm. The nano particle are arranges on the substrate homogeneously. Figure: 6.1 (b) depicts the crystal structure of the TmIG produced using VESTA software. The dodecahedral blue Tm^{3+} cations with

the tetrahedral Golden Fe^{3+} cations and green octahedral Fe^{3+} cations with the red O^{2-} anions. There are eight formula units make a unit cell with 160 atoms per unit cell.

6.2.2 Topography Study

The non destructive method to analyze the thickness and roughness is the XRR. XRR is used to analyze the thickness and the roughness quality of the TmIG thin film. Figure 6.2(a) depicts the fitted XRR experimental data with Parratt's formalism ((99, 47)). The thickness estimated using XRR is ≈ 22 nm with a surface roughness of ≈1.39 nm. The interfacial roughness between SiO_2 and TmIG is 0.3 nm. Figure: 6.2(b) shows the 3-dimensional surface morphology of the TmIG thin film. It concludes the homogeneous surface with a mean roughness of ≈1.2 nm, which is the same range as estimated by XRR. The surface is of good quality with moderate roughness.

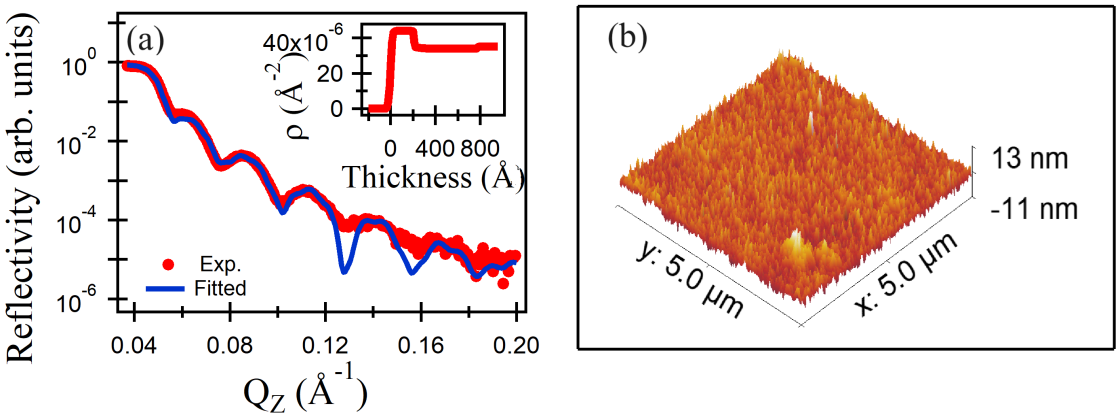

Fig. 6.2 (a) XRR graph of the TmIG with inset showing depth profiling, and (b) AFM micrograph of thin films.

6.2.3 Elemental Study

XPS is a nondestructive technique to probe the stoichiometry of the deposited thin film. Figure 6.3 (a) shows a survey XPS scan of the deposited thin film. It verifies the presence of thulium, iron, and oxygen along with carbon and nitrogen. XPS is calibrated with

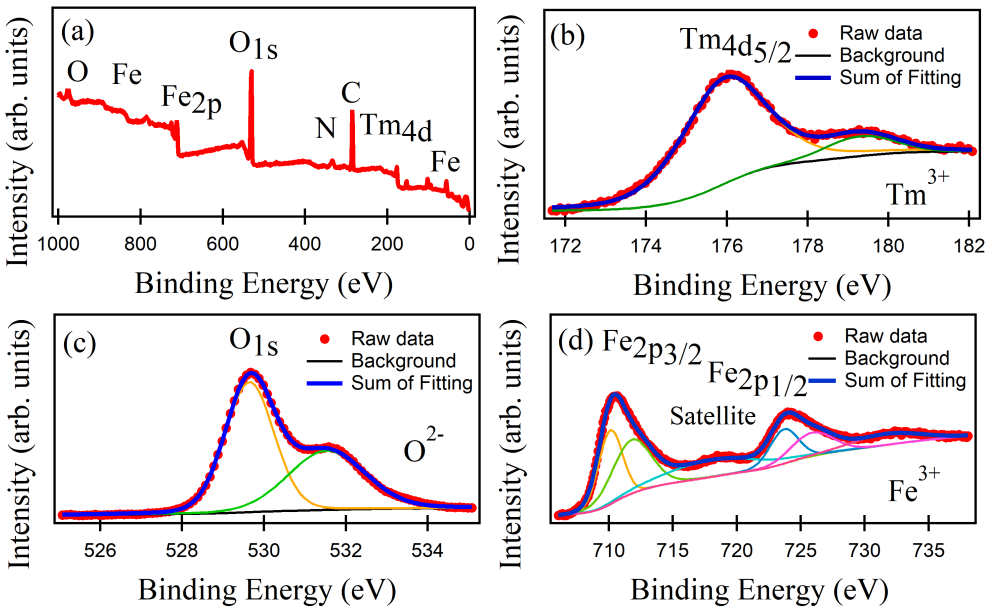

Fig. 6.3 (a) XPS survey scan of the TmIG confirming the presence of anticipated elements. High-resolution XPS spectra of (b) Tm_{4d}, (c) O_{1s}, and (d) Fe_{2p} elements.

carbon peak at 284.5 $\pm 0.1 eV$. Figure 6.3 (b) depicts high-resolution spectra of the $Tm_{4d_{5/2}}$. The peak of Tm^{3+} ion in the spectrum is at binding energy 175.9 $\pm$0.1 eV, which is very close to 175.4 $\pm$0.1 eV present in XPS database ((23)). The presence of satellite peak depicts the 3+ cationic state of the Thulium ((93)). Figure 6.3 (c) is high-resolution spectra of the O_{1s} with a peak at 529.6 $\pm$0.1 eV coexisted with the sister peak at 531.5 $\pm$0.1 eV. O_{1s} is the bulk contribution of the TmIG and the sister peak is result of the surface oxygen and hydroxyl environment at the top. Figure 6.3 (d) is a high-resolution spectrum of the Fe_{2p} orbital. There two different kind of Fe environments. First is tetrahedral (Fe_{tetra}) and second is octahedral (Fe_{octa}). The deconvolution of the Fe_{2p} gives the these contributions distinctively. The ratio of the intensity of $I_{Fe_{octa}}$ and $I_{Fe_{tetra}}$ of $Fe_{2p_{3/2}}$ spectra is 0.71 and $Fe_{2p_{3/2}}$ spectra is 0.61, the average of both gives 0.66 which is equivalent to the theoretical value 2:3. The presence of satellite peak at $\approx$8 eV from the tetrahedral environment confirms the presence of Fe^{3+} ion, as present in literature ((58, 112)). The atomic percentage analysis using the XPS has been performed using CasaXPS software

((46)). The thulium, iron, and oxygen are present in 12%, 26%, and 62%, respectively are very close to the desired TmIG stoichiometry. The atomic percentage analysis confirms the purity of composition and the absence of any secondary phase in the deposited thin film.

6.2.4 Magnetic Study

The magnetic study of the TmIG is essential to know its magnetic ordering. The literature suggests a low temperature compensation in TmIG bulk ((81)). Present work used SQUID-VSM to study room temperature and low temperature magnetization behavior of TmIG. Figure 6.4 (a) depicts the magnetization as a function of the temperature M(T) curve in the presence of a 100 Oe magnetic field of TmIG thin film. M(T) curve follows the trend of the bulk TmIG as reported in literature ((81, 56)). With the decrease in temperature, magnetization increases till 173 K and then decreases as temperature reduces further to 15 K, where it shows the minimum and starts to increase further. The complex canted magnetic state of the TmIG has been predicted using the M(T) curve. The reduction in the magnetization at 173 K is due to antiferromagnetic coupling and the complex canting behavior of the tetrahedral and octahedral Fe cations. Magnetization supports the bulk-like magnetic ordering of the TmIG on the thermally oxidized Si (100) synthesized using the complete solution method. The presence of antiferromagnetic transition near 50 K is due to the oxygen leakage in the chamber of the MPMS ((107)). Figure 6.4 (b) shows the schematic of the competition of the moment of iron and thulium present in the system which is inspired by the compensation mechanism explained by Wang *et al.* ((126)). The structure of TmIG gives information that there are two species of the Fe^{3+} ions one is octahedral (a-site), and another is tetrahedral (d-site). These two Fe^{3+} cations have ferrimagnetic coupling as supported by the Figure (6.4 a). In dodecahedral rare-earth Tm^{3+} ion, moment starts to originate with paramagnetic to antiferromagnetic ordering below 56 K and modulated ferromagnetic below 32 K ((73)). The competition

between the dodecahedral Tm^{3+} and tetrahedral and octahedral Fe^{3+} is a result of the canted magnetic moment of different sites as depicted in Figure (6.4 b). The literature proposed that the temperature dependence of the magnetization of thulium metal shows highest magnetic moment across ≈15 K ((36)). These competing moments at which they are opposite to each other and moment of Tm^{3+} at maxima give rise to the minima in the M(T) plot (the compensation temperature at ≈ 15K) and further increase at the moment due to the enhancement of the moment of Fe and decrement in the moment of Tm at lower temperature. This low-temperature compensation goes hand in hand with literature ((56)).

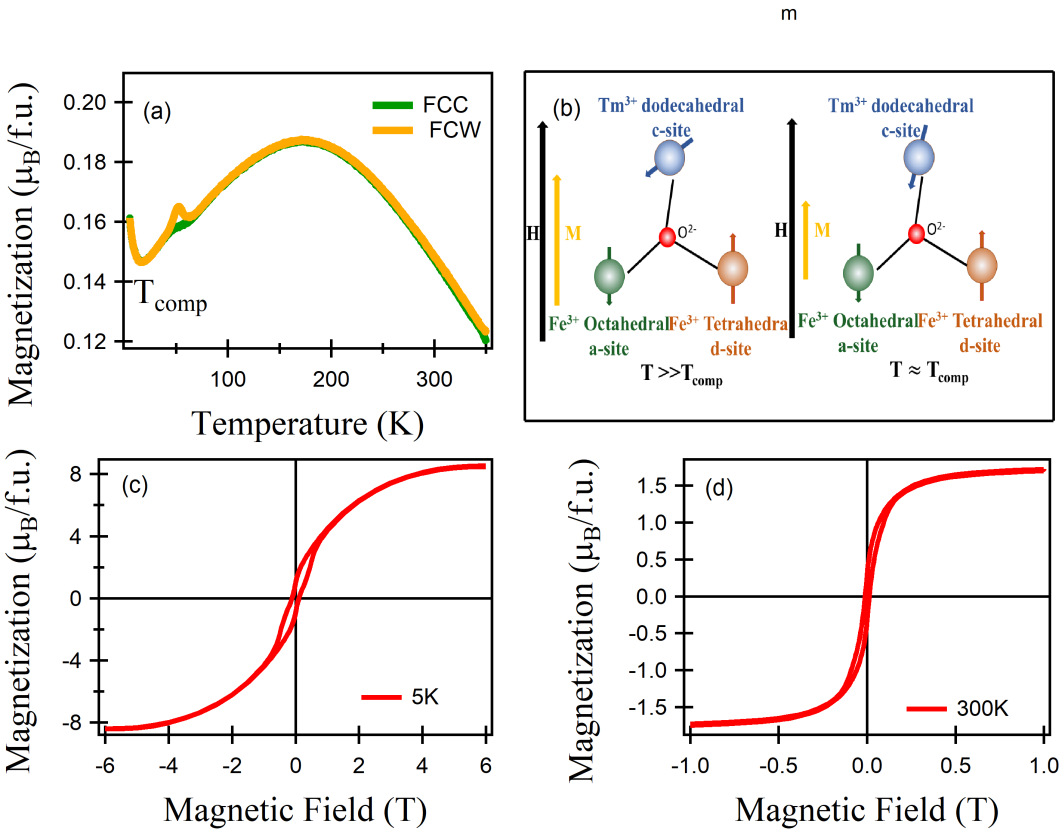

Fig. 6.4 (a) Magnetization as the function of the temperature of the TmIG, (b) Schematic of the moments a-site, d-site, and c-site above the Compensation temperature and at the compensation temperature, and (c) and (d) are magnetic hysteresis of the TmIG at 5 K and 300 K, respectively.

Figure 6.4 is magnetic hysteresis of TmIG thin film (c) at 5K $< T_{comp}$, and (d) at 300K $\gg T_{comp}$. The magnetic hysteresis at 5 K gives the signature of the two competing ferro-

magnetic ordering. The kink in the magnetic hysteresis is because of the two competing magnetic lattices of Tm^{3+} and the Fe^{3+}. Two different hysteresis overlap and gives net magnetization as a function of an external field, which is result of this kink. The moment is ≈8 μ_B/f.u. at 5 K. Figure 6.4(d) depicts the room temperature magnetic hysteresis. The saturation magnetization calculated by averaging the positive and negative value of the saturation of the TmIG hysteresis at 300 K is 1.7 μ_B/f.u. gives the room-temperature ferrimagnetic coupling ((127)). A magnetic coercivity of 126 Oe is observed. The magnetic order of the TmIG thin film on thermally oxidized Si (100) is canted ferrimagnetic, similar to the bulk. Solution-based spin coating is a cost-effective method to deposit the rare-earth garnets showing similar magnetic ordering as its bulk. Both low temperature and room temperature behavior are present.

6.3 Summary

TmIG thin film of ≈22 nm thickness has been successfully deposited using a sol-gel-based spin coating. The nature of the thin film is polycrystalline. Homogeneity of the thin film with roughness ≈1.5 nm. XPS confirms the stoichiometry is maintained and the presence of Tm^{3+}, Fe^{3+}, and O^{2-} ions in the sample. Magnetic measurement supports the complex magnetic nature of the ferrimagnetic coupling with ≈ 15 K as compensation temperature of the deposited sample. The hysteresis curve shows the low-temperature modulated ferromagnetism with the room-temperature ferrimagnetic ordering.

Chapter 7

Magnetic-ordering of the epitaxial Thulium Iron Garnet thin film

abstract

Magnonics has shown the immense potential of compatibility with CMOS devices and the ability to be utilized in futuristic quantum computing. Therefore, the magnonic crystals, both metallic and insulating, are under extensive exploration. The presence of high spin-orbit interaction induced by the presence of rare-earth elements in thulium iron garnet (TmIG) increases its potential in magnonic applications. Here, we present a cost-effective solution-based approach that enables the excellent quality interface and surface roughness of the epitaxial TmIG/GGG. The deposited TmIG ($\approx$12.2 nm) thin film's physical and spin dynamic properties are investigated in detail. The confirmation of the epitaxy using X-ray diffraction in ϕ-scan geometry along with the X-ray reflectivity and atomic force for the thickness and roughness analysis and topography, respectively. The epitaxial TmIG/GGG have confirmed the perpendicular magnetic anisotropy utilizing the polar-magneto-optic Kerr effect. Analyzing the ferromagnetic resonance study of TmIG/GGG thin films provides the anisotropy constant K_U = $20.6\times10^3 \pm 0.2\times10^3$ N/m^2 and the

Gilbert damping parameter $\alpha = 0.0216 \pm 0.0028$. The experimental findings suggest that the solution-processed TmIG/GGG thin films have the potential to be utilized in device applications.

7.1 Introduction

Magnonics is the study of spin waves-based information processing and transmission ((49)). Magnons have the potential to be utilized in more dense logic gates, along with the processing and transport of information simultaneously ((28)). Magnon's superposition ability makes it a potential candidate for its uses as a qubit in quantum computing ((3)). There are various magnon carrier systems; some are conducting, and others insulating ((28)). Conducting magnonic crystals are CoFeB((89, 129)), NiFe(permalloy) ((95, 76)), and Heusler compounds ((101, 109)). Iron garnets are one class of these insulating magnonic crystals ((110)). Initially, various fundamental understandings of magnon behaviours like magnon-magnon scattering and magnetic resonance have been considered as possible microscopic origins using these ferrimagnetic insulators ((115, 116)). Recently, the heterostructure YIG found its application in spin pumping. Soon after its discovery in 1950s, the experimental study confirmed system has the lowest dissipation (lowest linewidth of the ferromagnetic resonance), making it a promising system for various applications((25)). A recent study shows that in pulsed laser deposition (PLD) grown Pt/YIG, the interfacial spin Hall angle (θ_{SH}) is 0.33 ((33)). But further advanced processing can be achieved by PMA in the system ((53)). YIG has a low anisotropy constant K_U = 1×10^3 N/m^2 when deposited on $Gd_3Ga_5O_{12}$ (GGG) substrate((82)). High spin-orbit coupling in rare-earth iron garnets has the potential to resolve this ((92)). Complete rare-earth series can form the iron garnets ((133)). The rare-earth elements have their unique magnetic ordering so they contribute to the ferrimagnetic coupling. This contribution causes compensation temperature, which is the lowest magnetization state. Thulium iron

garnet (TmIG) is the rare-earth garnet with Curie temperature ($T_C \approx 550$ K) that has the lowest compensation temperature ≈15 K and room temperature moderate saturation magnetization. Recently, the Pt/TmIG heterostructure with PMA shows the magnetic switching and spin magnetoresistance ((6)) and TmIG/Au/TmIG shows the spin valves properties ((124)).

Iron garnet thin films are grown using ultra-high vacuum facilities and require extravagant facilities like PLD, off-centred rf-sputtering, and liquid phase epitaxy (LPE). Few studies have produced polycrystalline iron garnets using solution methods like spin-coating ((112, 111, 100)). However, the epitaxial thin film growth using spin-coating is not reported to date. This article presents a cost-effective, all-solution-based spin-coating method that uses the substrate's crystal structure to reference and grows an epitaxial thin film of TmIG/GGG. The epitaxial TmIG/GGG has been studied using synchrotron Grazing Incident X-ray diffraction (GIXRD). The confirmation of the epitaxy is presented using GIXRD ϕ-scan. The topography and elemental analysis of TmIG magnonic crystal are studied in detail. The magnetic study of the good interface quality epitaxial TmIG thin film is reported in the present article.

7.2 Results and discussion

7.2.1 Structural Study

The phase formation of the TmIG thin film deposited using sol-gel-based spin coating is performed using the GIXRD. As the mismatch between the substrate and the thin film is less than a percent, therefore, highly monochromatic 10 keV synchrotron X-rays have been utilized. Figure 7.1 (a) presents the out-of-plane XRD of TmIG (444) reflection with the substrate GGG (444) highest intensity reflection. Inset Figure 7.1(a) shows the logarithmic plot of the intensity to show the excellent interface quality that confirms high crystallinity

due to the presence of Laue oscillations ((42)). The interplanar distance of GGG (444) and TmIG (444) are 1.7938 ± 0.0085 Å, and 1.7778 ± 0.0084 Å, respectively. The lattice constants are 12.4281 ± 0.0116 Å, and 12.3145 ± 0.0116 Å, for the GGG and TmIG, respectively. Experimental data confirm the smoothness of the interface and the epitaxial growth between the substrate and thin film as shown in Figure 7.1 (b). The strain because of the mismatch between the two $\Delta\varepsilon = \frac{a_{GGG}-a_{TmIG}}{a_{GGG}}$ is 0.91 % which shows the tensile strain on the layer of TmIG thin film. The tensile strain is the cause of the presence of the PMA in the sample (discussed in further sections). Figure 7.1 (b) represents the ϕ-scan of the TmIG thin film. The ϕ-scan is measured along the (008) Bragg reflection, which is ψ = 54.7° from the (111) Bragg reflection ((90)). The three-fold symmetry in the ϕ-scan can be observed in Figure 7.1 (c). The angle difference of 120^0 between three-fold symmetry is experimentally observed in ϕ-scan, which confirms the epitaxy of the deposited thin film ((65)). The stress (σ) at the interface is calculated using the following equation ((51)):

$$\sigma = \frac{Y}{1-\nu}\Delta\varepsilon \tag{7.1}$$

where, Y is Young's modulus (2.00×10^{11}N/m^2) and the ν is Poisson's ratio (0.29) as present in literature ((133)). The σ calculated is $2.573\times10^9 \pm 2$ N/m^2.

7.2.2 Thickness and Topography Study

The substrate film interface quality is essential for the magnonic application. Figure 7.2 illustrates the topography and structural quality of the deposited thin film using AFM and XRR. Figure 7.2 (a) illustrates AFM showing smooth topography, estimating mean roughness is ≈0.8 nm. Figure 7.2 (b) illustrates the XRR of the TmIG thin film fitted using Parratt's formalism and that estimated the thickness of the ≈12.2 nm, and the interfacial roughness ≈0.2 nm, which is excellent. The degree of the crystalline can also be accessed

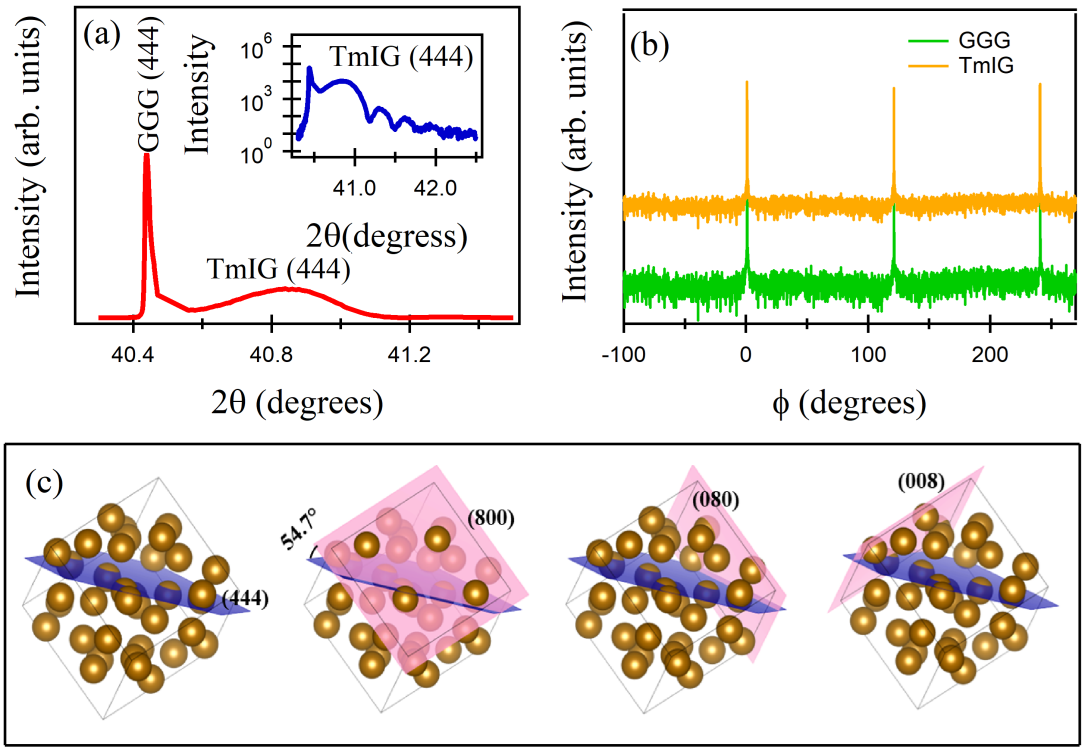

Fig. 7.1 Structural confirmation of the epitaxial TmIG thin film deposited using all-solution-based spin-coating. (a) $\theta - 2\theta$ scan of GIXRD of the substrate and the thin film with the logarithmic inset to present excellent crystallinity, (b) ϕ-scan to confirm the epitaxy with the three-fold symmetry of the (008) plan, and (c) schematic of the three-fold symmetry in (008) plane.

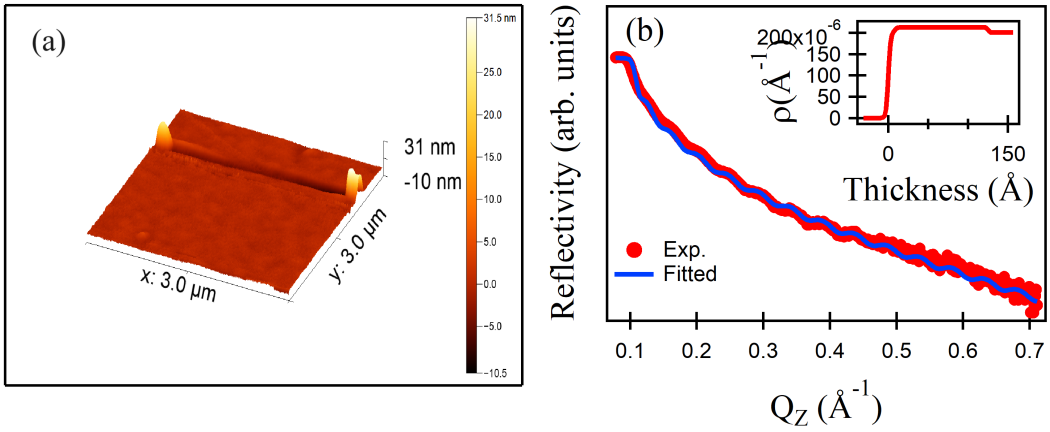

Fig. 7.2 Surface topography and the thickness and roughness study estimation using (a) atomic force microscopy and (b) x-ray reflectivity, respectively.

using the presence of Laue oscillations in the inset of Figure 7.1(a). The surface roughness estimated is ≈0.4 nm, which is in order equivalent to surface roughness estimation using AFM. The topography of the deposited thin film is smooth and suggests homogeneous growth on the substrate. Low surface and interface roughness show the potential of the sol-gel-based spin-coating method to study further applications.

7.2.3 Elemental Study

The elemental composition is probed using the XPS. Figure 7.3: depicts the survey scan and the high-resolution XPS of the TmIG thin film. Figure 7.3 (a): plot the survey scan, gives the presence of O, C, Fe, Tm, and N in the thin film. The sample constituted O, Fe, and Tm, but the environmental exposure caused the C and N absorption. The sample is calibrated using the carbon at peak position 284.2 ± 0.1 eV. Figure 7.3 (b) illustrates the high-resolution spectra of thulium $4d_{5/2}$ core electrons. $Tm_{4d_{5/2}}$ is observed at 175.7 ± 0.1 eV which is supported by the literature ((23)). Thulium is present in Tm^{2+} and Tm^{3+} but the most stable valence state is Tm^{3+}. The presence of a satellite peak at 179.2 ± 0.1 is similar to the literature and confirms Tm^{3+} charge state ((125)). Figure 7.3 (c)

illustrates the high-resolution spectra of the oxygen 1s core electrons. The main peak at binding energy 529.4 $\pm$ 0.1 eV is because the O_{1s} electrons bind in the TmIG; along with this, the surface contribution of the oxygen is also there at 530.8 $\pm$ 0.1 eV. Figure 7.3 (d) illustrates the high-resolution spectra of the iron 2p core electrons. Iron is present in a 2:3 ratio of octahedral and tetrahedral coordinates in TmIG (space group $Ia\bar{3}d$). Therefore, the Fe $2p_{3/2}$ and $2p_{1/2}$ peak comprise two peaks each. The Fe octahedral (Fe_{oct}) peaks $2p_{3/2}$ at binding energy 709.8 $\pm$ 0.1 eV and $2p_{1/2}$ at binding energy 723.1 $\pm$ 0.1 eV. The Fe tetrahedral (Fe_{tetra}) peaks $2p_{3/2}$ at binding energy 711.2 $\pm$ 0.1 eV and $2p_{1/2}$ at binding energy 724.5 $\pm$ 0.1 eV. The theoretical ratio between the area of octahedral and tetrahedral Fe is 2:3. The experimental ratio of the area of peak $Fe_{2p_{3/2}}$ octahedral and tetrahedral Fe is 0.66, and of peak $Fe_{2p_{1/2}}$ octahedral and tetrahedral Fe is 0.83 ((98)). The ratio is very close to the theoretical ratio 2:3, confirming that the quality of the sample is excellent ((98)). The difference between the core electron peak and the satellite peak is large and equivalent to the 8 eV, which further establishes that Fe is in a 3+ valence state and the stoichiometry is balanced ((111)). The atomic percentage of the constituents Tm^{3+}, Fe^{5+} and O^{2-} are 16 %, 26%, and 58%, respectively. The atomic percent is calculated using the CASAXPS software ((46)).

7.2.4 Magnetic Study

As the TmIG has application in magnonics, the magnetic properties of the deposited sample determine its application potential. Figure 7.4 presents the magnetic behaviour of the deposited all solution-based epitaxial TmIG thin film. Figure 7.4 (a) illustrates the polar MOKE measurements. The presence of out-of-plane uniaxial anisotropy gives the MOKE signal, which confirms the existence of the perpendicular magnetic anisotropy (PMA) at room temperature in the thin film ((103)). The uniaxial anisotropy (K_U) in the thin film is a combination of various components like stress-induced anisotropy (K_σ), magneto-

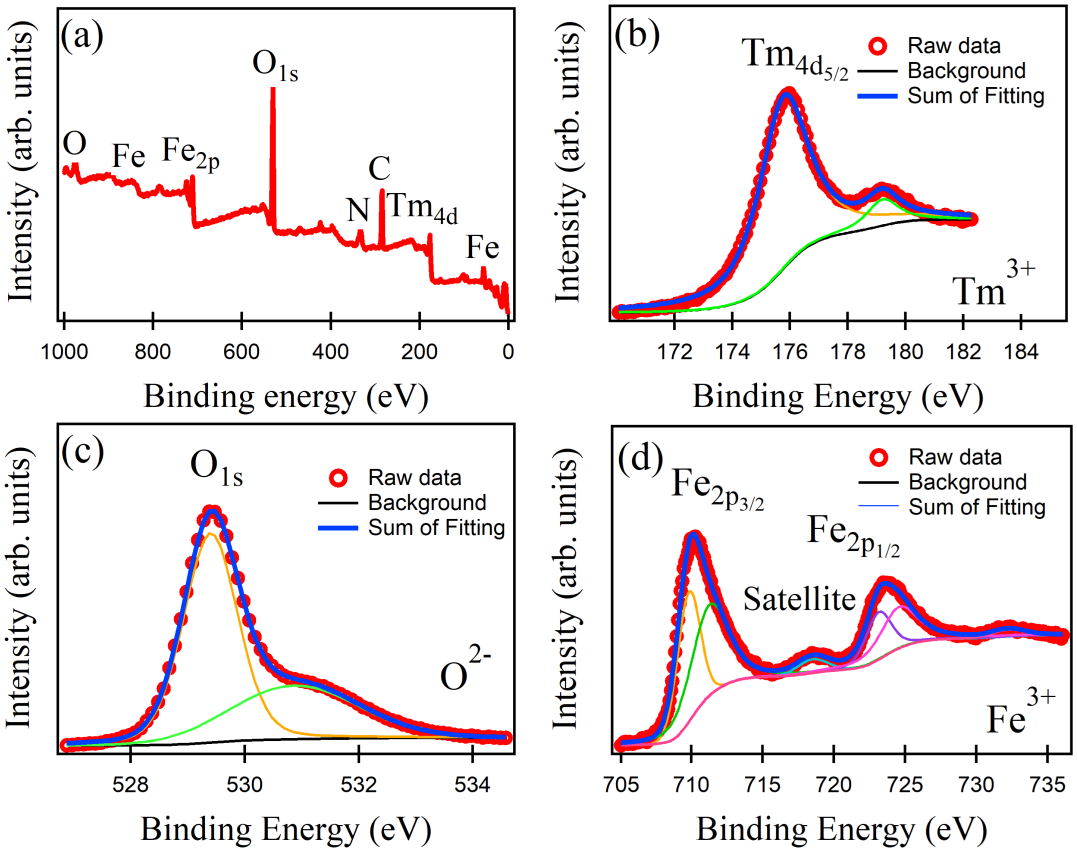

Fig. 7.3 XPS of the TmIG thin film has been presented. (a) survey scan from binding energy 0-1000 eV. High-resolution XPS of the elements (b) Tm^{3+}, (C) O^{2-} and (d) Fe^{3+} are fitted and presented with peak component with the Shirley background.

crystalline anisotropy (K_M), and shape anisotropy (K_S) ((14)). Figure 7.4 (b) illustrates the schematics of the PMA in the film. The stress-induced anisotropy is calculated using the formula as follows:

$$K_\sigma = -\frac{3}{2}\lambda_{111}\sigma \tag{7.2}$$

where, λ_{111} is the magnetostriction constant (-5.2 $\times 10^{-6}$) of the TmIG as present in literature ((133)). The value of the estimated stress-induced anisotropy (K_σ) is $20.07\times10^3\pm$ 5.71 $\times 10^{-2}$ N/m^2. Shape anisotropy (K_S) estimated is 0.49 $\times 10^3$ N/m^2. The cubic anisotropy constant (K_1) value is taken from the literature((103)) is -1.1$\times 10^3$ N/m^2. The final uniaxial anisotropy value is estimated as follows:

$$K_U = -\frac{K_1}{12} + K_\sigma + K_S \tag{7.3}$$

where, $K_1/12$ is K_M. The estimated K_U from the strain is 20.11 $\times 10^3$ N/m^2.

The magnetic study of the TmIG is also performed using FMR. It probes the precession of the moments along the external field, and this precession resonates with the applied frequency. The absorption of that frequency at a particular magnetic field gives the resonance magnetic field and the linewidth of the absorption, which signifies the moment's precession and energy dissipation, respectively. Figure 7.4: depicts the FMR results, (a) plots in-plane the resonance magnetic field (H_{res}) as a function of frequency and fitted using Kittel equation, (b) illustrates the linewidth as a function of the frequency. Kittel equation ((22, 134)) is as presented below:

$$f = \left(\frac{\gamma}{2\pi}\right)\sqrt{H(H+\mu_0 M_{eff})} \tag{7.4}$$

The effective magnetization ($\mu_0 M_{eff}$) estimated is -0.292 $\pm$ 0.003 T. As the PMA is confirmed with the polar MOKE, the negative value of $\mu_0 M_{eff}$ shows that anisotropy

dominates the saturation magnetization. $\mu_0 M_{eff}$ is composed of saturation magnetization ($\mu_0 M_S$) and the anisotropy field (H_U) in following equation((14)):

$$\mu_0 M_{eff} = \mu_0 M_S - H_U \tag{7.5}$$

In literature, the value of saturation magnetization ($\mu_0 M_S$) of bulk TmIG is 0.1244 T ((127)). The anisotropy Field (H_U) is estimated to be 0.4167 T. The anisotropy constant (K_U) is calculated by substituting the anisotropy field and saturation magnetization as present in the following equation:

$$K_U = \frac{H_U \times M_S}{2} \tag{7.6}$$

K_U is estimated by substituting, the values is $20.6\times10^3 \pm 0.2\times10^3$ N/m^2. K_U estimation by FMR is equivalent to the K_U calculated with the strain in GIXRD. This value is higher than the literature due to the self-growth of the TmIG/GGG and form a better interface. The value of the gyromagnetic ratio is 19.46 $\pm$ 0.09 GHz/T, which is lower than the free electron because of the high spin-orbit coupling of the thulium ions. The Landé g-factor estimated is 1.391 $\pm$ 0.006 from the gyromagnetic ratio. The Landé g-factor is smaller than the free electron as well as the value present for TmIG in literature((134)). The presence of low Landé g-factor can be due to the presence of high anisotropy present in TmIG/GGG thin film. The uniform mode is generated while the moment precession relaxes by the dissipating energy due to extrinsic and intrinsic factors. Extrinsic factors are like defects and electro-electron interaction, and intrinsic factors are like two-magnon interaction and high spin-orbit interaction. These factors can be obtained from the linear fitting of the magnetic linewidth as a function of the applied frequency. Figure 7.4 (d) depicts the linewidth (ΔH) as a function of the applied frequency. Yellow dots are obtained by analyzing the experimental FMR data as a function of the applied field (the intensity of

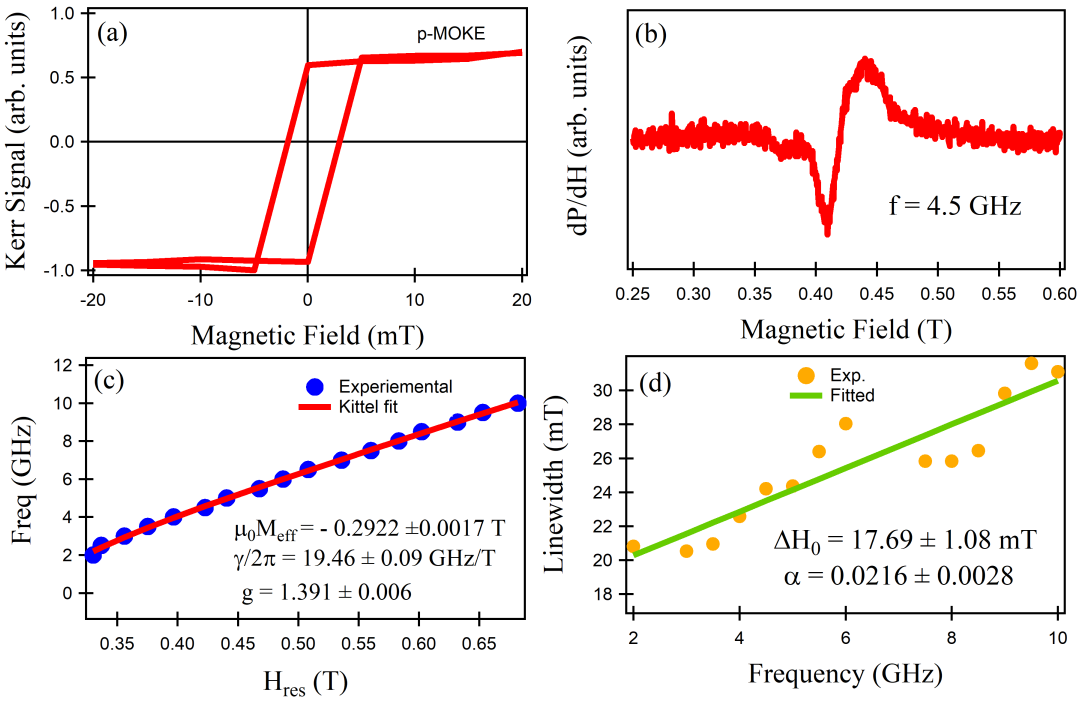

Fig. 7.4 FMR study of the TmIG thin film (a) Kittel fitting to the resonance magnetic field to study effective magnetic field and gyromagnetic ratio. (b) Linear fit to the linewidth as a function of frequency

the dP/dH is low, which causes the deviation), and the green line fits them linearly. The relation of linewidth, intrinsic, and extrinsic damping parameters is as follows:

$$\Delta H = \Delta H_0 + \frac{4\pi\alpha}{\gamma} f \tag{7.7}$$

The ΔH_0 is the extrinsic part of the TmIG energy dissipation, and the fitted value is the ΔH_0 is 17.69 $\pm$ 1.08 mT. The intrinsic dissipation is stated as the Gilbert damping parameter (α) = 0.0216 $\pm$ 0.0028. Gilbert damping parameter is of the same order as the present in literature in which samples are prepared with sophisticated methods ((103)).

This article presents a cost-effective method and to understand it the literature is compared with experimental observation in table 7.1. All the samples are grown on the GGG (111) substrate, and the thicknesses are different, but the Gilbert damping parameter

Table 7.1 The comparison of the present deposited TmIG/GGG with the literature.

Substrate	Deposition Method	Thickness (nm)	Damping Parameter	Anisotropy constant (10^3 N/m^2)	reference
GGG (111)	Sol-gel-based Spin-coating	12.2	0.0216	20.6	present
GGG (111)	PLD	29	0.013	9	((106))
GGG (111)	PLD	20 - 300	0.02	10	((29))
GGG (111)	sputtering	9	0.013	-	((127))
GGG (111)	PLD	8	-	11.88	((103))

is of the same order. The estimated K_U is higher compared to the literature and is supported by the lower value of the Landé g-factor of the present work.

7.3 Summary

Sol-gel-based spin coating is utilized to deposit the epitaxial thulium iron garnet (TmIG) thin film on the GGG substrate. The elemental analysis confirms the stoichiometric deposition with the low interface and the surface roughness. The presence of the perpendicular magnetic anisotropy of this all-solution method deposited TmIG due to the stress-induced anisotropy. Due to the presence of the high spin-orbit coupling gives rise to the lower gyromagnetic ratio and Landé g-factor, which is well matched with the literature. The intrinsic and extrinsic dissipation factors of TmIG present a potential for the deposition method. With further improvements, this cost-effective method of deposition has the potential to be used for magnonics applications.

Chapter 8

Conclusion and Future Scope

8.1 Conclusion

This thesis presents the synthesis of YIG and TmIG using the sol-gel-based spin-coating. As the literature reports the sophisticated methods like PLD, LPE and RF sputtering as the method of deposition of iron garnets. Thus method with the further accessibility with the clean room and controlled atmosphere can substitute these with low cost deposition ability.

In **chapter 4** of the thesis presents a optimization of the YIG annealing parameters. The structural study and the elemental study confirms the polycrystalline YIG with the maintained stoichiometry and the presence of Y^{3+}, Fe^{3+} cations that have been calibrated with the carbon's binding energy. The magnetic study confirms the effective magnetization of 0.1887 T and α is 5.93 $\times$ $10^{-3}\pm$ 0.5$\times 10^{-3}$ with the linewidth because of inhomogeneous contribution is 5.049 $\pm$ 0.3 mT. The α value is lower then the previously solution based method and the higher inhomomogeneous contribution has source in the grain boundaries and the defects.

In **chapter 5** epitaxial ($\approx$ 18 nm) YIG thin film on the GGG (111) single crystal has been grown and its magnetic properties are discussed. Strain calculation is done using the synchrotron GIXRD. The considering magnetostriction constant from the literature

the stress-induced magnetic anisotropy has been estimated to be $K_\sigma = 4.44 \pm 2.2\times10^{-3}$ kN/m^2. The uniaxial anisotropy estimated by the FMR has been $K_U = 4.69$ kN/m^2. This chapter confirms the significant contribution to the uniaxial anisotropy is stress-induced magnetic anisotropy.

In **chapter 6** polycrystalline TmIG thin film of thickness ≈22 nm thickness has been grown on the thermally oxidized Si(100). The atomic percentage of the elements are confirmed with the XPS. The Low compensation temperature of ≈15 K is experimentally proven in align with the available literature. The low temperature modulated ferromagnetism and the room temperature ferrimagnetic state has been observed with the SQUID-VSM.

In **chapter 7** high crystalline epitaxial TmiG of thickness ≈12.2 nm has been grown on the GGG(111) single crystal using the sol-gel-based spin coating. The epitaxy of the thin film is confirmed with the synchrotron GIXRD. The high SOC in the TmIG causes decrease in the Land g-factor. The high uniaxial anisotropy is reason of the PMA in the thin film. The confirmation of PMA is performed with the polar-MOKE. The significant contribution of the uniaxial anistropy is stress-induced anisotropy. The damping parameter estimated with the FMR is 0.0216, which is equivalent to the PLD grown samples.

8.2 Future Scope

Further improve the quality of the thin film, synthesis is to be performed in the clean room and the controlled environment to enhance the surface quality and but lower defects. The inverse spin Hall effect measurements has to conduct to measure the spin Hall angle in the YIG thin films to built a conduit with the lithography and study the magnonic propagation length and group velocity of the same.

The higher order spin wave excitation are observed in the epitaxial YIG, to study and confirmed its origin is also important for the theoretical understanding. The presence of

stress-induced anisotropy on the dispersion curve is needed to understand to simulate the experimental one.

The epitaxial TmIG shows the spin-orbit torque (SOT). The further experiments to be performed SOT measurement to observe the application potential. Because of the presence of the PMA, it potential for the device fabrication can be explored. The magnonics devices with the heavy metal interface are execellent for memory and logic gates fabrications.

Bibliography

[1] Michael D Abràmoff, Paulo J Magalhães, and Sunanda J Ram. Image processing with imagej. *Biophotonics international*, 11(7):36–42, 2004.

[2] Philip W Anderson and John M Rowell. Probable observation of the josephson superconducting tunneling effect. *Physical Review Letters*, 10(6):230, 1963. doi:10.1103/PhysRevLett.10.230.

[3] SN Andrianov and SA Moiseev. Magnon qubit and quantum computing on magnon $Bose-Einstein$ condensates. *Physical Review A*, 90(4):042303, 2014. doi:https://doi.org/10.1103/PhysRevA.90.042303.

[4] Muhammad Faiz Ashri, Nik Akmal Rejab, Zainal Arifin Ahmad, Norazharuddin Shah Abdullah, Nur Azam Badarulzaman, Raja Azlan Amirul Raja Mat, and Wan Fahmin Faiz Wan Ali. Densification and grain growth of microwave-sintered yttrium iron garnet. 2068(1):020107, 2019. doi:https://doi.org/10.1063/1.5089406s.

[5] Can Onur Avci, Andy Quindeau, Maxwell Mann, Chi-Feng Pai, Caroline A Ross, and Geoffrey SD Beach. Spin transport in as-grown and annealed thulium iron garnet/platinum bilayers with perpendicular magnetic anisotropy. *Physical Review B*, 95(11):115428, 2017.

[6] Can Onur Avci, Andy Quindeau, Chi-Feng Pai, Maxwell Mann, Lucas Caretta, Astera S Tang, Mehmet C Onbasli, Caroline A Ross, and Geoffrey SD Beach. Current-induced switching in a magnetic insulator. *Nature materials*, 16(3):309–314, 2017. doi:10.1038/NMAT4812.

[7] P. Barla, V. K. Joshi, and S. Bhat. Spintronic devices: a promising alternative to cmos devices. *Journal of Computational Electronics*, 20(2):805–837, 2021. doi:https://doi.org/10.1007/s10825-020-01648-6.

[8] Jackson J Bauer, Ethan R Rosenberg, Subhajit Kundu, K Andre Mkhoyan, Patrick Quarterman, Alexander J Grutter, Brian J Kirby, Julie A Borchers, and Caroline A Ross. Dysprosium iron garnet thin films with perpendicular magnetic anisotropy on silicon. *Advanced Electronic Materials*, 6(1):1900820, 2020.

[9] JJ Bauer, ER Rosenberg, and CA Ross. Perpendicular magnetic anisotropy and spin mixing conductance in polycrystalline europium iron garnet thin films. *Applied Physics Letters*, 114(5), 2019.

[10] J.M. Beaujour, D. Ravelosona, I. Tudosa, E.E. Fullerton, and A.D. Kent. Ferromagnetic resonance linewidth in ultrathin films with perpendicular magnetic anisotropy. *Phys. Rev. B*, 80(18):180415, 2009. doi:https://doi.org/10.1103/PhysRevB.80.180415.

[11] Félix Bertaut and Francis Forrat. Structure des ferrites ferrimagnetiques des terres rares. *Comptes rendus hebdomadaires des seances de l academie des sciences*, 242 (3):382–384, 1956.

[12] Patrick Bertrand. *Electron Paramagnetic Resonance Spectroscopy: Applications*. Springer Nature, 2020.

[13] B. Bhoi and M. S. Diware. Preferred-oriented polycrystalline $Y_3Fe_5O_{12}$ films grown on quartz with low microwave loss. *J. Am. Ceram. Soc.*, 104(6):2423–2427, 2021. doi:10.1111/jace.17675.

[14] B. Bhoi, B. Kim, Y. Kim, M.-K. Kim, J.-H. Lee, and S.-K. Kim. Stress-induced magnetic properties of *PLD*-grown high-quality ultrathin *YIG* films. *Journal of Applied Physics*, 123(20), 2018. doi:https://doi.org/10.1063/1.5031198.

[15] Biswanath Bhoi, N Venkataramani, Shiva Prasad, RPRC Aiyar, Gulshan Kumar, I Samajdar, and M Kostylev. Observation of enhanced magnetic anisotropy in pld yig thin film on ggg (1 1 1) substrate. *Journal of Magnetism and Magnetic Materials*, 483:191–195, 2019. doi:https://doi.org/10.1016/j.jmmm.2019.03.111.

[16] G. Binasch, P. Grünberg, F. Saurenbach, and W. Zinn. Enhanced magnetoresistance in layered magnetic structures with antiferromagnetic interlayer exchange. *Phys. rev. B*, 39(7):4828, 1989. doi:https://doi.org/10.1103/PhysRevB.39.4828.

[17] Felix Bloch. Zur theorie des ferromagnetismus. *Zeitschrift für Physik*, 61(3-4): 206–219, 1930.

[18] Stephen Blundell. Magnetism in condensed matter, 2003.

[19] Toufik Boudiar, Beatrice Payet-Gervy, M-F Blanc-Mignon, J-J Rousseau, Martine Le Berre, and Hélène Joisten. Magneto-optical properties of yttrium iron garnet (*YIG*) thin films elaborated by radio frequency sputtering. *J. Magn. Magn. Mater.*, 284:77, 2004. doi:https://doi.org/10.1016/j.jmmm.2004.06.046.

[20] H Buhay, JD Adam, MR Daniel, NJ Doyle, MC Driver, GW Eldridge, MH Hanes, RL Messham, and MM Sopira. Thick yttrium-iron-garnet (yig) films produced by pulsed laser deposition (pld) for integration applications. *IEEE Transactions on Magnetics*, 31(6):3832–3834, 1995. doi:10.1109/20.489787.

[21] C Burrowes, B Heinrich, B Kardasz, EA Montoya, E Girt, Yiyan Sun, Young-Yeal Song, and Mingzhong Wu. Enhanced spin pumping at yttrium iron garnet/au interfaces. *Appl. Phys. Lett.*, 100(9):092403, 2012. doi:https://doi.org/10.1063/1.3690918.

[22] Houchen Chang, PA Praveen Janantha, Jinjun Ding, Tao Liu, Kevin Cline, Joseph N Gelfand, Wei Li, Mario C Marconi, and Mingzhong Wu. Role of damping in spin seebeck effect in yttrium iron garnet thin films. *Science advances*, 3(4):e1601614, 2017.

[23] Jill Chastain and Roger C King Jr. Handbook of x-ray photoelectron spectroscopy. *Perkin-Elmer Corporation*, 40:221, 1992.

[24] P. Che, Y. Zhang, C. Liu, S. Tu, Z. Liao, D. Yu, F. A. Vetro, J.P. Ansermet, W. Zhao, and L. Bi. Short-wavelength spin waves in yttrium iron garnet micro-channels on silicon. *IEEE Magn. Lett.*, 7:1–4, 2016. doi:10.1109/LMAG.2016.2616105.

[25] Vladimir Cherepanov, Igor Kolokolov, and Victor L'vov. The saga of *YIG*: Spectra, thermodynamics, interaction and relaxation of magnons in a complex magnet. *Physics reports*, 229(3):81–144, 1993. doi:https://doi.org/10.1016/0370-1573(93)90107-O.

[26] D.S. Chrischon, F. Beck, K.D. Sossmeier, and M. Carara. *FMR* linewidth and the crystallization processes in *Co*-based amorphous microwires. *J. Magn. Magn. Mater.*, 336:66, 2013. doi:https://doi.org/10.1016/j.jmmm.2013.01.038.

[27] A. V. Chumak, V. I. Vasyuchka, A. A. Serga, and B. Hillebrands. Magnon spintronics. *Nat. Phys.*, 11(6):453, 2015. doi:https://doi.org/10.1038/nphys3347.

[28] AV Chumak, AA Serga, and B Hillebrands. Magnonic crystals for data processing. *Journal of Physics D: Applied Physics*, 50(24):244001, 2017.

[29] O. Ciubotariu, A. Semisalova, K. Lenz, and M. Albrecht. Strain-induced perpendicular magnetic anisotropy and gilbert damping of $Tm_3Fe_5O_{12}$ thin films. *Scientific reports*, 9(1):17474, 2019. doi:https://doi.org/10.1038/s41598-019-53255-6.

[30] John Clarke and Alex I Braginski. The squid handbook. vol. 2. applications of squids and squid systems. 2006.

[31] M. Collet, O. Gladii, M. Evelt, V. Bessonov, L. Soumah, P. Bortolotti, S.O. Demokritov, Y. Henry, V. Cros, M. Bailleul, et al. Spin-wave propagation in ultra-thin *YIG* based waveguides. *Appl. Phys. Lett.*, 110(9):092408, 2017. doi:https://doi.org/10.1063/1.4976708.

[32] Bernard Dennis Cullity and Chad D Graham. *Introduction to magnetic materials*. John Wiley & Sons, 2011.

[33] Y Dai, SJ Xu, SW Chen, XL Fan, DZ Yang, DS Xue, DS Song, J Zhu, SM Zhou, and Xuepeng Qiu. Observation of giant interfacial spin hall angle in y 3 fe 5 o 12/pt heterostructures. *Physical Review B*, 100(6):064404, 2019.

[34] O. d'Allivy Kelly, A. Anane, R. Bernard, J. Ben Youssef, C. Hahn, A. H. Molpeceres, C. Carrétéro, E. Jacquet, C. Deranlot, P. Bortolotti, et al. Inverse spin hall effect in nanometer-thick yttrium iron garnet/*Pt* system. *Appl. Phys. Lett.*, 103(8):082408, 2013. doi:https://doi.org/10.1063/1.4819157.

[35] S. Datta and B. Das. Electronic analog of the electro-optic modulator. *Appl. Phys. Lett.*, 56(7):665–667, 1990. doi:https://doi.org/10.1063/1.102730.

[36] DD Davis and RM Bozorth. Magnetic properties of thulium metal. *Physical Review*, 118(6):1543, 1960.

[37] BW Delf, A Green, and RJ Stevens. Sputtering of yttrium iron garnet (yig) thin films from a powder mixture of fe2o3 and y2o3. *physica status solidi (a)*, 13(2): 493–498, 1972. doi:https://doi.org/10.1002/pssa.2210130218.

[38] Jinjun Ding, Chuanpu Liu, Yuejie Zhang, Uppalaiah Erugu, Zhiyong Quan, Rui Yu, Ethan McCollum, Songyu Mo, Sheng Yang, Haifeng Ding, et al. Nanometer-thick yttrium iron garnet films with perpendicular anisotropy and low damping. *Physical Review Applied*, 14(1):014017, 2020.

[39] Jinjun Ding, Tao Liu, Houchen Chang, and Mingzhong Wu. Sputtering growth of low-damping yttrium-iron-garnet thin films. *IEEE Magnetics Letters*, 11:1–5, 2020. doi:10.1109/LMAG.2020.2989687.

[40] Gerald F Dionne. *Magnetic oxides*, volume 14. 2009.

[41] Carsten Dubs, Oleksii Surzhenko, Ronny Thomas, Julia Osten, Tobias Schneider, Kilian Lenz, Jörg Grenzer, René Hübner, and Elke Wendler. Low damping and microstructural perfection of sub-40nm-thin yttrium iron garnet films grown by liquid phase epitaxy. *Physical Review Materials*, 4(2):024416, 2020. doi:10.1103/PhysRevMaterials.4.024416.

[42] Viet Duc Duong, Phuoc Cao Van, Trinh Nguyen Thi, Ha Yeong Ahn, Viet Anh Cao, Junghyo Nah, Ganghwi Kim, Ki-Suk Lee, Ji-Wan Kim, and Jong-Ryul Jeong. Interfacial roughness driven manipulation of magnetic anisotropy and coercivity in ultrathin thulium iron garnet films. *Journal of Alloys and Compounds*, 927:166800, 2022. doi:https://doi.org/10.1016/j.jallcom.2022.166800.

[43] JR Eshbach and RW Damon. Surface magnetostatic modes and surface spin waves. *Physical Review*, 118(5):1208, 1960.

[44] P Etienne, G Creuzet, A Friederich, F Nguyen-Van-Dau, A Fert, and J Massies. Molecular beam epitaxial growth of fe/cr multilayers on (001) gaas. *Appl. phys. lett.*, 53(2):162–164, 1988. doi:https://doi.org/10.1063/1.100353.

[45] Paul P Ewald. Die intensität der interferenzflecke bei zinkblende und das gitter der zinkblende. *Annalen der Physik*, 349(10):257–282, 1914. doi:10.1002/andp.19143491005.

[46] N. Fairley, V. Fernandez, M. Richard-Plouet, C. Guillot-Deudon, J. Walton, E. Smith, D. Flahaut, M. Greiner, M. Biesinger, and S. Tougaard. Systematic and collaborative approach to problem solving using x-ray photoelectron spectroscopy. *Appl. Surf. Sci. Adv.*, 5:100112, 2021. doi:https://doi.org/10.1016/j.apsadv.2021.100112.

[47] ID Feranchuk, SI Feranchuk, L Komarov, S Sytova, and A Ulyanenkov. Analytical ansatz for self-consistent calculations of x-ray transmission and reflection coefficients at graded interfaces. *Physical Review B*, 67(23):235417, 2003.

[48] A. Fert, V. Cros, and J. Sampaio. Skyrmions on the track. *Nat. nanotech.*, 8(3): 152–156, 2013. doi:https://doi.org/10.1038/nnano.2013.29.

[49] B. Flebus, S. M. Rezende, D. Grundler, and A. Barman. Recent advances in magnonics. *Journal of Applied Physics*, 133(4):160401, 2023. doi:https://doi.org/10.1063/5.0153424.

[50] DB Fraser, EM Gyorgy, RC LeCraw, JP Remeika, FJ Schnettler, and LG Van Uitert. New acoustic and magnetic properties of *YIG* and *YAG* with small mn and ni additions. *J. Appl. Phys.*, 36(3):1016, 1965. doi:https://doi.org/10.1063/1.1714078.

[51] J Fu, M Hua, X Wen, M Xue, S Ding, M Wang, P Yu, S Liu, J Han, C Wang, H Du, Y Yang, and J Yang. Epitaxial growth of $Y_3Fe_5O_{12}$ thin films with perpendicular magnetic anisotropy. *Applied Physics Letters*, 110(20), 2017. doi:10.1063/1.4983783.

[52] Jialiang Gao, Charles-Henri Lambert, Richard Schlitz, Manfred Fiebig, Pietro Gambardella, and Saül Vélez. Magnon transport and thermoelectric effects in ultrathin tm 3 fe 5 o 12/pt nonlocal devices. *Physical Review Research*, 4(4):043214, 2022.

[53] Kevin Garello, Can Onur Avci, Ioan Mihai Miron, Manuel Baumgartner, Abhijit Ghosh, Stéphane Auffret, Olivier Boulle, Gilles Gaudin, and Pietro Gambardella. Ultrafast magnetization switching by spin-orbit torques. *Applied Physics Letters*, 105(21), 2014. doi:https://doi.org/10.1063/1.4902443.

[54] S Geller and MA Gilleo. Structure and ferrimagnetism of yttrium and rare-earth–iron garnets. *Acta Crystallogr.*, 10(3):239, 1957. doi:https://doi.org/10.1107/S0365110X57000729.

[55] T. L. Gilbert. A phenomenological theory of damping in ferromagnetic materials. *IEEE Trans. Magn.*, 40(6):3443–3449, 2004. doi:10.1109/TMAG.2004.836740.

[56] MA Gilleo. Ferromagnetic insulators: garnets. *Handbook of Ferromagnetic Materials*, 2:1–53, 1980.

[57] J. B. Goodenough. Goodenough-Kanamori rule. *Scholarpedia*, 3(10):7382, 2008. doi:10.4249/scholarpedia.7382. revision #122456.

[58] Peter CJ Graat and Marcel AJ Somers. Simultaneous determination of composition and thickness of thin iron-oxide films from xps fe 2p spectra. *Applied Surface Science*, 100:36–40, 1996. doi:10.1016/0169-4332(96)00252-8.

[59] James HE Griffiths. Anomalous high-frequency resistance of ferromagnetic metals. *Nature*, 158(4019):670–671, 1946. doi:https://doi.org/10.1038/158670a0.

[60] AP Grosvenor, BA Kobe, Mark C Biesinger, and NS McIntyre. Investigation of multiplet splitting of fe 2p xps spectra and bonding in iron compounds. *Surface and Interface Analysis: An International Journal devoted to the development and application of techniques for the analysis of surfaces, interfaces and thin films*, 36 (12):1564–1574, 2004.

[61] Paweł Gruszecki, Maciej Kasprzak, Andriy E Serebryannikov, Maciej Krawczyk, and Wojtek Śmigaj. Microwave excitation of spin wave beams in thin ferromagnetic films. *Scientific reports*, 6(1):1–8, 2016. doi:https://doi.org/10.1038/srep22367.

[62] C. Hahn, G. De Loubens, O. Klein, M. Viret, V. V. Naletov, and J. Youssef. Comparative measurements of inverse spin hall effects and magnetoresistance in YIG/Pt and YIG/Ta. *Phys. Rev. B*, 87(17):174417, 2013. doi:https://doi.org/10.1103/PhysRevB.87.174417.

[63] M Haidar, P Dürrenfeld, M Ranjbar, M Balinsky, M Fazlali, M Dvornik, RK Dumas, Sergiy Khartsev, and Johan Åkerman. Controlling gilbert damping in a yig film using nonlocal spin currents. *Phys. Rev. B*, 94(18):180409, 2016. doi:10.1103/PhysRevB.94.180409.

[64] P. Hansen, K. Witter, and W. Tolksdorf. Magnetic and magneto-optic properties of lead-and bismuth-substituted yttrium iron garnet films. *Physical Review B*, 27(11): 6608, 1983. doi:https://doi.org/10.1103/PhysRevB.27.6608.

[65] George F Harrington and José Santiso. Back-to-basics tutorial: X-ray diffraction of thin films. *Journal of Electroceramics*, 47(4):141–163, 2021. doi:https://doi.org/10.1007/s10832-021-00263-6.

[66] C. Hauser, T. Richter, N. Homonnay, C. Eisenschmidt, M. Qaid, H. Deniz, D. Hesse, M. Sawicki, S.G. Ebbinghaus, and G. Schmidt. Yttrium iron garnet thin films with very low damping obtained by recrystallization of amorphous material. *Scientific reports*, 6(1):1–8, 2016. doi:10.1038/srep20827.

[67] B. Heinrich, C. Burrowes, E. Montoya, B. Kardasz, E. Girt, Y.-Y. Song, Y. Sun, and M. Wu. Spin pumping at the magnetic insulator (YIG)/normal metal (Au) interfaces. *Phys. Rev. Lett.*, 107(6):066604, 2011. doi:https://doi.org/10.1103/PhysRevLett.107.066604.

[68] Werner Heisenberg. Zur theorie des ferromagnetismus. In *Original Scientific Papers Wissenschaftliche Originalarbeiten*, pages 580–597. Springer, 1985. doi:10.1007/BF01328601.

[69] M. C. Hickey and J. S. Moodera. Origin of intrinsic gilbert damping. *Phys. rev. lett.*, 102(13):137601, 2009. doi:10.1103/PhysRevLett.102.137601.

[70] A. Hirohata, K. Yamada, Y. Nakatani, I. Prejbeanu, B. Diény, P. Pirro, and B. Hillebrands. Review on spintronics: Principles and device applications. *J Magn.and Magn. Mater.*, 509:166711, 2020. doi:https://doi.org/10.1016/j.jmmm.2020.166711.

[71] MJ Hurben and CE Patton. Theory of magnetostatic waves for in-plane magnetized isotropic films. *Journal of Magnetism and Magnetic Materials*, 139(3):263–291, 1995.

[72] MJ Hurben and CE Patton. Theory of two magnon scattering microwave relaxation and ferromagnetic resonance linewidth in magnetic thin films. *Journal of applied physics*, 83(8):4344–4365, 1998. doi:https://doi.org/10.1063/1.367194.

[73] M. Jackson. Magnetism of rare earth. *The IRM quarterly*, 10(3):1, 2000.

[74] Brian David Josephson. Possible new effects in superconductive tunnelling. *Physics letters*, 1(7):251–253, 1962. doi:10.1016/0031-9163(62)91369-0.

[75] Y Kajiwara, K Harii, S Takahashi, Jun-ichiro Ohe, K Uchida, M Mizuguchi, H Umezawa, H Kawai, Kazuya Ando, K Takanashi, et al. Transmission of electrical signals by spin-wave interconversion in a magnetic insulator. *Nature*, 464(7286): 262–266, 2010.

[76] Sangita S Kalarickal, Pavol Krivosik, Mingzhong Wu, Carl E Patton, Michael L Schneider, Pavel Kabos, Thomas J Silva, and John P Nibarger. Ferromagnetic resonance linewidth in metallic thin films: Comparison of measurement methods. *Journal of Applied Physics*, 99(9), 2006. doi:10.1063/1.2197087.

[77] Charles Kittel. Interpretation of anomalous larmor frequencies in ferromagnetic resonance experiment. *Physical Review*, 71(4):270, 1947.

[78] Charles Kittel. On the theory of ferromagnetic resonance absorption. *Physical review*, 73(2):155, 1948.

[79] S. Klingler, H. Maier-Flaig, C. Dubs, O. Surzhenko, R. Gross, H. Huebl, S. T. B. Gönnenwein, and M. Weiler. Gilbert damping of magnetostatic modes in a yttrium iron garnet sphere. *Appl. Phys. Lett.*, 110(9):092409, 2017. doi:http://dx.doi.org/10.1063/1.4977423.

[80] BB Krichevtsov, AM Korovin, SV Gastev, SM Suturin, KV Mashkov, M Sawada, and NS Sokolov. Magnetization reversal in $Co/GGG/YIG/GGG$ (1 1 1) nanoheterostructures: Interlayer magnetic coupling and orange peel effect. *Journal of Magnetism and Magnetic Materials*, 502:166542, 2020. doi:https://doi.org/10.1016/j.jmmm.2020.166542.

[81] Kannan M Krishnan. *Fundamentals and applications of magnetic materials*. Oxford University Press, 2016.

[82] Y Krockenberger, K-S Yun, T Hatano, S Arisawa, M Kawasaki, and Y Tokura. Layer-by-layer growth and magnetic properties of $Y_3Fe_5O_{12}$ thin films on $Gd_3Ga_5O_{12}$. *Journal of Applied Physics*, 106(12), 2009.

[83] A. Krysztofik, S. Özoğlu, and E. Coy. Magnetization damping in nanocrystalline yttrium iron garnet thin films grown on oxidized silicon. *IEEE Magn. Lett.*, 12:1–5, 2021. doi:10.1109/LMAG.2021.3086454.

[84] A. Krysztofik, N. Kuznetsov, H. Qin, L. Flajšman, E. Coy, and S. van Dijken. Tuning of magnetic damping in $Y_3Fe_5O_{12}$/metal bilayers for spin-wave conduit termination. *Materials*, 15(8):2814, 2022. doi:10.3390/ma15082814.

[85] Naresh Kumar, NG Kim, YA Park, N Hur, JH Jung, KJ Han, and KJ Yee. Epitaxial growth of terbium iron garnet thin films with out-of-plane axis of magnetization. *Thin Solid Films*, 516(21):7753–7757, 2008.

[86] Yan Li, Yiheng Wu, Liuwei Xu, Qi Gu, Shuaihua Wang, Xieming Xu, Xianhui Zhang, and Shaofan Wu. Enhancement in the magnetic properties of cr 3+ and ce 3+ substitution thulium iron garnet synthesized via sol-gel route. *Journal of Superconductivity and Novel Magnetism*, 34:1459–1466, 2021.

[87] QB Liu, KK Meng, ZD Xu, Tao Zhu, XG Xu, J Miao, and Y Jiang. Unusual anomalous hall effect in perpendicularly magnetized yig films with a small gilbert damping constant. *Physical Review B*, 101(17):174431, 2020.

[88] T. Liu, H. Chang, V. Vlaminck, Y. Sun, M. Kabatek, A. Hoffmann, L. Deng, and M. Wu. Ferromagnetic resonance of sputtered yttrium iron garnet nanometer films. *J. Appl. Phys.*, 115(17):17A501, 2014. doi:https://doi.org/10.1063/1.4852135.

[89] Xiaoyong Liu, Wenzhe Zhang, Matthew J Carter, and Gang Xiao. Ferromagnetic resonance and damping properties of *CoFeB* thin films as free layers in *MgO*-based magnetic tunnel junctions. *Journal of Applied Physics*, 110(3), 2011. doi:https://doi.org/10.1063/1.3615961.

[90] Rong Ma, Ming Liu, Jiannong Wang, and Hong Wang. The room temperature deposition of high-quality epitaxial yttrium iron garnet thin film via *RF* sputtering. *Journal of Alloys and Compounds*, 708:213–219, 2017. doi:http://dx.doi.org/10.1016/j.jallcom.2017.02.275.

[91] Ivan S Maksymov and Mikhail Kostylev. Broadband stripline ferromagnetic resonance spectroscopy of ferromagnetic films, multilayers and nanostructures. *Physica E: Low-dimensional Systems and Nanostructures*, 69:253–293, 2015. doi:https://doi.org/10.1016/j.physe.2014.12.027.

[92] John S McCloy and Brian Walsh. Sublattice magnetic relaxation in rare earth iron garnets. *IEEE Transactions on magnetics*, 49(7):4253–4256, 2013. doi:10.1109/TMAG.2013.2238510.

[93] Takafumi Miyazaki, Youji Tokumoto, Ryohei Sumii, Hajime Yagi, Noriko Izumi, Hisanori Shinohara, and Shojun Hino. Photoelectron spectra of thulium atoms encapsulated c82 fullerene, tm2@ c82 (iii) and tm2c2@ c82 (iii). *Chemical Physics*, 431:47–50, 2014.

[94] Q. I. Mohaidat, M. Lataifeh, K. Hamasha, S. H. Mahmood, I. Bsoul, and M. Awawdeh. The structural and the magnetic properties of aluminum substituted yttrium iron garnet. *Mater. Res.*, 21, 2018. doi:https://doi.org/10.1590/1980-5373-MR-2017-0808.

[95] Björn Obry, Philipp Pirro, Thomas Brächer, Andrii V Chumak, Julia Osten, Florin Ciubotaru, Alexander A Serga, Jürgen Fassbender, and Burkard Hillebrands. A micro-structured ion-implanted magnonic crystal. *Applied Physics Letters*, 102(20), 2013. doi:https://doi.org/10.1063/1.4807721.

[96] Robert C O'handley. *Modern magnetic materials: principles and applications*. Wiley, 2000.

[97] M.C. Onbasli, A. Kehlberger, D. H. Kim, G. Jakob, M. Kläui, A. V. Chumak, B. Hillebrands, and C. A. Ross. Pulsed laser deposition of epitaxial yttrium iron garnet films with low gilbert damping and bulk-like magnetization. *Apl. Mater.*, 2 (10):106102, 2014. doi:https://doi.org/10.1063/1.4896936.

[98] Lining Pan, Tingting Zhou, Yu Gao, Xueheng Zhuang, and Qikui Man. Angular-dependent spin-wave modes observations and excitation origins in yttrium iron garnet thin films. *Materials Today Communications*, 35:106028, 2023.

[99] L. G. Parratt. *Physical Review*, 95:359–369, Jul 1954.

[100] R. Peña-Garcia, A. Delgado, Y. Guerra, and E. Padrón-Hernández. *YIG* films with low magnetic damping obtained by solgel on silicon (100). *Mater. Lett.*, 161:384, 2015. doi:https://doi.org/10.1016/j.matlet.2015.08.147.

[101] P Pirro, T Sebastian, T Brächer, AA Serga, T Kubota, H Naganuma, M Oogane, Y Ando, and B Hillebrands. Non-gilbert-damping mechanism in a ferromagnetic heusler compound probed by nonlinear spin dynamics. *Physical Review Letters*, 113(22):227601, 2014. doi:https://doi.org/10.1103/PhysRevLett.113.227601.

[102] E. Popova, N. Keller, F. Gendron, M. Guyot, M..C Brianso, Y. Dumond, and M. Tessier. Structure and magnetic properties of yttrium–iron–garnet thin films prepared by laser deposition. *J. Appl. Phys.*, 90(3):1422, 2001. doi:https://doi.org/10.1063/1.1379344.

[103] Andy Quindeau, Can O Avci, Wenqing Liu, Congli Sun, Maxwell Mann, Astera S Tang, Mehmet C Onbasli, David Bono, Paul M Voyles, Yongbing Xu, et al. Tm3fe5o12/pt heterostructures with perpendicular magnetic anisotropy for spintronic applications. *Advanced Electronic Materials*, 3(1):1600376, 2017.

[104] Priti J Rajput, Sheetal U Bhandari, and Girish Wadhwa. A review on—spintronics an emerging technology. *Silicon*, pages 1–16, 2022. doi:https://doi.org/10.1007/s12633-021-01643-x.

[105] Ethan R Rosenberg, Lukáš Beran, Can O Avci, Cyrus Zeledon, Bingqian Song, Claudio Gonzalez-Fuentes, Johannes Mendil, Pietro Gambardella, Martin Veis, Carlos Garcia, et al. Magnetism and spin transport in rare-earth-rich epitaxial terbium and europium iron garnet films. *Physical Review Materials*, 2(9):094405, 2018.

[106] Ethan R Rosenberg, Kai Litzius, Justin M Shaw, Grant A Riley, Geoffrey SD Beach, Hans T Nembach, and Caroline A Ross. Magnetic properties and growth-induced anisotropy in yttrium thulium iron garnet thin films. *Advanced Electronic Materials*, 7(10):2100452, 2021. doi:https://doi.org/10.1002/aelm.202100452.

[107] A. Sakakibara. *Memoirs of the School of Engineering, Okayama University*, 10(2): 81–111, 1976.

[108] Georg Schmidt, Christoph Hauser, Philip Trempler, Maximilian Paleschke, and Evangelos Th Papaioannou. Ultra thin films of yttrium iron garnet with very low damping: A review. *physica status solidi (b)*, 257(7):1900644, 2020. doi:https://doi.org/10.1002/pssb.201900644.

[109] T Sebastian, Y Ohdaira, T Kubota, P Pirro, T Brächer, K Vogt, AA Serga, Hiroshi Naganuma, M Oogane, Y Ando, and B Hillebrands. Low-damping spin-wave propagation in a micro-structured $Co_2Mn_{0.6}Fe_{0.4}Si$ heusler waveguide. *Applied Physics Letters*, 100(11), 2012. doi:https://doi.org/10.1063/1.3693391.

[110] AA Serga, AV Chumak, and B Hillebrands. Yig magnonics. *Journal of Physics D: Applied Physics*, 43(26):264002, 2010.

[111] R Sharma, PK Ojha, S Choudhary, and SK Mishra. Magnetic ordering in sol-gel-based $Tm_3Fe_5O_{12}$ thin film. *Materials Letters*, 352:135154, 2023. doi:https://doi.org/10.1016/j.matlet.2023.135154.

[112] R Sharma, PK Ojha, and SK Mishra. Magnetic energy dissipative factors of spin-coated $Y_3Fe_5O_{12}$ thin films. *Thin Solid Films*, 764:139625, 2023. doi:https://doi.org/10.1016/j.tsf.2022.139625.

[113] Vinay Sharma, J Saha, S Patnaik, and Bijoy K Kuanr. Yig based broad band microwave absorber: A perspective on synthesis methods. *J. Magn. Magn. Mater.*, 439:277, 2017. doi:https://doi.org/10.1016/j.jmmm.2017.04.098.

[114] L. Soumah, N. Beaulieu, L. Qassym, C. Carrétéro, E. Jacquet, R. Lebourgeois, J. Ben Youssef, P. Bortolotti, V. Cros, and A. Anane. Ultra-low damping insulating magnetic thin films get perpendicular. *Nat. communicat.*, 9(1):1, 2018. doi:https://doi.org/10.1038/s41467-018-05732-1.

[115] M. Sparks, R. Loudon, and C. Kittel. Ferromagnetic relaxation. i. theory of the relaxation of the uniform precession and the degenerate spectrum in insulators at low temperatures. *Phys. Rev.*, 122(3):791, 1961. doi:10.1103/PhysRev.122.791.

[116] A. K. Srivastava, M. J Hurben, M. A Wittenauer, P. Kabos, C. E Patton, R Ramesh, P. C Dorsey, and D. B Chrisey. Angle dependence of the ferromagnetic resonance linewidth and two magnon losses in pulsed laser deposited films of yttrium iron garnet, mnzn ferrite, and nizn ferrite. *J. appl. phys.*, 85(11):7838–7848, 1999. doi:https://doi.org/10.1063/1.370595.

[117] AI Stognij, NN Novitskii, OL Golikova, AV Bespalov, R Gieniusz, A Maziewski, A Stupakiewicz, MN Smirnova, and VA Ketsko. Growth of $Y_3Fe_5O_{12}$ films on Si with AlO_x and SiO_2 buffer layers by ion beam sputtering. *Inorg. Mater.*, 53(10): 1069–1074, 2017. doi:10.1134/S0020168517100156.

[118] Y. Sun, Y.-Y. Song, H. Chang, M. Kabatek, M. Jantz, W. Schneider, M. Wu, H. Schultheiss, and A. Hoffmann. Growth and ferromagnetic resonance properties of nanometer-thick yttrium iron garnet films. *Appl. Phys. Lett.*, 101(15):152405, 2012. doi:https://doi.org/10.1063/1.4759039.

[119] Y. Sun, H. Chang, M. Kabatek, Y.-Y. Song, Z. Wang, M. Jantz, W. Schneider, M. Wu, E. Montoya, B. Kardasz, et al. Damping in yttrium iron garnet nanoscale films capped by platinum. *Phys. Rev. Lett.*, 111(10):106601, 2013. doi:https://doi.org/10.1103/PhysRevLett.111.106601.

[120] SM Suturin, AM Korovin, VE Bursian, LV Lutsev, V Bourobina, NL Yakovlev, M Montecchi, L Pasquali, V Ukleev, Alexei Vorobiev, A Devishvili, and N. S. Sokolov. Role of gallium diffusion in the formation of a magnetically dead layer at the y 3 fe 5 o 12/gd 3 ga 5 o 12 epitaxial interface. *Physical Review Materials*, 2 (10):104404, 2018.

[121] Ihor I Syvorotka, Dmytro Sugak, Uliana Yakhnevych, Oleh Buryy, Damian Włodarczyk, Agnieszka Pieniążek, Yaroslav Zhydachevskyy, Neonila Levintant-Zayonts, Hrygoryy Savytskyy, Oleksandr Bonchyk, et al. Investigation of the interface of y3fe5o12/gd3ga5o12 structure obtained by the liquid phase epitaxy. *Crystal Research and Technology*, 57(5):2100180, 2022.

[122] Yaroslav Tserkovnyak, Arne Brataas, and Gerrit EW Bauer. Enhanced gilbert damping in thin ferromagnetic films. *Phys. Rev. Lett.*, 88(11):117601, 2002. doi:https://doi.org/10.1103/PhysRevLett.88.117601.

[123] R Urban, Georg Woltersdorf, and B Heinrich. Gilbert damping in single and multilayer ultrathin films: Role of interfaces in nonlocal spin dynamics. *Physical review letters*, 87(21):217204, 2001. doi:10.1103/PhysRevLett.87.217204.

[124] Gilvânia Vilela, Hang Chi, Gregory Stephen, Charles Settens, Preston Zhou, Yunbo Ou, Dhavala Suri, Don Heiman, and Jagadeesh S Moodera. Strain-tuned magnetic anisotropy in sputtered thulium iron garnet ultrathin films and tig/au/tig valve structures. *Journal of Applied Physics*, 127(11), 2020.

[125] JJ Wang, ZB Fang, Ting' Ji, WY Ren, YY Zhu, and G He. Band offsets of epitaxial Tm_2O_3 high-k dielectric films on *Si* substrates by *X*-ray photoelectron spectroscopy. *Applied surface science*, 258(16):6107–6110, 2012. doi:https://doi.org/10.1016/j.apsusc.2012.03.013.

[126] S. Wang, G. Li, X. Huang, Y. Tian, J. Yu, L. Ren, H. Zhang, J. Wang, and K. Jin. Preparation of thulium iron garnet ceramics and investigation of spin transport properties in thin films. *Ceramics International*, 45(6):7649–7653, 2019.

[127] CN Wu, CC Tseng, YT Fanchiang, CK Cheng, KY Lin, SL Yeh, SR Yang, CT Wu, T Liu, M Wu, et al. High-quality thulium iron garnet films with tunable perpendicular magnetic anisotropy by off-axis sputtering–correlation between magnetic properties and film strain. *Scientific Reports*, 8(1):11087, 2018.

[128] H Wu, L Huang, C Fang, BS Yang, CH Wan, GQ Yu, JF Feng, HX Wei, and XF Han. Magnon valve effect between two magnetic insulators. *Physical review letters*, 120 (9):097205, 2018.

[129] Feng Xu, Qijun Huang, Zhiqin Liao, Shandong Li, and CK Ong. Tuning of magnetization dynamics in sputtered *CoFeB* thin film by gas pressure. *Journal of Applied Physics*, 111(7), 2012. doi:https://doi.org/10.1063/1.3670605.

[130] K. Yamada, K. Kogiso, Y. Shiota, M. Yamamoto, A. Yamaguchi, T. Moriyama, T. Ono, and M. Shima. Dependence of gilbert damping constant on microstructure in nanocrystalline *YIG* coatings prepared by co-precipitation and spin-coating on a *Si* substrate. *J. Magn. Magn. Mater.*, 513:167253, 2020. doi:https://doi.org/10.1016/j.jmmm.2020.167253.

[131] H Yamahara, M Mikami, M Seki, and H Tabata. Epitaxial strain-induced magnetic anisotropy in sm3fe5o12 thin films grown by pulsed laser deposition. *Journal of magnetism and magnetic materials*, 323(23):3143–3146, 2011.

[132] M. Yamamoto, S. Masaki, Y. Shiota, T. Moriyama, T. Kato, T. Ono, M. Shima, and K. Yamada. Bismuth composition, thickness, and annealing temperature dependence of the spin seebeck voltage in $Bi-YIG$ films prepared using sol–gel solution and spin-coating method. *J. Magn. and Magn. Mater.*, 556:169416, 2022.

[133] Saeedeh Mokarian Zanjani and Mehmet C Onbaşlı. Predicting new iron garnet thin films with perpendicular magnetic anisotropy. *Journal of Magnetism and Magnetic Materials*, 499:166108, 2020. doi:https://doi.org/10.1016/j.jmmm.2019.166108.

[134] Xiuye Zhang, Lichuan Jin, Dainan Zhang, Bo Liu, Hao Meng, Lei Zhang, Zhiyong Zhong, and Xiaoli Tang. Strong perpendicular anisotropy and anisotropic landé factor in bismuth-doped thulium garnet thin films. *Frontiers in Materials*, 9:879711, 2022. doi:10.3389/fmats.2022.879711.

[135] T. X Zhou, J. J Carmiggelt, L. M Gächter, I. Esterlis, D. Sels, R. J Stöhr, C. Du, D. Fernandez, J. F Rodriguez-Nieva, F. Büttner, E. Demlera, and A. Yacoby. A magnon scattering platform. *Proc. Nat. Acad. Sci.*, 118(25):e2019473118, 2021. doi:https://doi.org/10.1073/pnas.2019473118.

[136] HJ Zhu, M Ramsteiner, H Kostial, M Wassermeier, H-P Schönherr, and KH Ploog. Room-temperature spin injection from fe into gaas. *Phys. Rev. Lett.*, 87(1):016601, 2001. doi:10.1103/PhysRevLett.87.016601.

List of Publication

International Journals

1. “Interfacial skyrmion in magnetic thin films and its applications”, R. Sharma, S. K. Mishra, Journal of Magnetism and Magnetic Materials 551 **(2022)** 169107.

2. “Observation of V–V dimers softening and distinct length scales in nanostructured VO2 thin films ”, P.K. Ojha, R. Sharma, R. Hissariya, S. Babu, E. Ketkar, S. Singh, S. Neema, A. Rana, N. Pal, V.G. Sathe, S.K. Mishra, Journal of Physics and Chemistry of Solids 163 **(2022)** 110564.

3. “Antisites disorder mediated magnetization relaxation and polydispersity in La2NiMnO6 crystallites”, R. Hissariya, R. Sharma, S.K. Mishra, Journal of Physics and Chemistry of Solids 181 **(2023)** 111549.

4. “Magnetic energy dissipative factors of spin-coated Y3Fe5O12 thin films”, R. Sharma, P.K. Ojha and S.K. Mishra, Thin Solid Films 764 **(2023)** 139625.

5. “Magnetic ordering in sol-gel-based Tm3Fe5O12 thin films”, R. Sharma, P.K. Ojha, S. Choudhary and S. K. Mishra, Materials Letters 352 **(2023)** 135154.

6. “Charge ordering at a dielectric gate in itinerant metallic states with low-field memristor properties in VO2 thin films”, P. K. Ojha, R. Sharma, S. K. Mishra, and S. Ram, Surfaces and Interfaces 42 **(2023)** 103445.

7. “All solution grown epitaxial magnonic crystal of thulium iron garnet thin film”, R. Sharma, P. K. Ojha, S. Sahoo, R. Roychoudhary and S. K Mishra, Applied Physics Letters (under revision).

Proceeding

1. “The micromagnetic study of stabilizing parameters for the interfacial skyrmions”, R. Sharma, and S. K. Mishra, Materials Today: Proceedings 80 **(2023)** 1205.

Seminar and Symposium

1. MagIC+ Magnetism, Interactions and Complexity: innovative ideas on spin wave dynamics and transport properties in low-dimensional materials **(MagIC+ 2023)** Bedlewo, Poland **(Poster presented)**.

2. 8th International Conference on Nanomaterials for Better Living **(NBL 2023)** Srinagar, Kashmir **(Poster presented)**.

3. Recent Advancement in Sustainable Materials **(GC-RASM 2022)** Mangalore, Karnataka **(Oral presentation)**.

4. International Conference on Higher Education Research and Innovation **(ICHERI 2022) (Attended Virtually)**

5. International Conference on Advanced Materials and Mechanical Characterization **(ICAMMC 2021) (Attended Virtually)**

6. International Conference on Functional Nanomaterials **(ICFNM 2019)** Department of Physics, IIT (BHU), Varanasi, India **(Poster presented)**.

7. The European School on Magnetism **(ESM 2019)**, Brno, Czech Republic **(Poster Presented)**.

Vita

Rajnandini Sharma was borned on 14^{th} December 1993 in Rajasthan, India. She has completed her matriculation and intermediate in Madhya Pradesh, India. As she was among top 1% students of Madhya Pradesh in her intermediate, she got selected for the Scholarship for higher education (SHE), INSPIRE, DST, government of India. She also secured first position in her batch during her bachelor's degree at Gov. Holkar Science College, Indore. She has done master's degree in Physics at School of Physics, DAVV, Indore, India. She has attended summer internship at Institute for Plasma research (IPR), Gandhinagar, India during here master's degree. In IPR she has aligned an polychromator for the SST -1 TokamaK. As master's thesis she has studied temperature dependent Raman spectroscopic studies of $LaFeO_3$ and $LaMnO_3$ across magnetic ordering under Dr. vasant Sathe at UGC-DAE CSR, Indore. After completing her master's degree, she joined School of Physics, DAVV as Project fellow sponsored by Inter University Accelerator Center, New Delhi, India. There she developed her interest as materials researcher. Therefore, she decided to continue materials science as her doctorate stream. There after she joined Dr. Shrawan Kumar Mishra's lab at School of Materials Science and Technology, Indian Institute of Technology, (BHU). In her doctoral studied she has explored the ferromagnetic insulators, yttrium iron garnet (YIG) and thulium iron garnet (TmIG). She has synthesized 12- 25 nm thick epitaxial and polycrystalline thin films with all solution-based cost-effective method. She presented that it is possible to grow epitaxial thin films of application potential using cost-effective method.